



저작자표시-비영리-변경금지 2.0 대한민국

이용자는 아래의 조건을 따르는 경우에 한하여 자유롭게

- 이 저작물을 복제, 배포, 전송, 전시, 공연 및 방송할 수 있습니다.

다음과 같은 조건을 따라야 합니다:



저작자표시. 귀하는 원저작자를 표시하여야 합니다.



비영리. 귀하는 이 저작물을 영리 목적으로 이용할 수 없습니다.



변경금지. 귀하는 이 저작물을 개작, 변형 또는 가공할 수 없습니다.

- 귀하는, 이 저작물의 재이용이나 배포의 경우, 이 저작물에 적용된 이용허락조건을 명확하게 나타내어야 합니다.
- 저작권자로부터 별도의 허가를 받으면 이러한 조건들은 적용되지 않습니다.

저작권법에 따른 이용자의 권리는 위의 내용에 의하여 영향을 받지 않습니다.

이것은 [이용허락규약\(Legal Code\)](#)을 이해하기 쉽게 요약한 것입니다.

[Disclaimer](#)

공학박사학위논문

Tailor-fitted preparation of chemically
derived graphene-based materials and
their specific applications

화학적으로 유도된 그래핀 기반 재료의 용도 맞춤형
제조 및 응용

2015년 8월

서울대학교 대학원

재료공학부

정 해 슬

Abstract

**Tailor-fitted preparation of chemically
derived graphene-based materials and
their specific applications**

Haesol Jung

Department of Materials Science and Engineering

The Graduate School

Seoul National University

As a dream material, graphene has attracted much attention because of its unique and outstanding properties such as optical transparency, lightness, high surface area, high mechanical strength, and ultrahigh electrical conductivity beyond existing materials. In particular, chemically derived graphene (CDG) has been widely studied because it is produced in large scale and easily processed using graphene oxide (GO) as a versatile platform. To produce CDG-based material with desired properties, modification of GO such as reduction, functionalization, doping, and decoration is necessary. Although a number of studies have covered preparation of CDG through various modifications and applications, they still do not exhibit the superb properties of graphene as expected. This is because the application-targeting design of CDG for maximizing performance by tackling underlying challenge has been rarely attempted. To address this issue, this thesis determines the required properties for target application and designs the CDG-based material by modifying GO to have an optimized material characteristics based on the requirements. Additionally, this thesis verifies the improved performances of tailor-

fitted CDG-based materials in target applications.

Part I introduces an overview of the synthesis, characteristics, and applications of CDG-based materials as well as research on representative modification methods of GO to produce CDG-based materials for various applications. In particular, it focuses on three main application fields: transparent conductive film (TCF), gas barrier layer (GBL), and hydrogen storage. This thesis investigated the key issues in each application and assessed the efforts undertaken in state of the art to solve challenges. Application-specific tailoring strategies for CDG-based materials in each application are suggested to address the limitations in previous research.

Part II explains the tailor-fitted preparation method for CDG-based materials according to the strategies mentioned in Part I. Oxidation, reduction, and doping are used to produce CDG for TCF applications. As a tailor-fitted reducing agent for TCF, lithium naphthalenide (LN) is utilized since it derives ultrafast reduction of GO at room temperature without damaging the film and simultaneously provides a doping effect. As a result, CDG produced by LN reduction shows good TCF performance and stability. Functionalization with diol and reduction are used to prepare CDG for GBL applications. Edge-to-edge crosslinking functionalization, an unprecedented method for GBLs, induces an increased CDG lateral size, resulting in improved moisture shielding property. For hydrogen storage application, simultaneous reduction and functionalization of GO with polydopamine (PD) together with decoration of platinum (Pt) are used to synthesize CDG. The size, distribution, and loading amount of Pt and surface area of PD-functionalized CDG are tailored due to the systematic control of PD loading. As a result, the high hydrogen storage capacity even at room temperature is achieved.

Part III summarizes the tailor-fitted design of CDG-based materials for TCF, GBL,

and hydrogen storage applications and their performances. In conclusion, this thesis provides a CDG-based material preparation method through optimized modifications to improve performances in specific application, overcoming limitations of previous approaches.

Keywords: graphene, chemically derived graphene, graphene oxide, modifications, applications

Student Number: 2011-20670

Contents

Part I General introduction to basic researches on chemically derived graphene-based materials

Chapter 1. Introduction.....	2
1.1. Overview of chemically derived graphene (CDG)-based materials	2
1.1.1. Brief introduction of graphene	2
1.1.1.1. Structure and properties	2
1.1.1.2. Applications	3
1.1.1.3. Synthetic methods.....	3
1.1.2. Synthetic procedure of CDG.....	6
1.1.2.1. Preparation of graphene oxide (GO): oxidation of graphite.....	6
1.1.2.2. Preparation of CDG: reduction of GO.....	7
1.1.3. Structure of GO and CDG	8
1.1.3.1. Structure of GO	8
1.1.3.2. Structure of CDG	9
1.1.4. General modifications of CDG-based materials.....	11
1.1.4.1. Reduction.....	11
1.1.4.1.1. Chemical reduction	11
1.1.4.1.2. Thermal reduction.....	13
1.1.4.2. Functionalization	13
1.1.4.2.1. Covalent functionalization	13

1.1.4.2.2. Noncovalent functionalization	19
1.1.4.3. Doping and Decoration.....	21
1.1.4.3.1. Doping with non-metal atoms.....	21
1.1.4.3.2. Doping with molecules	25
1.1.4.3.3. Decoration with metal or metal oxide	25
1.2. Issues and state-of-the-art research on specific applications using chemically-derived graphene	29
1.2.1. Transparent conductive film (TCF).....	29
1.2.2. Gas barrier layer (GBL)	31
1.2.3. Hydrogen storage	32
1.3. Scope and aim of the present work	35
1.4. References.....	36

Part II Tailor-fitted preparation and applications of CDG-based material

Chapter 2. Chemically reduced GO through reduction and doping using lithium naphthalenide (LN).....	47
2.1. Introduction	47
2.2. Experimental	49
2.2.1. Materials and reagents	49
2.2.2. Synthesis of materials	50
2.2.2.1. Preparation of LN	50
2.2.2.2. Synthesis of rGO(LN_reduction time_M)	50

2.2.2.3. Synthesis of rGO(LN_reduction time_T)	50
2.2.2.4. Synthesis of rGO(H) and to rGO(S).....	51
2.2.2.5. Preparation procedure for fragility test.....	51
2.2.3. Fabrication of TCF	51
2.2.3.1. Fabrication of transparent conductive film.....	51
2.2.3.2. Comparison of reduction effect on TCF	52
2.2.4. Characterization.....	52
2.3. Characteristics and application.....	53
2.3.1. Characteristics	53
2.3.1.1. Validation of reduction efficiency.....	53
2.3.1.2. Crystal and physi-/chemical structure	60
2.3.1.3. Microstructure	62
2.3.1.4. Fragility and flexibility	64
2.3.2. Application for TCF	65
2.3.2.1. Effect of oxidation control on TCF performance	65
2.3.2.2. Effect of reduction control on TCF performance	66
2.3.2.3. Effect of doping on TCF performance.....	69
2.4. Conclusions	72
2.5. References.....	73

Chapter 3. Edge-to-edge bridged graphene/PVDF-HFP composite through functionalization using diol and reduction.....	78
3.1. Introduction	78

3.2. Materials and Methods	79
3.2.1. Materials and reagents	79
3.2.2. Synthesis of materials	80
3.2.2.1. Synthesis of GO.....	80
3.2.2.2. Synthesis of edge-to-edge bridged GO.....	80
3.2.2.3. Synthesis of bridged GO and a hybrid composite using other linkers .	
.....	81
3.2.3. Fabrication of gas barrier layer.....	81
3.2.4. Characterization.	81
3.3. Characteristics and application.....	83
3.3.1. Characteristics	83
3.3.2. Application for gas barrier layer	91
3.4. Conclusions	93
3.5. References.....	94

Chapter 4. Pt-decorated graphene through reduction, functionalization, doping, and metal decoration.....	96
4.1. Introduction	96
4.2. Tailor-fitted preparation of Pt-decorated graphene for hydrogen storage	99
4.2.1. Material and reagents.....	99
4.2.2. Synthesis of Materials.....	99
4.2.2.1. Synthesis of PD	99
4.2.2.2. Synthesis of PD_Pt.....	99

4.2.2.3. Synthesis of rGO.....	100
4.2.2.4. Synthesis of rGO_Pt.....	100
4.2.2.5. Synthesis of rGO/PDxx.....	100
4.2.2.6. Synthesis of rGO/PDxx_Pt.....	100
4.2.3. Characterization.....	101
4.3. Characteristics and application.....	102
4.3.1. Characteristics	102
4.3.2. Application for hydrogen storage	117
4.4. Conclusion	118
4.5. References.....	119

Part III Conclusions

Chapter 5. Conclusive remarks	123
-------------------------------------	-----

List of Tables

Table 2. 1. Comparison of the synthetic conditions and measured parameters for the graphene chemically prepared using various reducing agents

Table 2. 2. Values of σ_{DC}/σ_{OP} .

Table 4. 1. Quantitative analysis of XPS C 1s data.

Table 4. 2. Summary of BET SSA, Pt size and content, and hydrogen uptake of samples

List of Figures

- Figure 1. 1. Quality and price coordinates with promising application fields of several methods for graphene production.[35]
- Figure 1. 2. Representative structure models of GO suggested by (a) Hofmann, (b) Ruess, (c) Scholz-Boehm, (d) Nakajima-Matsuo, and (e) Lerf-Klinowski.[57]
- Figure 1. 3. (a) Transmission electron microscopy (TEM) image of rGO with 1nm scale bar. Colors are added to highlight the different features as follows: dark gray, contaminated regions; blue, disordered network or extended defects; red, ad-atoms or substitutions; green, isolated defects; yellow, holes. (b) Simulated morphology of rGO sheets. (Grey, carbon; red, oxygen; white, hydrogen)[58, 60]
- Figure 1. 4. Possible pathways of de-epoxidation of GO by (a) hydrazine[61, 73] and (b) hydroiodic acid.[64, 67]
- Figure 1. 5. Covalent functionalization on edge of GO by (a) and (b) amidation and (c) esterification.[80, 81, 83]
- Figure 1. 6. Covalent functionalization on basal plane of GO using (a) hydroxyl and (b) and (c) epoxy functional groups in GO.[85-87]
- Figure 1. 7. Covalent functionalization on both edge and basal plane of GO using (a) isocyanate and (b) diol and diamine.[89, 90]
- Figure 1. 8. Noncovalent functionalization of GO with dye-labeled ssDNA.[91]
- Figure 1. 9. Schematic illustration of nitrogen-doped rGO using (a) cyanamide and (b) melamine and (c) sulfur-doped rGO. [95, 98, 105]
- Figure 1. 10. Schematic illustration of synthesis and applications of rGO decorated with gold nanoparticles to (a) surface-enhanced Raman scattering substrate and (b) memory device.[114, 116]
- Figure 1. 11. Schematic illustration of synthesis of rGO decorated with (a) SnO₂, (b) Mn₃O₄, and (c) TiO₂. [117, 118, 123]

- Figure 1. 12. Representative modification of GO for CDG-based TCF: (a) Oxidation control to prepare large size CDG and (b) post-doping to improve electrical conductivity of CDG.[109, 124, 125]
- Figure 1. 13. Approaches to improve hydrogen storage capacity through (a) functionalization,[132] (b) doping,[136, 137] and (c) decoration.[138, 139]
- Figure 2. 1. Scheme of the ultrafast reduction of GO. Note that gray, white, red, and violet spheres indicate carbon, hydrogen, oxygen, and lithium-containing compounds, respectively.
- Figure 2. 2. XPS C1s spectra of (a) GO and (b) rGO(LN_10min_M). Relative ratios of (c) oxygen-containing functional groups to aromatic carbons in GO and MeOH-washed rGO, and (d) C-O-C/C-OH + O=C-O in MeOH-washed rGO as a function of the reduction time; the total carbon content was assumed to remain unchanged, 100%.
- Figure 2. 3. FTIR spectra of GO and rGO (LN_10min_M).
- Figure 2. 4. The proposed GO reduction pathways to form (a) Li_2O , (b) Li_2O_2 , and (c) Li_2CO_3 as a by-product.
- Figure 2. 5. (a) XRD patterns of GO, rGO(LN_10min_M), rGO(LN_30min_M), and rGO(LN_60min_M). (b) Raman spectra of GO, rGO(LN_10min_M), rGO(LN_30min_M), and rGO(LN_60min_M) with I_D/I_G .
- Figure 2. 6. (a) SEM image, (b),(c) TEM images, and (d) SAED pattern of rGO(LN_10min_M).
- Figure 2. 7. Photographs of GO films immersed in various reducing agents (35 wt% aqueous N_2H_4 solution, 0.2 M NaBH_4 , and LN) for various reaction times: (a) 1 min, (b) 5 min, (c) 60 min, (d) 120 min, and (e) 2 days. For clarity, the rGO film reduced by LN was re-immersed in MeOH after reduction because the LN solution is dark green. (f) A flexible rGO(LN_10min_M) film.
- Figure 2. 8. SEM images and size distribution of (a) small sized GO, (b) medium sized

GO, and (c) large sized GO.

Figure 2. 9. (a) Photos of rGO TCFs prepared using different concentrations of GO and different reducing agents. (b) XPS C1s spectra of rGOs prepared by using different reducing agents.

Figure 2. 10. Controlled doping of lithium-containing moieties of rGO by controlling washing step.

Figure 2. 11. XPS (a) C1s spectra and (b) O1s spectra of rGO(LN_10min_T).

Figure 2. 12. (a) Sheet resistance and (b) Raman spectra of rGO(LN_M) and rGO(LN_T).

Figure 2. 13. (a) TCF performance of rGO(LN_T). (b) TCF stability of rGO(LN_M) with nitric acid doping and rGO(LN_T).

Figure 3. 1. Schematic illustration of the edge-to-edge bridged rGO (c-rGO)/PVDF-HFP synthesis process.

Figure 3. 2. (a) Side view and (b) Top view of GO, GO(CaCl₂), GO(PEI), and GO(HQ).

Figure 3. 3. (a) Images of the GO, GO(ED), GO(HD), GO(HQ), and GO(DN) dispersions in DMF. (b) Optical images and G-band Raman maps of the rectangular region and corresponding Raman spectra of GO(HQ)/PVDF-HFP and GO(PEI)/PVDF-HFP as indicated by the arrows.

Figure 3. 4. FTIR spectra of GO, GO(ED), GO(HD), GO(HQ), and GO(DN).

Figure 3. 5. SEM images of (a) GO and (b), (c) GO(HQ). (The white circles indicate the bridge between the GO sheets.) (d), (e) TEM images of GO(HQ). (f) The sheet size distributions of the GO and GO(HQ). The average sheet sizes of the GO and GO(HQ) are 9.44 and 19.32 μm , respectively.

Figure 3. 6. XRD patterns of GO, GO(ED), GO(HD), GO(HQ), and GO(DN).

Figure 3. 7. (a) Permeability levels of PVDF-HFP, rGO/PVDF-HFP, rGO(ED)/PVDF-HFP, rGO(HD)/PVDF-HFP, rGO(HQ)/PVDF-HFP, and rGO(DN)/PVDF-HFP. Note that shortened sample names were displayed in the graph. (b) Relative water vapor shielding performances of GO and rGO(HQ)/PVDF-

HFP as a function of time.

Figure 4. 1. XPS N 1s spectra of (a) rGO/PD06 and (b) rGO/PD06_Pt. XPS (c) C 1s and (d) Pt 4f spectrum of rGO/PD06_Pt.

Figure 4. 2. UV-Vis absorption spectra of (a) dopamine and (b) rGO/PDs with different reaction times.

Figure 4. 3. SEM images of (a) rGO/PD03, (b) rGO/PD06, and (c) rGO/PD12. (d) Nitrogen content as a function of reaction time.

Figure 4. 4. XPS C 1s spectra of (a) GO, (b) rGO, (c)-(f) rGO/PDs.

Figure 4. 5. FTIR spectra of GO and rGO/PD06

Figure 4. 6. Photograph of rGO/PD foam.

Figure 4. 7. SEM images of (a) rGO/PD03, (b) rGO/PD06, and (c) rGO/PD12. (d) Nitrogen adsorption isotherms and BET SSA of rGO/PDs with different reaction times.

Figure 4. 8. TEM images of (a), (c) PD_Pt and (b), (d) rGO_Pt.

Figure 4. 9. TEM images of (a) rGO_Pt, (b) rGO/PD03_Pt, (c) rGO/PD06_Pt, (d) rGO/PD09_Pt, (e) rGO/PD12_Pt. (f) Magnified image of rGO/PD_Pt.

Figure 4. 10. Correlation between (a) size of Pt and (b) content of Pt and degree of functionalization of PD.

Figure 4. 11. XRD patterns of rGO/PD, rGO/PD03_Pt, rGO/PD06_Pt, and rGO/PD09_Pt.

Figure 4. 12. (a) Nitrogen adsorption isotherms of rGO/PD_Pt and (b) hydrogen uptake at 298 K and 10 bar with Pt content of rGO/PD_Pts.

Figure 4. 13. Pore size distribution of rGO/PD_06 and rGO/PD06_Pt by cumulative pore volume using Barrett-Joyner-Halenda (BJH) model.

Figure 4. 14. Hydrogen uptakes of rGO, rGO/PD06, and rGO/PD06_Pt at 298 K and 100 bar.

Part I

General introduction to basic researches on chemically derived graphene-based materials

Chapter 1. Introduction

1.1. Overview of chemically derived graphene (CDG)-based materials

Graphene is regarded as a new material of dream owing to its extraordinary properties exceeding existing materials. Since Novoselov and Geim experimentally discovered graphene in 2004, interest in graphene has boomed to produce extensive researches to date.[1] Especially, studies using chemically derived graphene (CDG) has been conducted due to its practicality. Prior to overview of CDG-based materials, a brief introduction of graphene will be provided ahead to help comprehensive understanding of CDG as an extension of graphene.

1.1.1. Brief introduction of graphene

1.1.1.1. Structure and properties

Graphene is a single-atom-thick sheet of sp^2 -hybridized carbon atoms arranged in a hexagonal pattern. Graphene is the thinnest carbon material, which absorbs only 2.3% of light in the visible light range,[2, 3] and the strongest material with Young's modulus of 1.0 TPa and intrinsic stress of 130 GPa, which is over 100 times stronger than steel.[4] In addition, graphene shows high flexibility, and owing to its structural character, even the smallest molecules such as hydrogen or helium cannot pass through the layer.[5] Graphene is a zero-band gap semiconductor where conduction band and valence band meet at the Dirac point. The unique electronic character makes the electrons behave massless, resulting in ultrahigh electron mobility up to $200,000 \text{ cm}^2\text{V}^{-1}\text{s}^{-1}$, which is more than 100 times that of silicon.[6-8] Thermal conductivity of

graphene is also superb at $600 \text{ Wm}^{-1}\text{K}^{-1}$, which is about ten times superior to metals such as copper and aluminum.[9] In addition, the theoretical specific surface area of graphene is $2630 \text{ m}^2/\text{g}$, which is much higher than other carbon materials.[10, 11]

1.1.1.2. Applications

The excellent properties of graphene beyond existing materials have brought intensive attention in a wide range of fields. As an alternative to existing silicon-based transistors, graphene has high charge carrier mobility and excellent thermal conductivity.[12, 13] Together with high flexibility, transparency, and good conductivity, use of graphene extends to the flexible transparent electrode, which is the key requirement for advancing a new next era of electronic devices. Graphene-based transparent electrodes applied in an organic light-emitting diode (OLED), display, and solar cell, have been reported.[14-16] In order to increase the life span of optoelectronic devices mentioned above, graphene also can be used as a gas barrier layer owing to its impermeability to effectively shield outer gases that can damage the device.[17-19] In addition, high specific surface area and the possibility of modification for efficient redox reaction make graphene viable in energy storage applications.[11, 20, 21] Other than these fields, graphene has infinite potential for other applications, including structural materials, sensors, heat dissipative insulating layers, and bio-applications.[22-27]

1.1.1.3. Synthetic methods

Novoselov and Geim (2004) experimentally obtained graphene by micromechanical exfoliation of graphite using adhesive tape.[1] Although this method could produce graphene with large-size crystallites with ultrahigh charge carrier mobility, difficulty in

scalable production limits further applications. As an alternative, bottom-up approaches have been studied. For example, monolayer or multilayer graphene was grown on a metal substrate such as copper foil by the chemical vapor deposition (CVD) technique.[28] Moreover, a report on 30-inch CVD-grown graphene film by roll-to-roll processing highlights the possibility of commercializing graphene.[29] However, expensive facilities for CVD, contamination by residues, and limit in mass production are still remaining problems. Graphene is also synthesized by sublimating non-carbon atoms from carbon-containing substrates such as SiC by epitaxial growth.[12, 30] Although this method can produce high quality graphene with a size of tens to hundreds of micrometers, use of an expensive SiC wafer and high temperatures are the main demerits. Due to the low practicality of the aforementioned methods, liquid-phase exfoliation methods including sonication-assisted exfoliation of graphene from graphite,[31] oxidized graphite,[32] graphite intercalation compounds,[33] and unzipped carbon nanotubes[34] have attracted much attention. Especially, synthesis of graphene by oxidation of graphite followed by reduction is a good candidate for graphene due to the advantages of relatively high efficiency, scalability, and possibility of versatile design for further applications. In this regard, thesis is exclusively focused on the chemically derived graphene (CDG), and general overview of CDG will be followed (Figure 1.1).

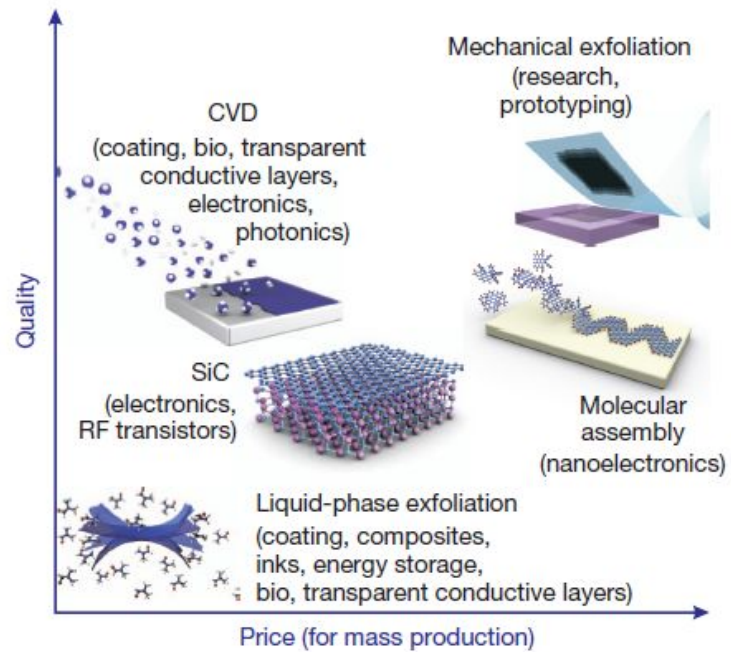


Figure 1. 1. Quality and price coordinates with promising application fields of several methods for graphene production.[35]

1.1.2. Synthetic procedure of CDG

Graphite is considered as the first precursor to make graphene. However, strong van der Waals interaction between sheets makes direct exfoliation of graphite into graphene sheets difficult. As an alternative route, production of graphene from graphene oxide (GO) has been investigated. The use of GO has advantages such as good dispersibility under solvents for easy exfoliation and processing, and possession of oxygenated functional groups that can be used for further modifications. Synthesis of CDG consists of two steps: 1) oxidation of graphite to produce GO and 2) reduction of GO to produce CDG. (Note that CDG is a product derived by reducing GO and is sometimes called reduced GO (rGO).)

1.1.2.1. Preparation of graphene oxide (GO): oxidation of graphite

Synthesis of GO is the procedure of treating graphite with oxidizing agents by introducing oxygenated functional groups in the graphite. The history of oxidizing graphite traces back to over a few hundred years. In 1859, Brodie synthesized carbonic oxide which has a molecular formula of $C_{2.19}H_{0.80}O_{1.00}$ that use potassium chlorate and nitric acid.[36] Staudenmaier improved Brodie's method by increasing the amount and repetition of oxidants and sulfuric acid.[37] Although the ratio of oxygen to carbon (1.85) and inter-sheet spacing (6.23 Å) were increased, long reaction time and evolution of hazardous intermediate remained as a problem.[38] To counter these issues, Hummers (1958) tried a new method using sodium nitrate, potassium permanganate, and sulfuric acid, which resulted in GO with 6.67 Å of inter-sheet spacing within 2 hours.[39] Afterward, a majority synthesis of GO are based on

Hummers' method with modifications such as the addition of a pretreated step before oxidation or an improved washing step.[40-42] Recently, a general method contains two procedures: pretreatment of graphite sheets and main oxidation. In the first step, a dehydrating agent such as phosphorus pentoxide and oxidizing agents such as potassium persulfate and sulfuric acid help graphite to be exfoliated for facilitating the following oxidation. The next step is almost analogous to Hummers' method with a slight modification.

1.1.2.2. Preparation of CDG: reduction of GO

The reduction of GO is performed to generate CDG by removing oxygenated functional groups such as epoxy, hydroxyl, carbonyl, and carboxyl groups and by restoring π -conjugation. For this purpose, several reduction methods including thermal, chemical, electrochemical, photocatalytic, and combined reduction have been reported. In thermal reduction, GO is treated under generally low temperature around 200°C which decompose functional groups of GO into CO or CO₂ gases.[43] Thermal sources can extend to microwaves or photo-irradiation.[44, 45] Chemical reduction is based on the reaction between GO and chemical reducing agents such as hydrazine hydrate, sodium borohydride, and so on.[46-48] In electrochemical reduction, reduction of GO was conducted in an electrochemical cell where GO is deposited on a substrate.[49, 50] A photocatalyst such as TiO₂ can act as a reducing promoter by providing an accumulated electron by UV-irradiation to GO.[51] Combined reduction using several methods is also used.[47]

1.1.3. Structure of GO and CDG

1.1.3.1. Structure of GO

GO is a sensitive and complex material with low reproducibility and nonstoichiometric chemical composition. In addition, present characterization tools are difficult to clearly identify the chemical structure of GO. Hence, various structural models of GO have been suggested and have aroused debate over a few decades (Figure 1.2).

The early structural model of GO is based on repeated regular lattices as Hofmann and Holst's suggested. The model structure consists of epoxy groups on the basal plane of graphene.[52] Later, Ruess proposed a modified model of Hofmann's where the GO has a sp^3 -hybridized basal plane.[53] Based on the structural similarity of other materials such as $(CF)_n$ and $(C_2F)_n$, new models were suggested by Scholz et al. and Nakajima et al..[54, 55] Contrary to a previous lattice-based model, the most well-known model by Lerf and Klinowski showed a non-repeated and irregular structure for reflecting a nonstoichiometric character of GO, where hydroxyl and epoxy functional groups are present on the basal plane and carboxylic acid groups are at the periphery of the GO platelets.[56] This model has been modified slightly without significant change since it was reported. Hence, the chemical structure of GO can be generally understood based on the Lerf-Klinowski model. However, the chemical structure and nature of GO could vary, depending on the differences in graphite precursor and oxidation procedure.

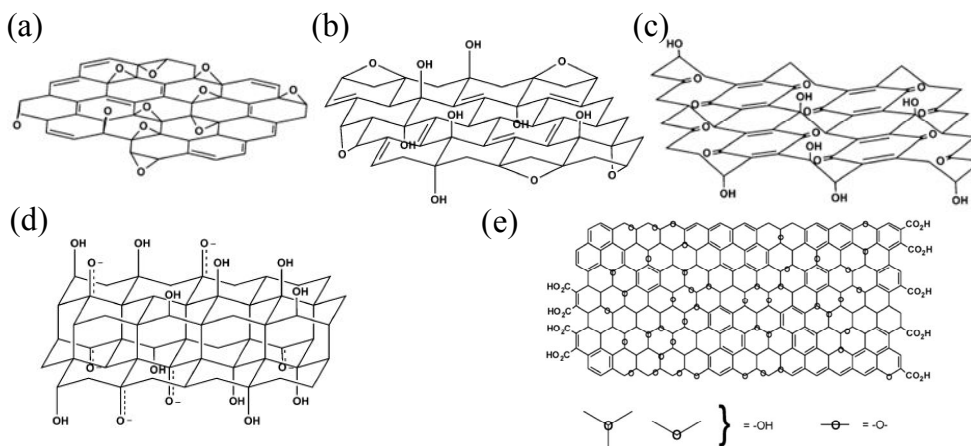


Figure 1. 2. Representative structure models of GO suggested by (a) Hofmann, (b) Ruess, (c) Scholz-Boehm, (d) Nakajima-Matsuo, and (e) Lerf-Klinowski.[57]

1.1.3.2. Structure of CDG

Ideally, graphene is single-atom-thick and a two-dimensional network of carbons where carbons are sp^2 -hybridized with hexagonal arrangement. CDG could be generally regarded as graphene. However, the structure of CDG based on the transition from GO to graphene is more reasonable because CDG is prepared from the reduction of GO. During reduction, most of the functional groups are removed and π -conjugation is restored, resulting in the structure of CDG as a two-dimensional carbon network with mostly sp^2 - hybridized carbon and some sp^3 - hybridized islands.[58, 59] However, the structure of CDG, is difficult to strictly define due to its dependence on treatments such as reduction and annealing (Figure 1.3).

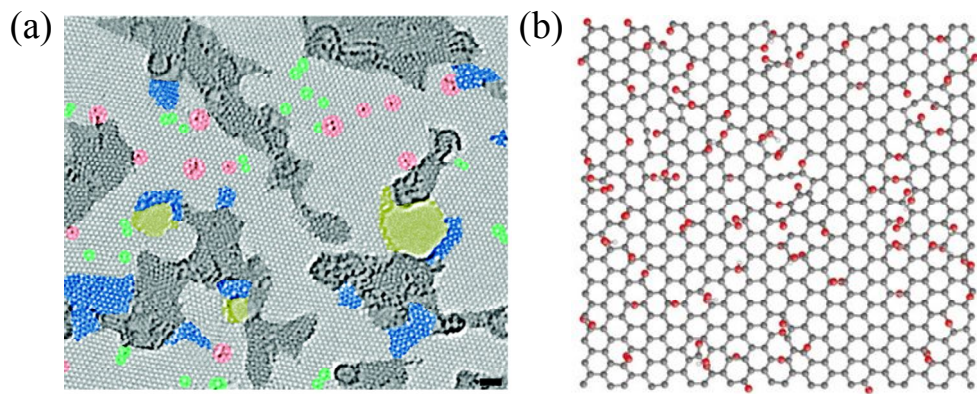


Figure 1. 3. (a) Transmission electron microscopy (TEM) image of rGO with 1nm scale bar. Colors are added to highlight the different features as follows: dark gray, contaminated regions; blue, disordered network or extended defects; red, ad-atoms or substitutions; green, isolated defects; yellow, holes. (b) Simulated morphology of rGO sheets. (Grey, carbon; red, oxygen; white, hydrogen)[58, 60]

1.1.4. General modifications of CDG-based materials

In order for CDG to be practical, effective production of high quality CDG and tailor-fitted design of CDG or CDG-based materials with desired properties are key issues of CDG-related research. To achieve these points, modification methods such as reduction, functionalization, doping, and decoration have been widely used. Because CDG has low processability without additional treatment, modification of GO followed by reduction is a more feasible route to produce application-specific CDG. In this context, general modifications of GO will be discussed.

1.1.4.1. Reduction

During reduction, removal of oxygen-containing functional groups and concurrent restoration of π -conjugation take place to produce electrically conductive CDG. Judging from this aspect, reduction of GO is a prerequisite step for electronic and energy storage applications. Although there are several methods to reduce GO as briefly mentioned in 1.1.2.2., the two most commonly used reduction methods will be presented here.

1.1.4.1.1. Chemical reduction

Chemical reagents have reducing strength and are involved in chemical reduction. A number of reducing agents have been reported so far. Some widely used reductants are hydrazine, sodium borohydride, and hydroiodic acid. Stankovich et al. reported the reduction of GO using hydrazine hydrate, where they proposed de-epoxidation as a possible reduction route.[46] Although reduction of other functional groups such as hydroxyl, carbonyl, and carboxylic acid groups have not been verified yet, some

possible reduction pathways based on the ring-opening of the epoxy group were theoretically suggested (Figure 1.4).[61, 62] Sodium borohydride is a commonly used reducing agent in synthetic chemistry and has been reported in many studies.[47, 63] BH_4^- attacks the electrophilic functional groups to produce BH_3 and oxyanion under aqueous condition, which can be further stabilized by combining with each other. The repeated process of this step continues to form boronate intermediate. Thus, GO can be finally reduced after water attack to the boronate intermediate.[64, 65] In organic chemistry, hydrohalic acids are nucleophilic and are able to open epoxide rings, hence, hydroiodic acid have been used to reduce GO. [64-67] In addition, lithium aluminum hydride, sulfuric acid, ascorbic acid, iron powder, and bovine serum albumin were investigated as reducing agents.[68-72]

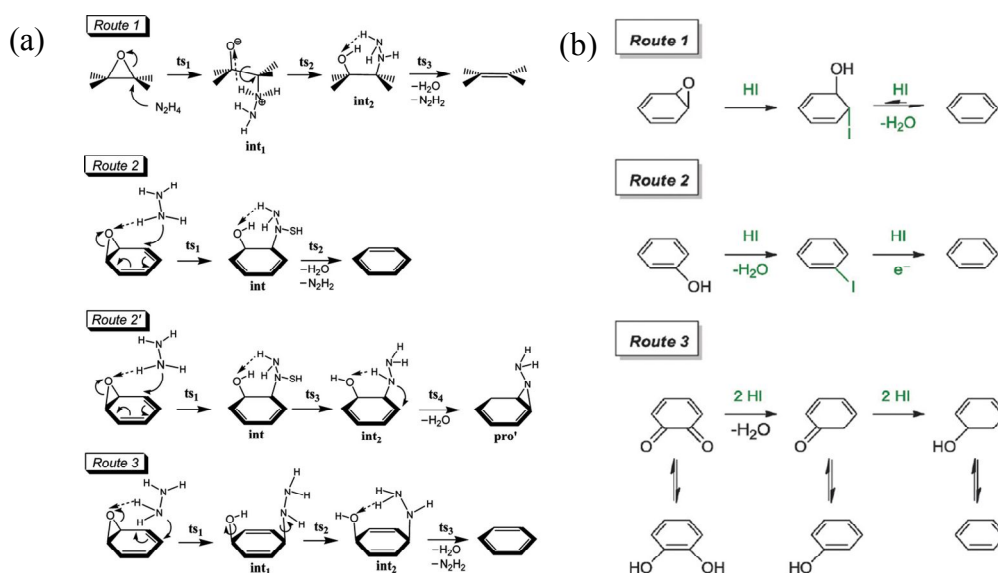


Figure 1. 4. Possible pathways of de-epoxidation of GO by (a) hydrazine[61, 73] and (b) hydroiodic acid.[64, 67]

1.1.4.1.2. Thermal reduction

Oxygen-containing functional groups in GO are decomposed by thermal sources such as heat, microwave, and xenon flash.[32, 44, 45] Thermal reduction was conducted under a wide range of temperatures under inert or reducing gases. Mcallister et al. calculated a diffusion coefficient and decomposition rate of decomposed gas, and concluded that a critical temperature for exfoliation of GO is 550 °C.[74] Thermal reduction under ultrahigh vacuum was conducted by varying temperatures in order to study the effect of temperature on properties of resulting rGO.[75] In some reports, much higher temperatures near 1000°C was used to reduce GO.[32, 47, 76] High temperature reduction has energy-consuming and control issues. Hence, GO reduction at a low temperature below 200°C has been investigated.[43, 77-79]

1.1.4.2. Functionalization

Various oxygen-containing functional groups of GO can act as reaction sites for functionalization. Functionalization can be classified into covalent and noncovalent functionalization, which is based on whether formation of a new bond is involved.

1.1.4.2.1. Covalent functionalization

In covalent functionalization, new bond formation takes place by a chemical reaction between the oxygenated functional groups of GO and specific species. GO has different kinds of oxygen-containing functional groups on its basal planes and edges. Carboxylic acid groups are on the edges, and hydroxyl and epoxy groups are on the basal planes of GO, which is based on the Lerf-Klinowski model.

Edge-on covalent functionalization generally uses amidation or esterification.

Typical amidation occurs when carboxylic acid group in GO reacts with amine. Liu et al. reported synthesized porphyrin (or fullerene)-functionalized rGO by forming an amide bond that resulted from the reaction between GO and amine-functionalizing porphyrin (or pyrrolidine-functionalized fullerene). They showed an enhanced nonlinear optical response for photonic or optoelectronic applications (Figure 1.5a).[80] For potential drug delivery material, covalently functionalized GO with amine-treated polyethylene glycol was suggested. Whereas GO had instability in biological solutions, functionalized GO showed excellent stability under the same condition (Figure 1.5b).[81] Glucose oxidase-functionalized GO via the formation of a peptide bond showed good sensing performance to glucose, suggesting a potential use in biosensor electrodes for clinical diagnosis.[82] In addition to amidation, another edge-on covalent functionalization, esterification reaction can occur when the carboxylic acid group in GO reacts with a hydroxyl group. For example, GO functionalized with poly(vinyl alcohol) was studied to produce stable GO dispersion under aqueous and polar organic solvents for solution processing without additional substances (Figure 1.5c).[83] Likewise, CH₂OH-terminated poly(3-hexylthiophene) (P3HT) was prepared by grafting it onto GO via esterification. In addition, a fabricated bilayer photovoltaic device based on the CH₂OH-P3HT-functionalized GO/C₆₀ heterostructure showed power conversion efficiency of three times that of P3HT and GO/C₆₀ mixture.[84]

Face-on covalent functionalization uses functional groups such as hydroxyl and epoxy groups on the basal plane of GO. Hydroxyl groups in GO react with boronic acid to produce GO frameworks with enhanced hydrogen and carbon dioxide storage capacity by tuning pore characteristics (Figure 1.6a).[85] Other than the hydroxyl group, the nucleophilic ring-opening of the epoxy group is also widely used to induce

covalent functionalization of the basal plane of GO. Ionic liquid, 1-(3-aminopropyl)-3-methylimidazolium bromide (IL-NH₂) reacted with GO, resulting in a reaction between the epoxy functional group in GO and the amine functional group in IL-NH₂. IL-NH₂-functionalized rGO showed long-term dispersion stability in some solvents such as water, N,N-dimethylformamide (DMF), and dimethyl sulfoxide (DMSO) due to electrostatic repulsion that originated from functionalized IL-NH₂ (Figure 1.6b).[86] As another example, functionalized rGO by covalent functionalization of GO with 3-aminopropyltriethoxysilane (APTS) via epoxy ring-opening reaction was reported. This reaction formed stable and homogeneous dispersion in various solvents, including water, ethanol, DMF, DMSO, and APTS. In addition, this functionalized rGO was used as a reinforcing component of APTS monolith and produced covalent bonding, which showed greatly improved failure strength and toughness in comparison to neat APTS (Figure 1.6c).[87] Improved mechanical strength of functionalized GO was also reported where cross-linking of GO with polyallylamine (PAA) occurred by the attack of amine groups in PAA to epoxy groups in GO.[88]

Generally, functionalization sites are not limited to either edge or basal plane of GO. Instead, functionalization on both sites can occur. Furthermore, the site of functionalization is not easy to be identified in many cases. Covalent functionalization of isocyanate onto GOs can be used by changing carboxylic acid and hydroxyl groups in GO into amide on the edge and carbamate esters on the basal plane of GO, respectively. This leads to stable dispersion in polar aprotic solvents (Figure 1.7a).[89] Also, site-selective cross-linking of GO can alter the mechanical property and electrical conductivity by reacting GO with 1,4-butanediol and ethylenediamine, respectively. Different properties of each sample are attributed to different stacked structures of GO (or rGO) paper by different interlayer distance, which depends on the reaction site

(Figure 1.7b).[90]

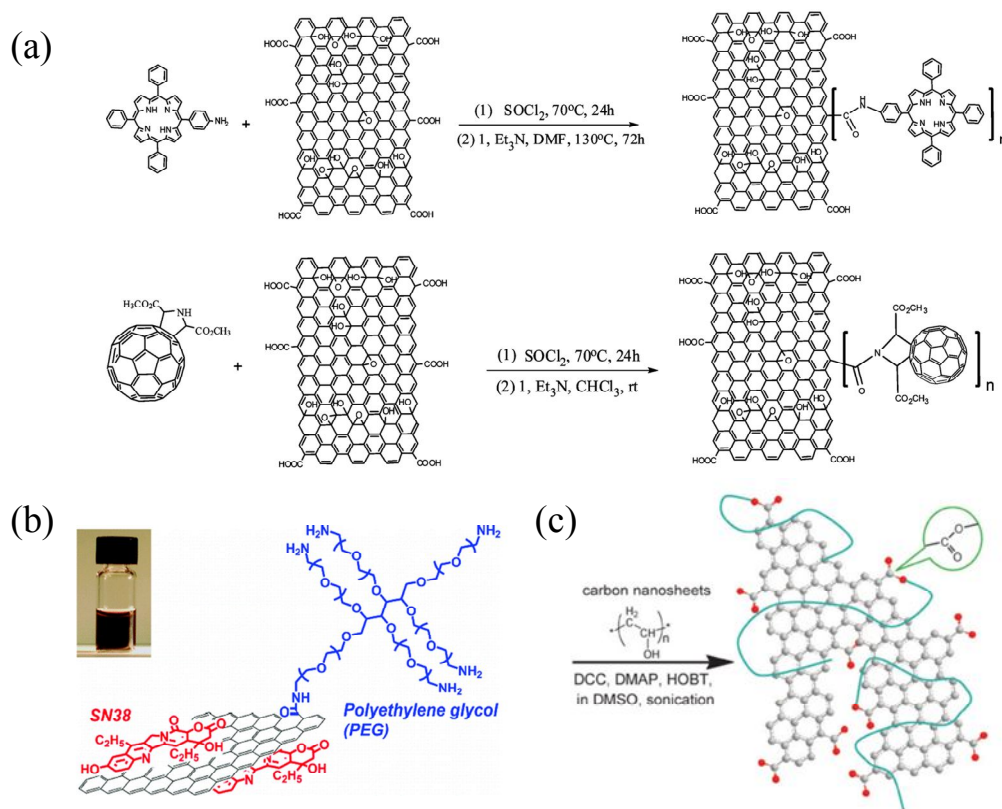


Figure 1. 5. Covalent functionalization on edge of GO by (a) and (b) amidation and (c) esterification.[80, 81, 83]

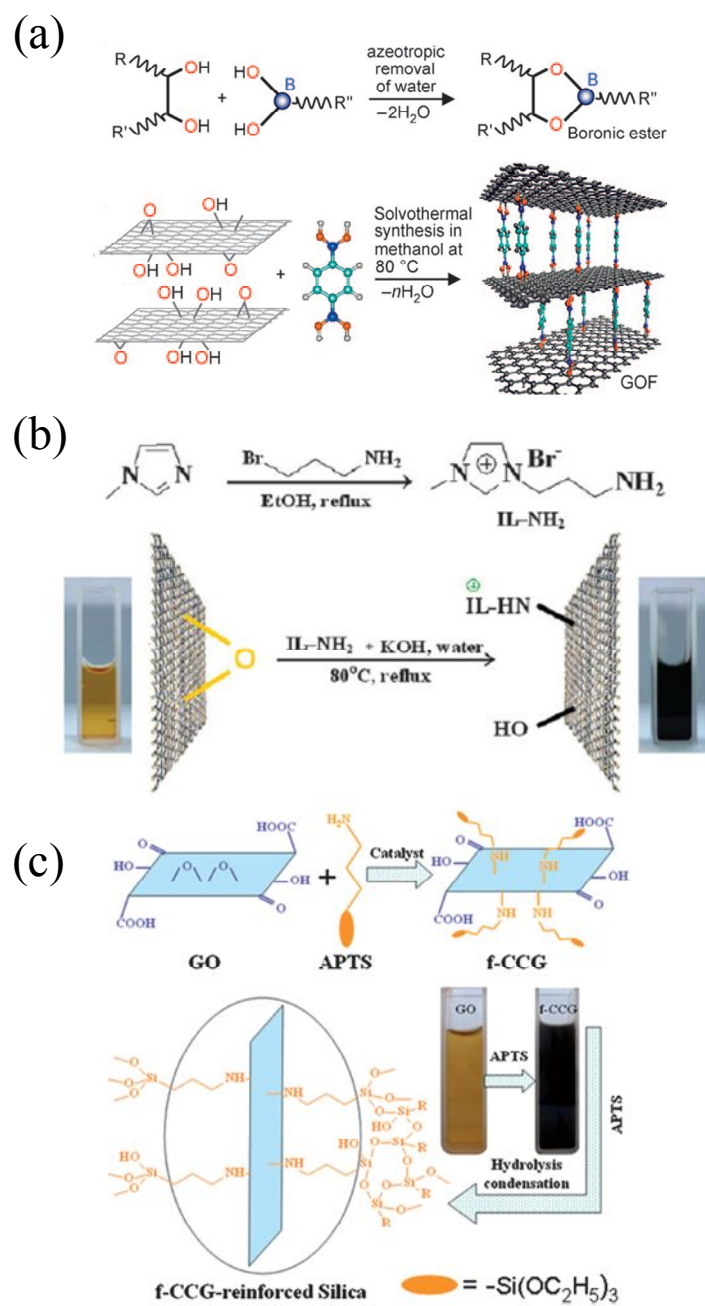


Figure 1. 6. Covalent functionalization on basal plane of GO using (a) hydroxyl and (b) and (c) epoxy functional groups in GO.[85-87]

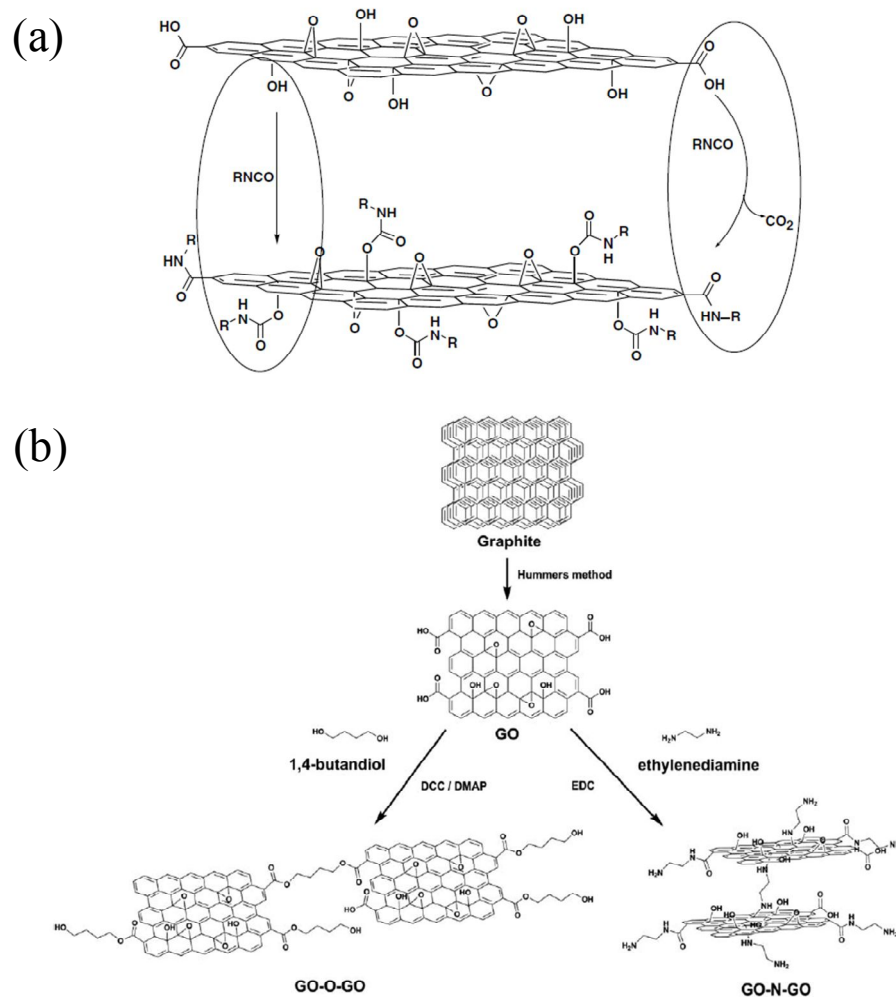


Figure 1. 7. Covalent functionalization on both edge and basal plane of GO using (a) isocyanate and (b) diol and diamine.[89, 90]

1.1.4.2.2. Noncovalent functionalization

GO can be noncovalently functionalized via π - π stacking and π -cation interaction in addition to van der Waals interaction. GO has a sp^2 hybridized carbon region where oxygen functional groups do not destroy the conjugation. Hydrogen bonding can also be involved, utilizing abundant functional groups in GO.

Lu et al. introduced dye-labeled ssDNA to GO via noncovalent functionalization that includes van der Waals interaction, π - π stacking, and hydrogen bonding between ssDNA or dye and GO. Using the dye fluorescence, which was quenched by interaction with GO and restored after its binding of target molecules, GO was proved to be a promising platform for biosensors (Figure 1.8).[91] Similarly, aptamer-carboxylfluorescein(FAM)/GO nanocomplex was reported elsewhere. GO was used both as a cargo of DNA into living cells and as a probe for adenosine triphosphate (ATP) in cells after noncovalent functionalization with aptamer-(FAM).[92] GO can be used as a carrier of the cancer therapy drug, doxorubicin hydrochloride (DXR), by efficiently binding and releasing DXR through π - π stacking and hydrogen bonding.[93]

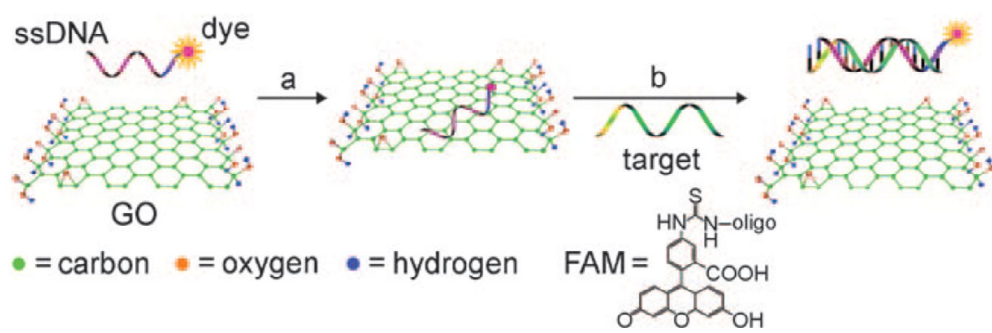


Figure 1. 8. Noncovalent functionalization of GO with dye-labeled ssDNA.[91]

1.1.4.3. Doping and Decoration

Introduction of atoms or molecules into GO (or CDG) have been widely used to tailor the structure and properties of GO (or CDG) for various applications such as catalysts, energy conversion and storage, optoelectronic devices, and magnetic applications. This modification can be classified into three types: 1) doping with non-metal atoms, 2) doping with molecules, and 3) decoration with metal or metal oxides, which depend on the type and role of introduced species. In detail, if the intrinsic properties of pristine CDG are altered after modification, CDG is categorized as doping. Otherwise, CDG is categorized as decoration. In addition, some examples in this modification could be included in other modifications (e.g., functionalization in the aspect of interaction between GO or CDG and added species). However, they will be explained in this section if chemical or structural properties of introduced species are altered from the starting precursor.

1.1.4.3.1. Doping with non-metal atoms

So-called heteroatom-doped CDG means doped CDG with non-metal atoms such as boron, nitrogen, phosphorus, and sulfur. Non-metal atom doping can affect structure, electronic structure, magnetic moment, and optical property of CDG, extending the application spectrum of CDG.

Both p and n types of doping is possible with nitrogen doping, depending on the environment of the doped nitrogen.[94] Regardless of type, doping can lead to an increase in electrical conductivity, which is advantageous for electronic applications. Crumpled nitrogen-doped rGO sheets with high pore volume was synthesized through following the reactions, functionalization of GO with cyanamide, polymerization of cyanamide, and calcination. Crumpled nitrogen-doped rGO sheets showed excellent

electrochemical properties for a supercapacitor, owing to a highly porous structure and high N-content (9.96%) (Figure 1.9a).[95] Li et al. reported nitrogen doped rGO quantum dots (N-GQDs) with a N/C ratio of 4.3 at % and blue luminescence, and its electrocatalytic activity was comparable to commercial Pt/C catalyst.[96] Nitrogen percentage in rGO is regulated by controlling exposure time. Resulted N-doped rGO can be an electrode for electrochemical catalysis of hydrogen peroxide and glucose sensor with excellent biocompatibility and fast electron transfer kinetics.[97] Using melamine as a nitrogen source, N-doped rGO with 10.1 at% nitrogen content was produced, which showed excellent electrocatalytic activity toward oxygen reduction reaction (ORR) in alkaline electrolytes (Figure 1.9b).[98] Besides the improved electronic and electrocatalytic properties, N-doping changes the characteristics of rGO, including tailored magnetic and optical properties. Annealing rGO under an ammonia environment produced N-doped rGO with 64.1 % increased magnetization in comparison to undoped rGO that was attributed to an increased spin polarization-induced magnetic moment caused by increasing pyrrolic nitrogen and prohibiting graphitic nitrogen.[99] With a similar strategy, Khai et al. reported that blue photoluminescence intensity of N-doped rGO significantly increased with an increase in annealing time.[100]

Phosphorus, which is in same group element with nitrogen, can also dope rGO, resulting in structural distortion, improved electrical conductivity through n-type doping, and induction of the magnetic moment. Phosphorus-doped rGO synthesized by thermal annealing of the mixture of GO and triphenylphosphine was used as an electrocatalyst in ORR as well as for an anode in a lithium ion battery.[101] Another example of P-doped rGO by Li et al. was synthesized through annealing of GO with 1-butyl-3-methylimidazolium hexafluorophosphate as a phosphorus source. This P-doped

rGO exhibited a high specific surface area of 496.67 m²/g and relatively high phosphorus content, which are advantageous for ORR.[102]

Doping of electron-deficient boron in rGO can induce a p-type doping effect, which improves the electrical properties of B-doped rGO. B-doped rGO synthesized by thermal annealing of GO with boron oxide showed excellent electrocatalytic activity, long-term stability towards ORR, and a good tolerance to poisons, indicating the possibility as a cathode in fuel cells.[103] B-doped rGO, which is synthesized using BCl₃, is also used as an anode material in lithium ion batteries, showing a high reversible capacity, high-rate capability, and long-term cyclability attributed to improvement in electrical conductivity, electrochemical activity, and surface morphology by boron doping.[104]

As another dopant, sulfur can be doped in rGO, inducing change in polarization favorable for catalytic properties and electronic structure.[94] S-doped rGO with benzyl disulfide as a sulfur source showed better catalytic activity toward ORR than a commercial Pt-based catalyst (Figure 1.9c).[105]

Besides monoatom-doped rGO, dual-doped rGO for various applications has been reported. Doping of more than one atom can give rise to a synergistic effect on application performance by significant change in the properties of rGO.[106, 107]

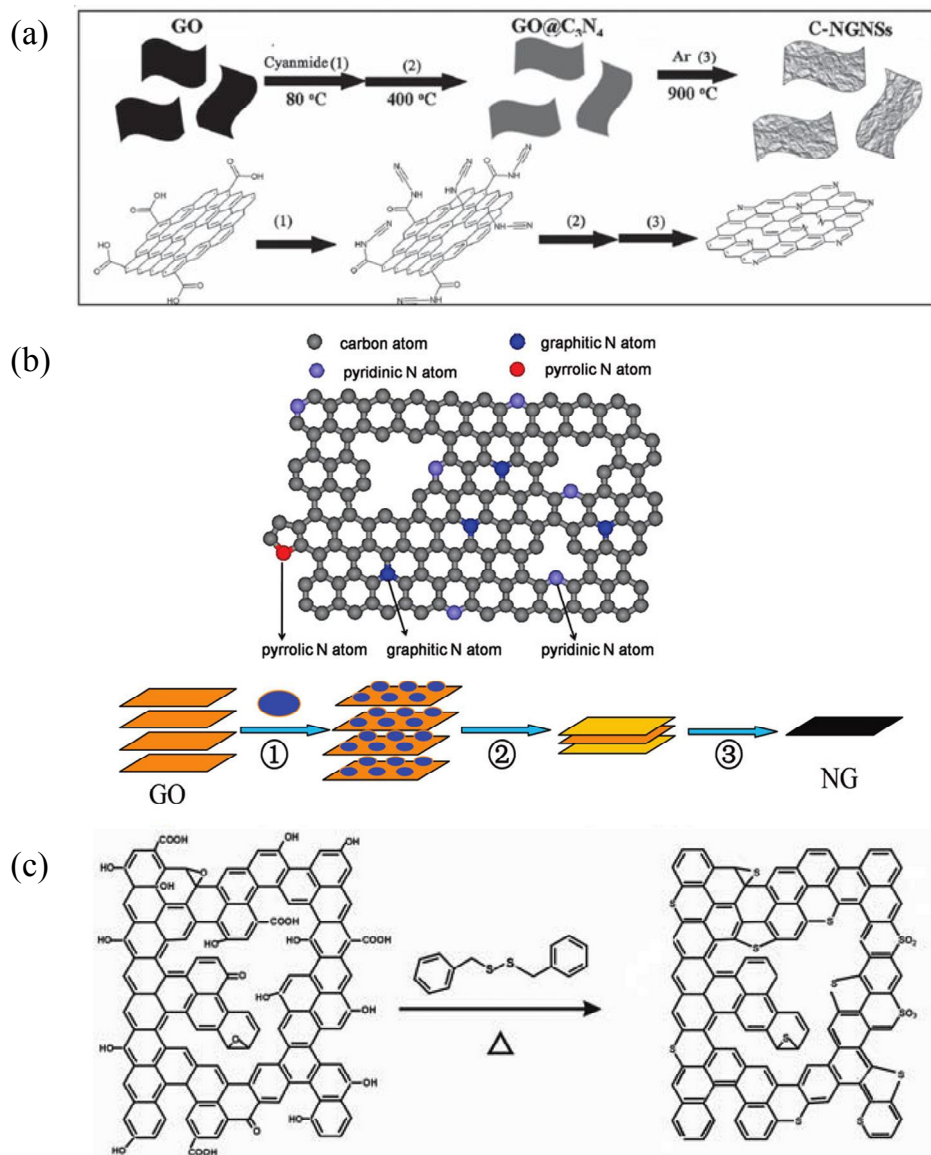


Figure 1. 9. Schematic illustration of nitrogen-doped rGO using (a) cyanamide and (b) melamine and (c) sulfur-doped rGO. [95, 98, 105]

1.1.4.3.2. Doping with molecules

When CDG is doped with molecules, electron donating or the withdrawing nature of molecules can influence the electronic property of CDG. This is because of the charge-transfer between CDG and the molecule, which could be attributed to orbital hybridization and position of the highest occupied molecular orbital (HOMO) and the lowest occupied molecular orbital (LUMO) of the molecule.[108] Owing to charge-transfer effect, molecule-doped CDG shows enhanced conductivity in comparison to pristine CDG. Hence, doping of CDG with molecules is especially used for transparent electrode.

For example, doping with iodine (I_2) (or iodine anion: I^-) can increase the electrical conductivity of rGO using hydroiodic acid, thus producing transparent conductive rGO film.[66, 109] Similarly, thionyl chloride vapor was used for anion doping of rGO/CNT nanocomposite. This treatment decreased sheet resistance of doped rGO containing nanocomposite in comparison to undoped rGO containing nanocomposite.[110] auric chloride can be used to increase hole concentration by withdrawing electrons from rGO to Au^{3+} ion. The sheet resistance of auric chloride-doped rGO transparent conductive film decreased by more than 50% in comparison to pristine rGO.[63]

1.1.4.3.3. Decoration with metal or metal oxide

A large specific surface area and high affinity to metal of GO or CDG enable GO to be used as a substrate for immobilizing metal or metal oxide. Metal or metal oxide exerts a special role in specific applications such as catalytic electrochemical energy storage.

Platinum-decorated rGO was synthesized and showed a high electrocatalytic activity for methanol oxidation reaction (MOR), which is attributed to subnanometer Pt

nanoparticles that originated from a strong interaction between rGO and Pt atoms.[111] A nanocomposite consisting of Pt-loaded rGO and chromate-organic framework (MIL-101) was prepared, which showed significant enhancement in room temperature hydrogen storage capacity due to spillover mechanism.[112] Pd and Au were used to produce rGO-metal nanoparticle nanocomposites, which have a potential application in methanol fuel cells.[113] Au-decorated rGO can be used in electronic and logic-devices by controlling the electrical properties, band gap, and schottky barrier, and as surface-enhanced Raman scattering (SERS) substrate by tailoring Raman properties (Figure 1.10a).[114, 115] As another example, Au-decorated rGO was demonstrated as an ambipolar memory device, which can be operated both as conductivity- and type-switching memory devices by controlling the charge density in Au nanoparticles (Figure 1.10b).[116]

Metal oxides such as tin (IV) dioxide (SnO_2), Manganese (II) dimanganese (III) oxide (Mn_3O_4), iron (III) oxide (Fe_2O_3), iron (II) iron (III) oxide (Fe_3O_4), and cobalt(II) oxide (CoO) have been reported as anode materials for lithium-ion batteries (Figure 1.11a and b).[117-120] Oxygen functional groups strongly interact with a metal ion to induce monodispersed and nano-sized metal oxide-decorated rGO. While metal nanoparticles prevent rGO from stacking, rGO can help accommodate the volume change of metal oxide during cycling, resulting in good rate capability from fast transport lithium ions and electrons as well as cycle stability. rGO decorated with Fe_3O_4 can be used to remove arsenic contamination in water purification because the hybrid material has advantages in both increased adsorption sites for arsenic and facile removal of arsenic from water using a superparamagnetic property.[121] For a semiconductor application, TiO_2 -decorated rGO was suggested. The properties of TiO_2 -decorated rGO were tunable, depending on the type of GO.[122] Titanium dioxide is

also used as a photocatalyst for hydrogen evolution from water splitting (Figure 1.11c).[123]

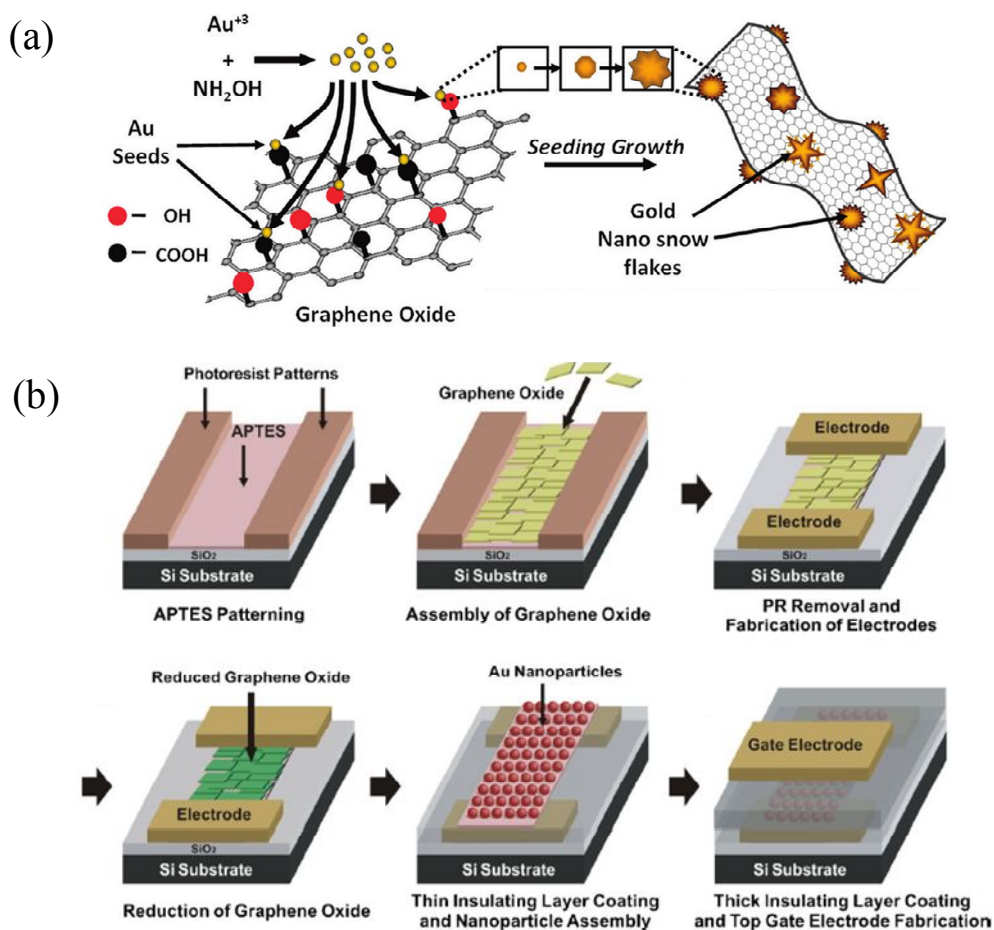


Figure 1. 10. Schematic illustration of synthesis and applications of rGO decorated with gold nanoparticles to (a) surface-enhanced Raman scattering substrate and (b) memory device.[114, 116]

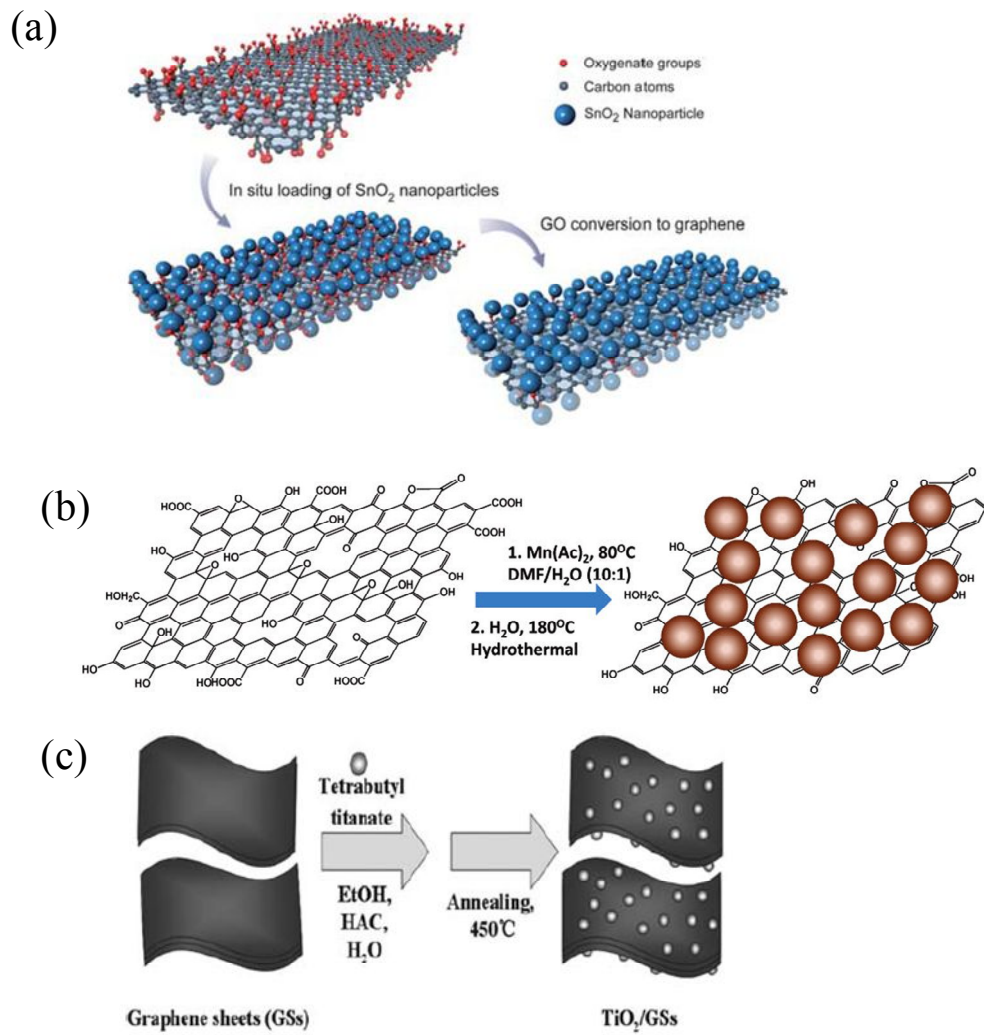


Figure 1. 11. Schematic illustration of synthesis of rGO decorated with (a) SnO₂, (b) Mn₃O₄, and (c) TiO₂. [117, 118, 123]

1.2. Issues and state-of-the-art research on specific applications using chemically-derived graphene

The outstanding properties of graphene promote the use of graphene to a variety of applications such as optoelectronics, protection barrier, and energy storage. In each subcategory, transparent conductive film (TCF), gas barrier layer (GBL), and hydrogen storage will be discussed in detail.

1.2.1. Transparent conductive film (TCF)

As a key component for optoelectronics, TCF has been widely studied. Besides optical transparency and electrical conductivity, flexibility should also be considered as an evaluating parameter of TCF because of the increasing demand for flexible devices. In order to improve the properties mentioned above, use of large lateral size of CDG with highly restored π -conjugation and post-modulation of a charge carrier is necessary.

A large lateral size CDG decreases inter-sheet contact resistance by reducing the number of inter-sheet junctions. Meanwhile, optical transparency is also improved because a small amount of CDG is required to comparable electrical properties than smaller sized CDG. To prepare large-sized CDG, an oxidation step to synthesize GO is controlled (Figure 1.12a).[109, 124] In addition, chemical doping of molecules such as nitric acid, iodine, and thionyl chloride were applied for further increase in electrical properties by increasing charge carrier density (Figure 1.12b).[124-126] Despite these efforts to improve TCF performance, a number of studies overlook the importance of the reduction step, and accept previously reported reduction methods without deep consideration. Reduction is a compulsory step to fabricate TCF because the

involvement of events during reduction (removal of oxygen functional group and restoration of π -conjugation) primarily determine the electrical conductivity of TCF. Additionally, reduction affects other important evaluating parameters such as film integrity and adhesion to the substrate. Hence, a study for an appropriate and practical reduction method for TCF is necessary.

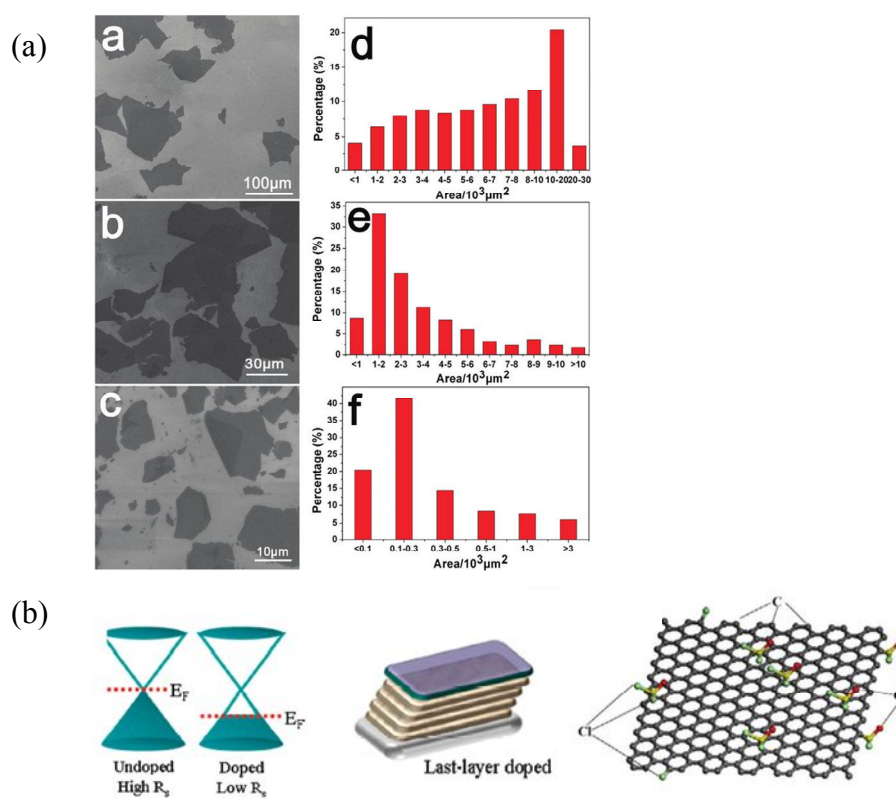


Figure 1. 12. Representative modification of GO for CDG-based TCF: (a) Oxidation control to prepare large size CDG and (b) post-doping to improve electrical conductivity of CDG.[109, 124, 125]

1.2.2. Gas barrier layer (GBL)

CDG is a promising candidate for GBL material. Theoretically, CDG has suitable nature for GBL, such as the impermeability, optical transparency, and flexibility. The reducing permeability of gases is a main research area in CDG-based GBL. Based on the gas permeation steps, efforts to minimize the dissolution and diffusion of gases have mainly been reported.

The development of outer surface properties that are unfavorable to gas permeation is important in order to suppress the dissolution of gases through the outer layer of GO or CDG-based material. In this context, hydrophobic surface moisture shielding through reduction modification can be a solution.[18, 127, 128]

The diffusion of gas should be suppressed by increasing the diffusion path after the dissolution of gases to the inner layer. The introduction of a high aspect ratio of GO or CDG into the matrix for producing a hybrid composite is a generally used method to obtain this goal.[129, 130]

Although studies to tackle major issues in GBL with CDG have showed improved performance, the results premature level because most studies are based on a simplified introduction of GO or CDG without a logical strategy. For this reason, a more fundamental approach to solve GBL-related issues should be investigated.

1.2.3. Hydrogen storage

As a versatile building block, CDG can be applied to hydrogen storage applications because CDG is tunable through proper modifications by having different porosities and surface characteristics. For hydrogen storage, the specific surface area (SSA) of CDG and the binding energy between CDG and hydrogen are the most important factors because these characteristics improve the potential of hydrogen storage on CDG-based material.[131] Three major potentials relating to hydrogen storage are Lennard-Jones (LJ), electrostatic (ES), and specific potential.

For example, LJ potential can be enhanced by developing GO or CDG with high SSA, which results from the overlap of van der Waals potential of pore walls. GO and CDG is considered to be composed of two dimensional graphene sheets with spacing, which is generally comparable or bigger than 0.75 and 0.34 nm, respectively. Hence, the tailored interlayer spacing of GO or CDG to generate SSA through covalent functionalization of GO using fillers with different lengths has been mainly investigated (Figure 1.13a).[132] Another approach investigated the effect of multiplicity of functionalization sites (depending on the different reaction sites of filler) on SSA and hydrogen storage capacity.[133]

In order to improve ES potential, heteroatom doping such as boron or nitrogen has been investigated. Heteroatom doping induces change in the electronic structure of CDG, resulting in induced dipole/quadrupole moment of hydrogen which contributes to the adsorption of hydrogen (Figure 1.13b). [134-136] In addition, heteroatom doping can be further used to stabilize metal decoration which is generally applied to enhance the specific potential due to its high affinity to metal and thus preventing aggregation.

The efforts to increase hydrogen storage using specific interactions have been devoted because of their outstanding effect on hydrogen storage at ambient conditions,

which can be a solution for hydrogen economy to come true. However, hydrogen storage mechanisms of this type have not yet been revealed. Representative specific interactions are spillover and Kubas interaction (Figure 1.13c). Spillover means the sequences of hydrogen dissociation by catalytic metal and diffusion of dissociated hydrogen atom on the surface of material. In Kubas interaction, bidirectional interactions of electron donation from filled σ -orbital of hydrogen to unfilled d-orbital of transition metal, and electron back-donation from filled d-orbital of transition metal to unfilled σ^* -orbital of hydrogen are generally suggested.

A number of studies have shown increased hydrogen storage using the above mentioned approaches. Only a few studies meet the target value as suggested by the US Department of Energy (DOE). Most studies tried to modify one or two potential terms by providing fragmentary information. Appropriate synergistic modification of CDG that affect all three potential terms for improved hydrogen storage capacity is necessary.

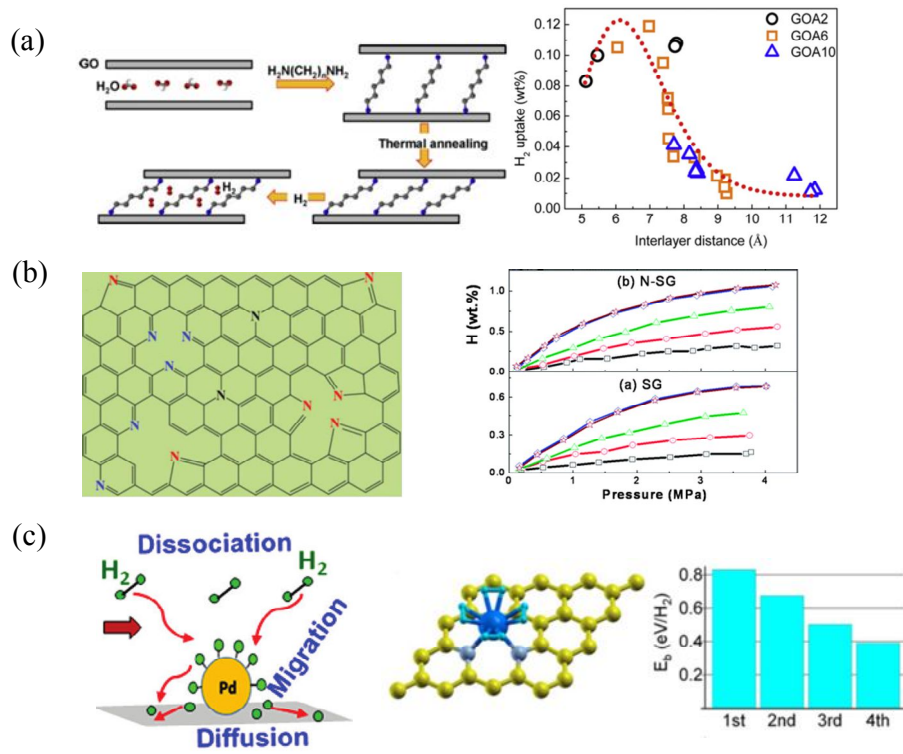


Figure 1. 13. Approaches to improve hydrogen storage capacity through (a) functionalization,[132] (b) doping,[136, 137] and (c) decoration.[138, 139]

1.3. Scope and aim of the present work

To solve the limitations in existing approaches to various applications, a strategic design of CDG-based materials is necessary. Thus, a tailor-fitted preparation method of CDG-based materials for specific-applications will be provided in this work.

Chapter 2 provides a preparation method for CDG in TCF applications through a simultaneous reduction and doping using lithium naphthalenide (LN). A chemical reduction with LN not only has practical meaning (reaction rapidly occurs under room temperature), but also maintains integrity and film flexibility. Moreover, reduction with controlled washing can induce chemical doping of the lithium containing molecule. Through this strategy, CDG shows good electrical conductivity, transparency, and flexibility, making it more suitable for future generations of TCF applications.

Chapter 3 shows the preparation of CDG-based composite through functionalization using diol and reduction for the GBL application. Edge-to-edge cross-linking of CDG-based composites are proved to be more effective than uncross-linked CDG-based composites in shielding moisture due to the moisture's increased diffusion path. Thus, produced CDG shows less permeability, which makes it applicable for GBL applications.

Chapter 4 discusses the preparation of CDG through functionalization, doping, and reduction by polydopamine (PD) and platinum (Pt) decoration for the hydrogen storage application. Polydopamine plays multi-roles as a reducing agent and a metal dispersing agent. By tailoring the functionalization degree of PD, the SSA of PD-functionalized CDG as well as the size, distribution, and amount of decorated Pt can be controlled. Therefore, the produced CDG shows outstanding hydrogen uptake at ambient conditions, which makes it beneficial in hydrogen storage applications.

1.4. References

- [1] K. S. Novoselov, A. K. Geim, S. V. Morozov, D. Jiang, Y. Zhang, S. V. Dubonos, I. V. Grigorieva, A. A. Firsov, *Science* **2004**, *306*, 666.
- [2] R. R. Nair, P. Blake, A. N. Grigorenko, K. S. Novoselov, T. J. Booth, T. Stauber, N. M. R. Peres, A. K. Geim, *Science* **2008**, *320*, 1308.
- [3] X. Li, Y. Zhu, W. Cai, M. Borysiak, B. Han, D. Chen, R. D. Piner, L. Colombo, R. S. Ruoff, *Nano Lett.* **2009**, *9*, 4359.
- [4] C. Lee, X. Wei, J. W. Kysar, J. Hone, *Science* **2008**, *321*, 385.
- [5] V. Berry, *Carbon* **2013**, *62*, 1.
- [6] K. I. Bolotin, K. J. Sikes, Z. Jiang, M. Klima, G. Fudenberg, J. Hone, P. Kim, H. L. Stormer, *Solid State Commun.* **2008**, *146*, 351.
- [7] N. Savage, *Nature* **2012**, *483*, S30.
- [8] J.-H. Chen, C. Jang, S. Xiao, M. Ishigami, M. S. Fuhrer, *Nat Nano* **2008**, *3*, 206.
- [9] A. A. Balandin, S. Ghosh, W. Bao, I. Calizo, D. Teweldebrhan, F. Miao, C. N. Lau, *Nano Lett.* **2008**, *8*, 902.
- [10] F. Bonaccorso, L. Colombo, G. Yu, M. Stoller, V. Tozzini, A. C. Ferrari, R. S. Ruoff, V. Pellegrini, *Science* **2015**, *347*.
- [11] M. D. Stoller, S. Park, Y. Zhu, J. An, R. S. Ruoff, *Nano Lett.* **2008**, *8*, 3498.
- [12] Y.-M. Lin, C. Dimitrakopoulos, K. A. Jenkins, D. B. Farmer, H.-Y. Chiu, A. Grill, P. Avouris, *Science* **2010**, *327*, 662.
- [13] H. Chang, Z. Sun, Q. Yuan, F. Ding, X. Tao, F. Yan, Z. Zheng, *Adv. Mater.* **2010**, *22*, 4872.
- [14] K. S. Kim, Y. Zhao, H. Jang, S. Y. Lee, J. M. Kim, K. S. Kim, J.-H. Ahn, P. Kim, J.-Y. Choi, B. H. Hong, *Nature* **2009**, *457*, 706.
- [15] J.-H. Chang, W.-H. Lin, P.-C. Wang, J.-I. Taur, T.-A. Ku, W.-T. Chen, S.-J. Yan,

- C.-I. Wu, *Sci. Rep.* **2015**, 5.
- [16] Y. U. Jung, K.-W. Park, S.-T. Hur, S.-W. Choi, S. J. Kang, *Liq. Cryst.* **2013**, 41, 101.
- [17] H. Yamaguchi, J. Granstrom, W. Nie, H. Sojoudi, T. Fujita, D. Voiry, M. Chen, G. Gupta, A. D. Mohite, S. Graham, M. Chhowalla, *Advanced Energy Materials* **2014**, 4, n/a.
- [18] T. Kim, J. H. Kang, S. J. Yang, S. J. Sung, Y. S. Kim, C. R. Park, *Energy Environ. Sci.* **2014**, 7, 3403.
- [19] Z. Liu, J. Li, F. Yan, *Adv. Mater.* **2013**, 25, 4296.
- [20] L. Xiao, D. Wu, S. Han, Y. Huang, S. Li, M. He, F. Zhang, X. Feng, *ACS Appl Mater Interfaces* **2013**, 5, 3764.
- [21] X. Zang, Q. Chen, P. Li, Y. He, X. Li, M. Zhu, X. Li, K. Wang, M. Zhong, D. Wu, H. Zhu, *Small* **2014**, 10, 2583.
- [22] W. Lee, J. U. Lee, B. M. Jung, J.-H. Byun, J.-W. Yi, S.-B. Lee, B.-S. Kim, *Carbon* **2013**, 65, 296.
- [23] X. Lee, T. Yang, X. Li, R. Zhang, M. Zhu, H. Zhang, D. Xie, J. Wei, M. Zhong, K. Wang, D. Wu, Z. Li, H. Zhu, *Appl. Phys. Lett.* **2013**, 102.
- [24] C. S. Boland, U. Khan, C. Backes, A. O'Neill, J. McCauley, S. Duane, R. Shanker, Y. Liu, I. Jurewicz, A. B. Dalton, J. N. Coleman, *ACS Nano* **2014**, 8, 8819.
- [25] J. J. Bae, S. C. Lim, G. H. Han, Y. W. Jo, D. L. Doung, E. S. Kim, S. J. Chae, T. Q. Huy, N. Van Luan, Y. H. Lee, *Adv. Funct. Mater.* **2012**, 22, 4819.
- [26] Z. Yan, G. Liu, J. M. Khan, A. A. Balandin, *Nat. Commun.* **2012**, 3, 827.
- [27] X. Shi, H. Chang, S. Chen, C. Lai, A. Khademhosseini, H. Wu, *Adv. Funct. Mater.* **2012**, 22, 751.
- [28] X. Li, W. Cai, J. An, S. Kim, J. Nah, D. Yang, R. Piner, A. Velamakanni, I. Jung, E.

- Tutuc, S. K. Banerjee, L. Colombo, R. S. Ruoff, *Science* **2009**, 324, 1312.
- [29] S. Bae, H. Kim, Y. Lee, X. Xu, J.-S. Park, Y. Zheng, J. Balakrishnan, T. Lei, H. Ri Kim, Y. I. Song, Y.-J. Kim, K. S. Kim, B. Ozyilmaz, J.-H. Ahn, B. H. Hong, S. Iijima, *Nat Nano* **2010**, 5, 574.
- [30] C. Virojanadara, M. Syväjarvi, R. Yakimova, L. I. Johansson, A. A. Zakharov, T. Balasubramanian, *Physical Review B* **2008**, 78, 245403.
- [31] Y. Hernandez, V. Nicolosi, M. Lotya, F. M. Blighe, Z. Sun, S. De, I. T. McGovern, B. Holland, M. Byrne, Y. K. Gun'Ko, J. J. Boland, P. Niraj, G. Duesberg, S. Krishnamurthy, R. Goodhue, J. Hutchison, V. Scardaci, A. C. Ferrari, J. N. Coleman, *Nat Nano* **2008**, 3, 563.
- [32] H. C. Schniepp, J.-L. Li, M. J. McAllister, H. Sai, M. Herrera-Alonso, D. H. Adamson, R. K. Prud'homme, R. Car, D. A. Saville, I. A. Aksay, *J. Phys. Chem. B* **2006**, 110, 8535.
- [33] L. M. Viculis, J. J. Mack, R. B. Kaner, *Science* **2003**, 299, 1361.
- [34] L. Jiao, L. Zhang, X. Wang, G. Diankov, H. Dai, *Nature* **2009**, 458, 877.
- [35] K. S. Novoselov, V. I. Falko, L. Colombo, P. R. Gellert, M. G. Schwab, K. Kim, *Nature* **2012**, 490, 192.
- [36] B. C. Brodie, *Philosophical Transactions of the Royal Society of London* **1859**, 149, 249.
- [37] L. Staudenmaier, *Berichte der deutschen chemischen Gesellschaft* **1898**, 31, 1481.
- [38] O. C. Compton, S. T. Nguyen, *Small* **2010**, 6, 711.
- [39] W. S. Hummers, R. E. Offeman, *J. Am. Chem. Soc.* **1958**, 80, 1339.
- [40] N. I. Kovtyukhova, P. J. Ollivier, B. R. Martin, T. E. Mallouk, S. A. Chizhik, E. V. Buzaneva, A. D. Gorchinskiy, *Chem. Mater.* **1999**, 11, 771.
- [41] C.-Y. Su, Y. Xu, W. Zhang, J. Zhao, X. Tang, C.-H. Tsai, L.-J. Li, *Chem. Mater.*

- 2009**, *21*, 5674.
- [42] F. Kim, J. Luo, R. Cruz-Silva, L. J. Cote, K. Sohn, J. Huang, *Adv. Funct. Mater.* **2010**, *20*, 2867.
- [43] S. J. Yang, T. Kim, H. Jung, C. R. Park, *Carbon* **2013**, *53*, 73.
- [44] Y. Zhu, S. Murali, M. D. Stoller, A. Velamakanni, R. D. Piner, R. S. Ruoff, *Carbon* **2010**, *48*, 2118.
- [45] L. J. Cote, R. Cruz-Silva, J. Huang, *J. Am. Chem. Soc.* **2009**, *131*, 11027.
- [46] S. Stankovich, D. A. Dikin, R. D. Piner, K. A. Kohlhaas, A. Kleinhammes, Y. Jia, Y. Wu, S. T. Nguyen, R. S. Ruoff, *Carbon* **2007**, *45*, 1558.
- [47] W. Gao, L. B. Alemany, L. J. Ci, P. M. Ajayan, *Nat. Chem.* **2009**, *1*, 403.
- [48] H. Jung, S. J. Yang, T. Kim, J. H. Kang, C. R. Park, *Carbon* **2013**, *63*, 165.
- [49] M. Zhou, Y. Wang, Y. Zhai, J. Zhai, W. Ren, F. Wang, S. Dong, *Chemistry – A European Journal* **2009**, *15*, 6116.
- [50] S. Pei, H.-M. Cheng, *Carbon* **2012**, *50*, 3210.
- [51] G. Williams, B. Seger, P. V. Kamat, *ACS Nano* **2008**, *2*, 1487.
- [52] U. Hofmann, R. Holst, *Berichte der deutschen chemischen Gesellschaft (A and B Series)* **1939**, *72*, 754.
- [53] G. Ruess, *Monatsh Chem.* **1946**, *76*, 381.
- [54] W. Scholz, H. P. Boehm, *Z. Anorg. Allg. Chem.* **1969**, *369*, 327.
- [55] T. Nakajima, A. Mabuchi, R. Hagiwara, *Carbon* **1988**, *26*, 357.
- [56] A. Lerf, H. He, M. Forster, J. Klinowski, *J. Phys. Chem. B* **1998**, *102*, 4477.
- [57] D. R. Dreyer, S. Park, C. W. Bielawski, R. S. Ruoff, *Chem. Soc. Rev.* **2010**, *39*, 228.
- [58] K. P. Loh, Q. Bao, G. Eda, M. Chhowalla, *Nat. Chem.* **2010**, *2*, 1015.
- [59] K. Erickson, R. Erni, Z. Lee, N. Alem, W. Gannett, A. Zettl, *Adv. Mater.* **2010**, *22*,

4467.

- [60] C. Gómez-Navarro, J. C. Meyer, R. S. Sundaram, A. Chuvilin, S. Kurasch, M. Burghard, K. Kern, U. Kaiser, *Nano Lett.* **2010**, *10*, 1144.
- [61] X. Gao, J. Jang, S. Nagase, *J. Phys. Chem. C* **2010**, *114*, 832.
- [62] M. C. Kim, G. S. Hwang, R. S. Ruoff, *The Journal of Chemical Physics* **2009**, *131*, 064704.
- [63] H.-J. Shin, K. K. Kim, A. Benayad, S.-M. Yoon, H. K. Park, I.-S. Jung, M. H. Jin, H.-K. Jeong, J. M. Kim, J.-Y. Choi, Y. H. Lee, *Adv. Funct. Mater.* **2009**, *19*, 1987.
- [64] C. K. Chua, M. Pumera, *Chem. Soc. Rev.* **2014**, *43*, 291.
- [65] W. H. Brown, T. Poon, *Introduction to Organic Chemistry*, John Wiley & Sons, Hoboken NJ **2005**.
- [66] S. Pei, J. Zhao, J. Du, W. Ren, H.-M. Cheng, *Carbon* **2010**, *48*, 4466.
- [67] I. K. Moon, J. Lee, R. S. Ruoff, H. Lee, *Nat. Commun.* **2010**, *1*, 73.
- [68] A. Ambrosi, C. K. Chua, A. Bonanni, M. Pumera, *Chem. Mater.* **2012**, *24*, 2292.
- [69] D. Kim, S. J. Yang, Y. S. Kim, H. Jung, C. R. Park, *Carbon* **2012**, *50*, 3229.
- [70] M. J. Fernández-Merino, L. Guardia, J. I. Paredes, S. Villar-Rodil, P. Solís-Fernández, A. Martínez-Alonso, J. M. D. Tascón, *J. Phys. Chem. C* **2010**, *114*, 6426.
- [71] Z.-J. Fan, W. Kai, J. Yan, T. Wei, L.-J. Zhi, J. Feng, Y.-m. Ren, L.-P. Song, F. Wei, *ACS Nano* **2010**, *5*, 191.
- [72] J. Liu, S. Fu, B. Yuan, Y. Li, Z. Deng, *J. Am. Chem. Soc.* **2010**, *132*, 7279.
- [73] Q. Tang, Z. Zhou, Z. Chen, *Nanoscale* **2013**, *5*, 4541.
- [74] M. J. McAllister, J.-L. Li, D. H. Adamson, H. C. Schniepp, A. A. Abdala, J. Liu, M. Herrera-Alonso, D. L. Milius, R. Car, R. K. Prud'homme, I. A. Aksay, *Chem. Mater.* **2007**, *19*, 4396.

- [75] C. Mattevi, G. Eda, S. Agnoli, S. Miller, K. A. Mkhoyan, O. Celik, D. Mastrogiovanni, G. Granozzi, E. Garfunkel, M. Chhowalla, *Adv. Funct. Mater.* **2009**, *19*, 2577.
- [76] X. Li, G. Zhang, X. Bai, X. Sun, X. Wang, E. Wang, H. Dai, *Nat Nano* **2008**, *3*, 538.
- [77] W. Lv, D.-M. Tang, Y.-B. He, C.-H. You, Z.-Q. Shi, X.-C. Chen, C.-M. Chen, P.-X. Hou, C. Liu, Q.-H. Yang, *ACS Nano* **2009**, *3*, 3730.
- [78] H.-B. Zhang, J.-W. Wang, Q. Yan, W.-G. Zheng, C. Chen, Z.-Z. Yu, *J. Mater. Chem.* **2011**, *21*, 5392.
- [79] S. J. Yang, J. H. Kang, H. Jung, T. Kim, C. R. Park, *J. Mater. Chem. A* **2013**, *1*, 9427.
- [80] Z.-B. Liu, Y.-F. Xu, X.-Y. Zhang, X.-L. Zhang, Y.-S. Chen, J.-G. Tian, *J. Phys. Chem. B* **2009**, *113*, 9681.
- [81] Z. Liu, J. T. Robinson, X. Sun, H. Dai, *J. Am. Chem. Soc.* **2008**, *130*, 10876.
- [82] Y. Liu, D. Yu, C. Zeng, Z. Miao, L. Dai, *Langmuir* **2010**, *26*, 6158.
- [83] L. M. Veca, F. Lu, M. J. Mezziani, L. Cao, P. Zhang, G. Qi, L. Qu, M. Shrestha, Y.-P. Sun, *Chem. Commun.* **2009**, 2565.
- [84] D. Yu, Y. Yang, M. Durstock, J.-B. Baek, L. Dai, *ACS Nano* **2010**, *4*, 5633.
- [85] J. W. Burrell, S. Gadipelli, J. Ford, J. M. Simmons, W. Zhou, T. Yildirim, *Angew. Chem. Int. Ed.* **2010**, *49*, 8902.
- [86] H. Yang, C. Shan, F. Li, D. Han, Q. Zhang, L. Niu, *Chem. Commun.* **2009**, *0*, 3880.
- [87] H. Yang, F. Li, C. Shan, D. Han, Q. Zhang, L. Niu, A. Ivaska, *J. Mater. Chem.* **2009**, *19*, 4632.
- [88] S. Park, D. A. Dikin, S. T. Nguyen, R. S. Ruoff, *J. Phys. Chem. C* **2009**, *113*, 15801.

- [89] S. Stankovich, R. D. Piner, S. T. Nguyen, R. S. Ruoff, *Carbon* **2006**, *44*, 3342.
- [90] J. U. Lee, W. Lee, J. W. Yi, S. S. Yoon, S. B. Lee, B. M. Jung, B. S. Kim, J. H. Byun, *J. Mater. Chem. A* **2013**, *1*, 12893.
- [91] C.-H. Lu, H.-H. Yang, C.-L. Zhu, X. Chen, G.-N. Chen, *Angew. Chem. Int. Ed.* **2009**, *48*, 4785.
- [92] Y. Wang, Z. Li, D. Hu, C.-T. Lin, J. Li, Y. Lin, *J. Am. Chem. Soc.* **2010**, *132*, 9274.
- [93] X. Yang, X. Zhang, Z. Liu, Y. Ma, Y. Huang, Y. Chen, *J. Phys. Chem. C* **2008**, *112*, 17554.
- [94] X. Wang, G. Sun, P. Routh, D.-H. Kim, W. Huang, P. Chen, *Chem. Soc. Rev.* **2014**, *43*, 7067.
- [95] Z. Wen, X. Wang, S. Mao, Z. Bo, H. Kim, S. Cui, G. Lu, X. Feng, J. Chen, *Adv. Mater.* **2012**, *24*, 5610.
- [96] Y. Li, Y. Zhao, H. Cheng, Y. Hu, G. Shi, L. Dai, L. Qu, *J. Am. Chem. Soc.* **2012**, *134*, 15.
- [97] Y. Wang, Y. Shao, D. W. Matson, J. Li, Y. Lin, *ACS Nano* **2010**, *4*, 1790.
- [98] Z.-H. Sheng, L. Shao, J.-J. Chen, W.-J. Bao, F.-B. Wang, X.-H. Xia, *ACS Nano* **2011**, *5*, 4350.
- [99] Y. Liu, Q. Feng, N. Tang, X. Wan, F. Liu, L. Lv, Y. Du, *Carbon* **2013**, *60*, 549.
- [100] T. Van Khai, H. G. Na, D. S. Kwak, Y. J. Kwon, H. Ham, K. B. Shim, H. W. Kim, *J. Mater. Chem.* **2012**, *22*, 17992.
- [101] C. Zhang, N. Mahmood, H. Yin, F. Liu, Y. Hou, *Adv. Mater.* **2013**, *25*, 4932.
- [102] R. Li, Z. Wei, X. Gou, W. Xu, *RSC Advances* **2013**, *3*, 9978.
- [103] Z.-H. Sheng, H.-L. Gao, W.-J. Bao, F.-B. Wang, X.-H. Xia, *J. Mater. Chem.* **2012**, *22*, 390.
- [104] Z.-S. Wu, W. Ren, L. Xu, F. Li, H.-M. Cheng, *ACS Nano* **2011**, *5*, 5463.

- [105] Z. Yang, Z. Yao, G. Li, G. Fang, H. Nie, Z. Liu, X. Zhou, X. a. Chen, S. Huang, *ACS Nano* **2012**, *6*, 205.
- [106] J. Liang, Y. Jiao, M. Jaroniec, S. Z. Qiao, *Angew. Chem. Int. Ed.* **2012**, *51*, 11496.
- [107] S. Wang, L. Zhang, Z. Xia, A. Roy, D. W. Chang, J.-B. Baek, L. Dai, *Angew. Chem. Int. Ed.* **2012**, *51*, 4209.
- [108] C. N. R. Rao, A. K. Sood, K. S. Subrahmanyam, A. Govindaraj, *Angew. Chem. Int. Ed.* **2009**, *48*, 7752.
- [109] J. Zhao, S. Pei, W. Ren, L. Gao, H.-M. Cheng, *ACS Nano* **2010**, *4*, 5245.
- [110] V. C. Tung, L.-M. Chen, M. J. Allen, J. K. Wassei, K. Nelson, R. B. Kaner, Y. Yang, *Nano Lett.* **2009**, *9*, 1949.
- [111] E. Yoo, T. Okata, T. Akita, M. Kohyama, J. Nakamura, I. Honma, *Nano Lett.* **2009**, *9*, 2255.
- [112] J. Zhang, X. Liu, H. Zhou, X. Yan, Y. Liu, A. Yuan, *RSC Advances* **2014**, *4*, 28908.
- [113] C. Xu, X. Wang, J. Zhu, *J. Phys. Chem. C* **2008**, *112*, 19841.
- [114] K. Jasuja, V. Berry, *ACS Nano* **2009**, *3*, 2358.
- [115] G. Goncalves, P. A. A. P. Marques, C. M. Granadeiro, H. I. S. Nogueira, M. K. Singh, J. Grácio, *Chem. Mater.* **2009**, *21*, 4796.
- [116] S. Myung, J. Park, H. Lee, K. S. Kim, S. Hong, *Adv. Mater.* **2010**, *22*, 2045.
- [117] L.-S. Zhang, L.-Y. Jiang, H.-J. Yan, W. D. Wang, W. Wang, W.-G. Song, Y.-G. Guo, L.-J. Wan, *J. Mater. Chem.* **2010**, *20*, 5462.
- [118] H. Wang, L.-F. Cui, Y. Yang, H. Sanchez Casalongue, J. T. Robinson, Y. Liang, Y. Cui, H. Dai, *J. Am. Chem. Soc.* **2010**, *132*, 13978.
- [119] W. Wei, S. Yang, H. Zhou, I. Lieberwirth, X. Feng, K. Mullen, *Adv. Mater.*

- 2013**, *25*, 2909.
- [120] J. Zhu, T. Zhu, X. Zhou, Y. Zhang, X. W. Lou, X. Chen, H. Zhang, H. H. Hng, Q. Yan, *Nanoscale* **2011**, *3*, 1084.
- [121] V. Chandra, J. Park, Y. Chun, J. W. Lee, I.-C. Hwang, K. S. Kim, *ACS Nano* **2010**, *4*, 3979.
- [122] C. Chen, W. Cai, M. Long, B. Zhou, Y. Wu, D. Wu, Y. Feng, *ACS Nano* **2010**, *4*, 6425.
- [123] X.-Y. Zhang, H.-P. Li, X.-L. Cui, Y. Lin, *J. Mater. Chem.* **2010**, *20*, 2801.
- [124] Q. Zheng, W. H. Ip, X. Lin, N. Yousefi, K. K. Yeung, Z. Li, J.-K. Kim, *ACS Nano* **2011**, *5*, 6039.
- [125] A. Kasry, M. A. Kuroda, G. J. Martyna, G. S. Tulevski, A. A. Bol, *ACS Nano* **2010**, *4*, 3839.
- [126] N. Jung, N. Kim, S. Jockusch, N. J. Turro, P. Kim, L. Brus, *Nano Lett.* **2009**, *9*, 4133.
- [127] A. Vitale, S. Merlo, G. Rizza, G. Melilli, M. Sangermano, *Macromol. Chem. Phys.* **2014**, *215*, 1588.
- [128] Y. Su, V. G. Kravets, S. L. Wong, J. Waters, A. K. Geim, R. R. Nair, *Nat. Commun.* **2014**, *5*, 4843.
- [129] O. C. Compton, S. Kim, C. Pierre, J. M. Torkelson, S. T. Nguyen, *Adv. Mater.* **2010**, *22*, 4759.
- [130] I. H. Tseng, Y.-F. Liao, J.-C. Chiang, M.-H. Tsai, *Mater. Chem. Phys.* **2012**, *136*, 247.
- [131] K. S. W. S. S.J.Gregg, *Adsorption, Surface Area and Porosity*, Academic Press, **1982**.
- [132] B. H. Kim, W. G. Hong, H. R. Moon, S. M. Lee, J. M. Kim, S. Kang, Y. Jun,

- H. J. Kim, *Int. J. Hydrogen Energy* **2012**, *37*, 14217.
- [133] G. Srinivas, J. W. Burrell, J. Ford, T. Yildirim, *J. Mater. Chem.* **2011**, *21*, 11323.
- [134] Y. G. Zhou, X. T. Zu, F. Gao, J. L. Nie, H. Y. Xiao, *J. Appl. Phys.* **2009**, *105*, 014309.
- [135] L. Firlej, B. Kuchta, C. Wexler, P. Pfeifer, *Adsorption* **2009**, *15*, 312.
- [136] V. B. Parambath, R. Nagar, S. Ramaprabhu, *Langmuir* **2012**, *28*, 7826.
- [137] B. P. Vinayan, R. Nagar, S. Ramaprabhu, *J. Mater. Chem. A* **2013**, *1*, 11192.
- [138] V. B. Parambath, R. Nagar, K. Sethupathi, S. Ramaprabhu, *J. Phys. Chem. C* **2011**, *115*, 15679.
- [139] G. Kim, S.-H. Jhi, N. Park, *Appl. Phys. Lett.* **2008**, *92*, 013106.

Part II

Tailor-fitted preparation and applications of CDG- based materials

Chapter 2. Chemically reduced GO through reduction and doping using lithium naphthalenide (LN)

2.1. Introduction

The transparent conductive film (TCF) is electrically conductive and optically transparent in the visible light range. It is a key component in optoelectronics such as displays, solar cells, touch panels, and so on. With the rise of flexible devices, electrical conductivity, transparency, and flexibility are important factors in TCF. In this aspect, graphene has attracted attention as a promising TCF material.

The graphene size, π -conjugation restoration, and charge carrier modulation should be considered when designing graphene for TCF applications. Several research focusing on large-size graphene preparation for TCF have been reported.[1-3] The charge carrier modulation by chemical doping was also widely studied using nitric acid, thionyl chloride, bromine, iodine, and so on.[2, 4, 5] However, few research mainly focused on π -conjugation restoration was found, although it is the most important step in determining the electrical conductivity. Therefore, reduction which is perfectly suitable for TCF application should be comprehensively investigated.

Chemical reduction methods use reducing agents such as hydrazine [6], sodium borohydride (NaBH_4) [7], hydrohalic acid [8], hydroquinone [9], iron nanoparticles [10], and ascorbic acid [11]. Although these chemicals are promising reducing agents, they require elevated (80–120 °C) or low (–33 °C) temperatures and long reaction times (1–24 hours, Table 1) [6-8, 12]. In addition to the drawback of these severe reduction conditions, multi-step processes are sometimes required to achieve effective reduction [7]. To overcome these limitations, considerable effort has been applied to the development of room-temperature reduction reactions [10, 13-15]. However,

reduction times at room temperature are generally longer than those of elevated temperature reduction reactions, as shown in Table 2.1. In addition, most of reductants damage to integrity or flexibility of reduced graphene oxide (rGO) film, which hinders their use in TCF application. Hence, reducing agents that can reduce GO within short periods of time under ambient conditions are still needed for practical TCF application.

Table 2. 1. Comparison of the synthetic conditions and measured parameters for the graphene chemically prepared using various reducing agents

Reducing agent	Reduction temperature (°C)	Reduction time ^a (hr)	C/O ^b	I _D /I _G ^d	Ref.
NaBH ₄ , H ₂ SO ₄	80, 120	1, 12	8.57	1.00	[7]
Hydrazine hydrate	100	24	10.3 ^c	> 1	[6]
HI	100	1	> 12	> 1	[8]
Hydrazine and ammonia	95	1	Unknown	Unknown	[16]
Ascorbic acid	80	1	Unknown	Unknown	[11]
Anhydrous hydrazine	80	2.5	Unknown	Unknown	[17]
Liquid ammonia and Li-33		Overnight	Unknown	Unknown	[12]
NaBH ₄	Unknown	2	≤ 8.6	> 1	[18]
H ₂ SO ₄	RT, 120	24, 12	Unknown	1.75	[13]
Hydrazine monohydrate	40	18	Unknown	Unknown	[15]
Fe and HCl	RT	6	7.9	0.32	[10]
Hydroquinone	Unknown	20	Unknown	> 2	[9]
Anhydrous hydrazine	Unknown	1 week	12.02 ^c	> 1	[14]

Lithium naphthalenide RT	10 min	8.86 ^c (6.66)	1.11	Present work
--------------------------	--------	-----------------------------	------	-----------------

^a Time used for reduction (values are given in units of hours, unless indicated otherwise).

^b XPS measurements; the reduction step was not followed by further treatment.

^c Elemental analysis.

^d Raman spectroscopy measurements; the reduction step was not followed by further treatment.

Because electrical property is not sufficient for use in TCF with only reduction, further treatments such as chemical doping are generally used. Thus, reducing agents that can act as chemical dopants are preferable.

We developed a one-step, ultrafast (less than 10 min) method of reducing GO using lithium naphthalenide (LN) as the reducing agent. Through this method, rGO is produced with remaining integrity, substrate adhesion, and flexibility. Our protocol is not only the fastest room temperature reduction method reported to date, but also provides a simultaneous chemical doping with reduction that simply modifies the washing conditions. As a result, LN reduction and concurrent doping enables the tailor-fitted graphene preparation for TCF applications.

2.2. Experimental

2.2.1. Materials and reagents

Reagent-grade chemicals were purchased from Sigma-Aldrich. All other solvents used for preparing the dispersions were purchased from Daejung Chemicals and Metals Co.,

Ltd. All raw materials were used as received unless otherwise stated. Lithium was immersed in anhydrous tetrahydrofuran (THF) to remove mineral oil and to restore the luster of its surface. GO was produced from graphite using a modified Hummers' method [19] and dispersed in anhydrous THF by water bath sonication. All synthetic procedures described below were conducted at room temperature in a glove box purged with argon.

2.2.2. Synthesis of materials

2.2.2.1. Preparation of LN

LN was synthesized by following the procedure described previously, with slight modification [20-22]. Naphthalene was dissolved in anhydrous THF to prepare a 0.1 M solution. Twofold mole of lithium was added to the naphthalene solution and vigorous agitation was applied until the solution color turned dark green, indicating that the reaction had gone to completion.

2.2.2.2. Synthesis of rGO(LN_reduction time_M)

LN (25% v/v) was added to a GO suspension, the solution was stirred for a period of time, and the rGO was collected by filtration, repeatedly rinsed with methanol (MeOH), and vacuum dried at 60 °C for 24 hours.

2.2.2.3. Synthesis of rGO(LN_reduction time_T)

To improve the dispersibility and colloidal stability, the reduction reaction was carried out using a modified washing step. The procedure described above was used to prepare

rGO(LN_reduction time_T), except that the sample was rinsed with THF instead of MeOH.

2.2.2.4. Synthesis of rGO(H) and to rGO(S)

For comparison, rGO samples were obtained using other common reducing agents: hydrazine hydrate and NaBH₄ (with sulfuric acid). These reactions were conducted as described in the literature [6, 7].

2.2.2.5. Preparation procedure for fragility test

GO films were synthesized by vacuum filtration. The resulting GO films were immersed in three reducing agents; 35 wt% aqueous hydrazine solution, 0.2 M NaBH₄, and LN. In the fragility testing, the physical appearance of the films was examined after various reduction times (immersion times).

2.2.3. Fabrication of TCF

2.2.3.1. Fabrication of transparent conductive film

GO dispersions with various concentration were prepared by dispersing GO in DI water for 1h using bath sonicator. 0.3 ml of homogenous GO dispersion was spin-coated on bare glass which is washed with detergent, acetone, and isopropyl alcohol, followed by UV-ozone for 15 minutes. GO coated glass was dried on the hot plate and reduced using desired reducing agents, washed, and dried. For further nitric acid doping, dried rGO TCF was immersed in nitric acid for 2 seconds and dried.

2.2.3.2. Comparison of reduction effect on TCF

For comparison the effect of reducing agent on TCF, rGO TCFs reduced by various reducing agents were prepared. Thermally reduced rGO TCF was prepared by thermal treatment of GO film at 200°C for 10 minutes. Chemically reduce rGO TCFs were produced for 10 minutes at room temperature using 57 wt% hydroiodic acid (HI), 35 wt% of N₂H₄, 0.2M of NaBH₄, and LN, respectively.

2.2.4. Characterization

The LN reduction efficiency was investigated by examining the GO and rGO with X-ray photoelectron spectroscopy (XPS) measurements (AXIS-His, KRATOS), Fourier transform IR spectrophotometer (FTIR; Nicolet 6700, Thermo Scientific), elemental analysis (Flash2000, CE Instrument), powder X-ray diffraction (PXRD; D8 Advance, Bruker) using Ni-filtered Cu K α radiation ($\lambda = 0.154184$ nm), and thermogravimetric analysis (TGA; SDT Q600, TA Instruments). The morphologies of the resultant rGO were characterized by scanning electron microscopy (SEM; JSM-6700F, JEOL and MERLIN Compact, ZEISS), high-resolution transmission electron microscopy (HR-TEM; JEM-3000F, JEOL), and analytic transmission electron microscopy (Analytic TEM; Tecnai F20, FEI). The physical-chemical structure was analyzed with Raman Spectrometry (RAMANplus, Nanophoton). Electrical conductivity measurements of the free-standing rGO films were carried out with a four-point probe system (Cresbox, Napson Corporation). For TCF performance measurement, electrical sheet resistance was determined with a four-point probe (M4P 205, MS TECH), and optical transparency was measured using UV-Vis spectrometer (Cary 5000, Varian Inc.).

2.3. Characteristics and application

2.3.1. Characteristics

2.3.1.1. Validation of reduction efficiency

Previous methods for reducing GO to rGO have required long reaction times at elevated temperatures. In the present study, by using LN as the reducing agent, we prepared rGO at room temperature within 10 min. A scheme of the procedure is shown in Figure. 2.1. XPS was conducted to characterize the resultant rGO (Figure. 2.2). Deconvolution of the C1s core level with curve fitting methods revealed that the major functional groups in our GO sample included hydroxyl (C–OH) and epoxy (C–O–C) groups. These main functional groups and the carboxylate groups are largely eliminated by reduction, and the non-oxygenated carbon content in the aromatic rings (sp^3 and sp^2) increases due to the removal of the oxygen-containing groups, concurrent with the restoration of conjugated C=C bonds (Table S1). The presence of restored π -conjugated graphene is also supported by the narrowing of the sp^2 C and sp^3 C peaks in the XPS C1s spectra due to the decrease in the quantity of sp^3 hybridized carbon in rGO. These changes are summarized in Figure. 2.2c, which shows the changes in the relative ratios of these functional groups. These results are consistent with previous reports that LN induces the reductive cleavage of epoxy ketones in organic syntheses, especially when the lithium ion is coordinated with the oxygen atom in epoxy groups [23-26]. According to these reports and the observed decrease in the ratio of C–O–C/C–OH, we suggest that LN can be used to achieve the cleavage of graphene epoxy groups, followed by the deoxygenation of the remaining graphene hydroxyl groups.

In addition, LN has a stronger reducing capability than the commonly used reducing agents [7, 10], which means that the atomic C to O ratio (C/O) in rGO(LN_10min_M)

is as high as 8.86. This result is attributed to the fact that LN significantly reduces both O=C–O and C–O–C/C–OH groups, whereas other reducing agents (e.g. NaOH, NaBH₄) mainly affect the C–O–C/C–OH groups [18, 27, 28]. In virtue of the balanced reduction of the C–O–C/C–OH and O=C–O groups by LN, reductions with LN can be monitored in terms of the relative ratio of the oxygenated functional groups; according to this approach, the reduction of GO by LN appears to be complete after 10 min, as shown in Figure. 2.2d. To the best of our knowledge, this is the first report of a rapid one-pot room-temperature synthesis of rGO with a quality comparable to that produced by other methods.

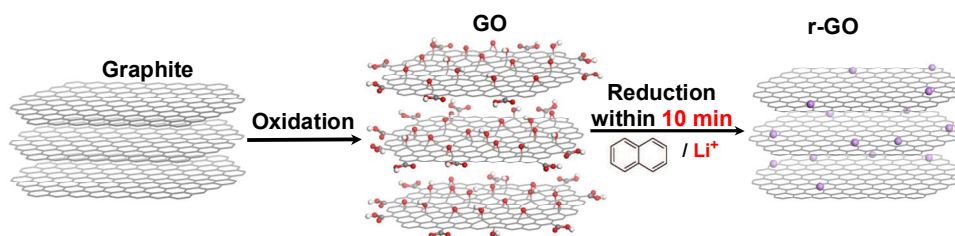


Figure 2. 1. Scheme of the ultrafast reduction of GO. Note that gray, white, red, and violet spheres indicate carbon, hydrogen, oxygen, and lithium-containing compounds, respectively.

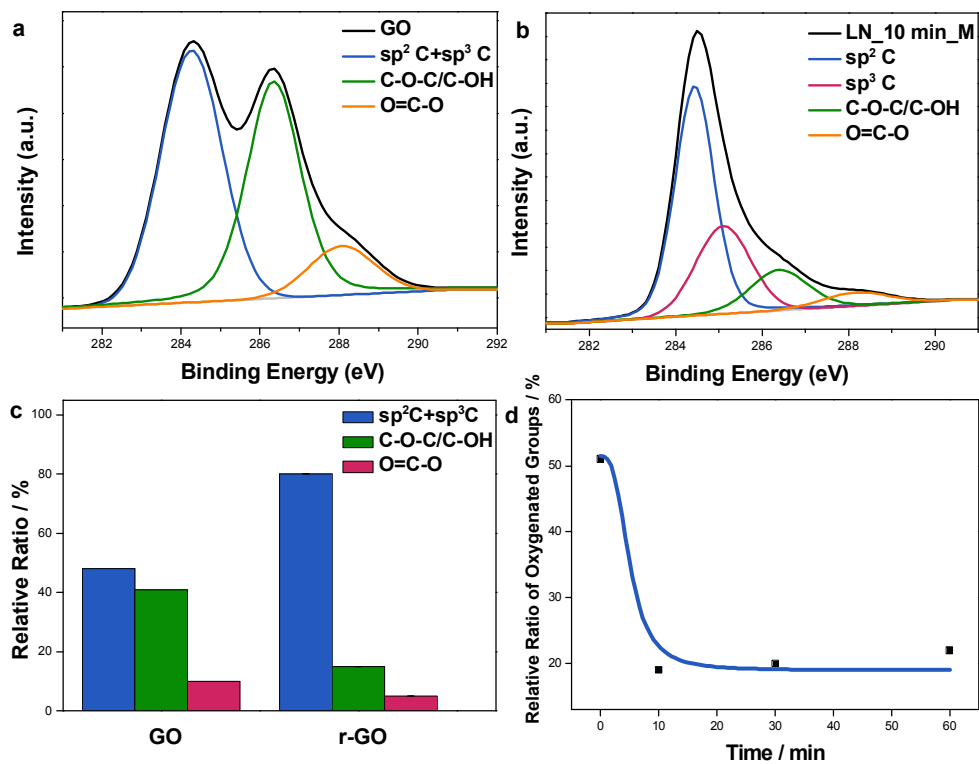


Figure 2. 2. XPS C1s spectra of (a) GO and (b) rGO(LN_10min_M). Relative ratios of (c) oxygen-containing functional groups to aromatic carbons in GO and MeOH-washed rGO, and (d) C-O-C/C-OH + O=C-O in MeOH-washed rGO as a function of the reduction time; the total carbon content was assumed to remain unchanged, 100%.

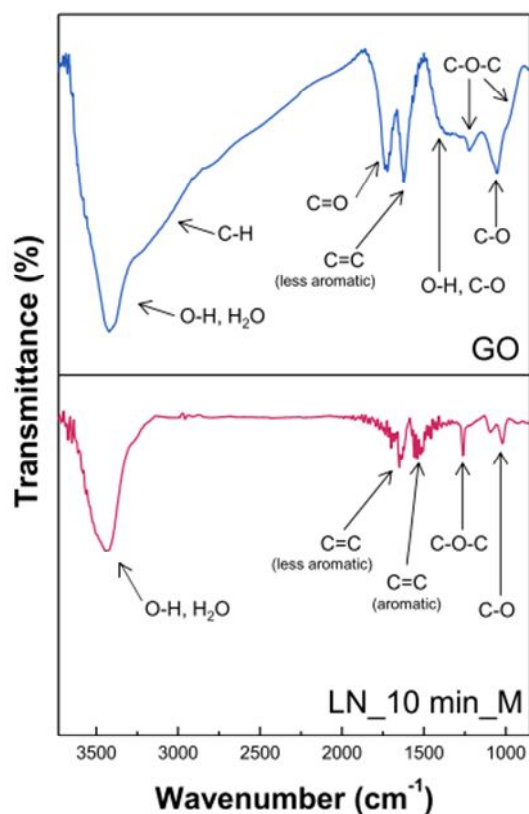


Figure 2. 3. FTIR spectra of GO and rGO (LN_10min_M).

To obtain more information about the mechanism of reduction by LN, we closely examined the synthesis of LN and the formation of rGO. Firstly, LN is formed by the concurrent oxidation of lithium and reduction of naphthalene, as discussed elsewhere [29-32]. The resultant nucleophilic naphthalene anion radical can easily attack electrophilic alpha-carbon of epoxide groups because the three-membered ring has significant angle strain [33]. The FTIR spectra of GO and rGO(LN_10min_M) indicate that a ring-opening process has occurred followed by deoxygenation (Figure. 2.3). GO produces a broad and intense band in the range 3000–3500 cm^{-1} (the O–H stretching of

hydroxyl groups and adsorbed water) and narrower bands at approximately 1720 cm^{-1} (C=O stretching), 1620 cm^{-1} (less aromatic C=C stretching), 1350 cm^{-1} (combined O–H bending and C–OH stretching), 1220 cm^{-1} (stretching of C–O–C), 1050 cm^{-1} (C–OH bending), and 1000 cm^{-1} (C–O–C bending) [34, 35]. Upon reduction, there are significant decreases in the absorption signals associated with the epoxide groups (1000 and 1220 cm^{-1}), O–H (1350 and 3000–3500 cm^{-1}), and C–OH (1050 and 1350 cm^{-1}), which indicates that the reduction with LN involves the ring-opening of the epoxide groups followed by deoxygenation of the hydroxyl groups. Note the appearance of a new band at 1560 cm^{-1} corresponding to aromatic C=C stretching, and that sp^3 hybridized C–H is almost undetectable after reduction, which is attributed to the recovery of the π -conjugated graphene basal plane [36]. The presence of π -conjugated graphene is also consistent with the XPS C1s spectra.

The XPS and FTIR spectra suggest the following possible reduction mechanism for the π -conjugation recovery. At first, reducing agent, LN, was formed by a redox reaction between lithium and naphthalene to make lithium cation and naphthalenide anion. As shown in Figure 2.4(a) and (b), epoxide ring-opening by a nucleophilic naphthalenide attack would follow because the naphthalene anion radical tends to transfer electrons to the epoxide group.[29] A naphthalene cluster (assembly of more than two naphthalene molecules) anion could be also formed from resonance stabilization due to a delocalized electron in the naphthalene cluster. Thus, an epoxide ring-opening can also occur by a naphthalene cluster anion (or combination of monomer anion and cluster anion).[37, 38] After this initial epoxide ring opening by naphthalenide (or cluster anion), rGO could be formed through two different pathways. The first is an electron transfer from another naphthalene monomer (or cluster) anion to a pre-formed radical by an epoxide ring opening, which leads to an aromatic C=C

bond formation and Li_2O (Figure 2.4(a)).[39, 40] Otherwise, the pre-formed radical can be transferred to a ring-opened oxygen functional group, making the LiO radical and rGO. The reactive LiO radicals react with each other to form Li_2O_2 through radical coupling (Figure 2.4(b)). As shown in Figure 2.4(c), Li_2O_2 can then react with CO_2 (from carboxylic acid in GO) to generate Li_2CO_3 . [41-43] However, further studies are needed to verify the underlying reduction mechanism.

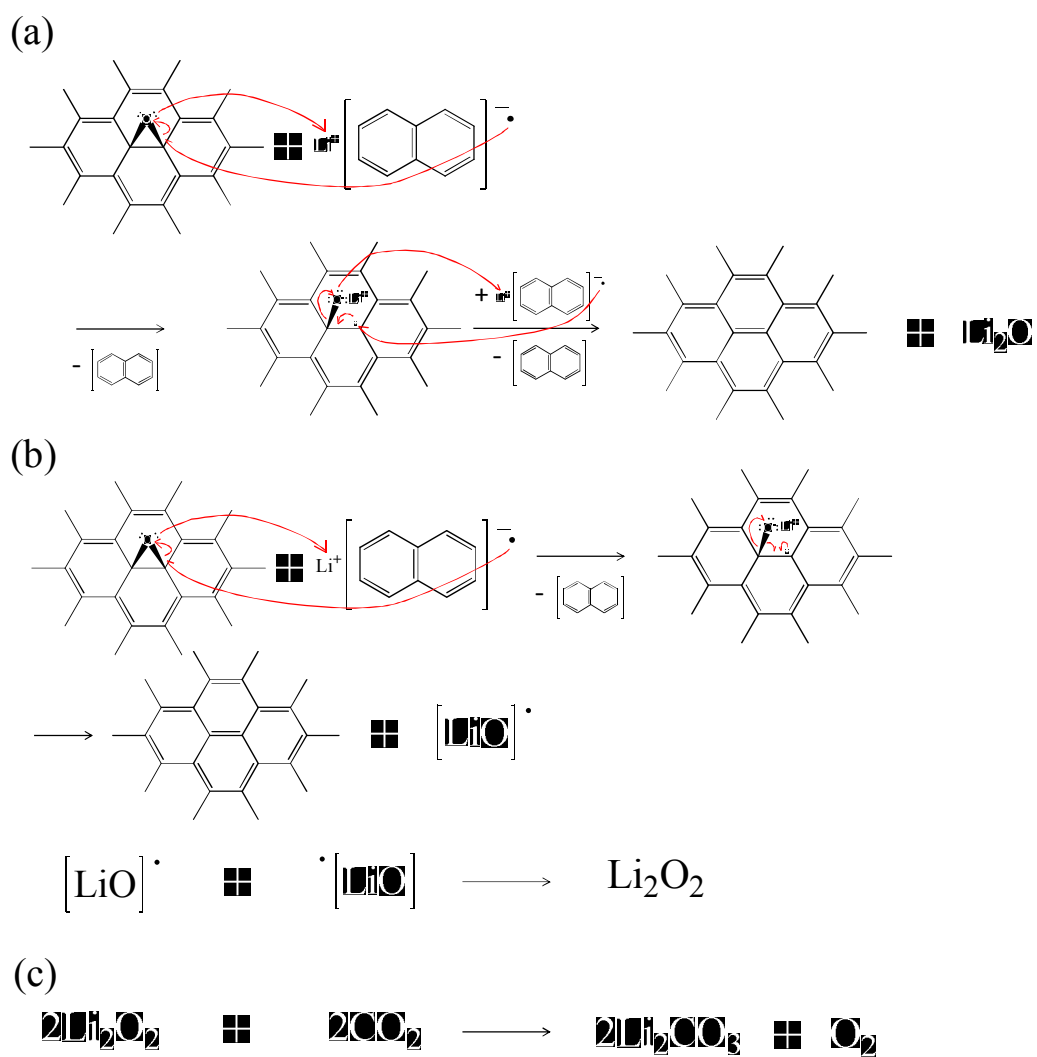


Figure 2. 4. The proposed GO reduction pathways to form (a) Li_2O , (b) Li_2O_2 , and (c) Li_2CO_3 as a by-product.

2.3.1.2. Crystal and physi-/chemical structure

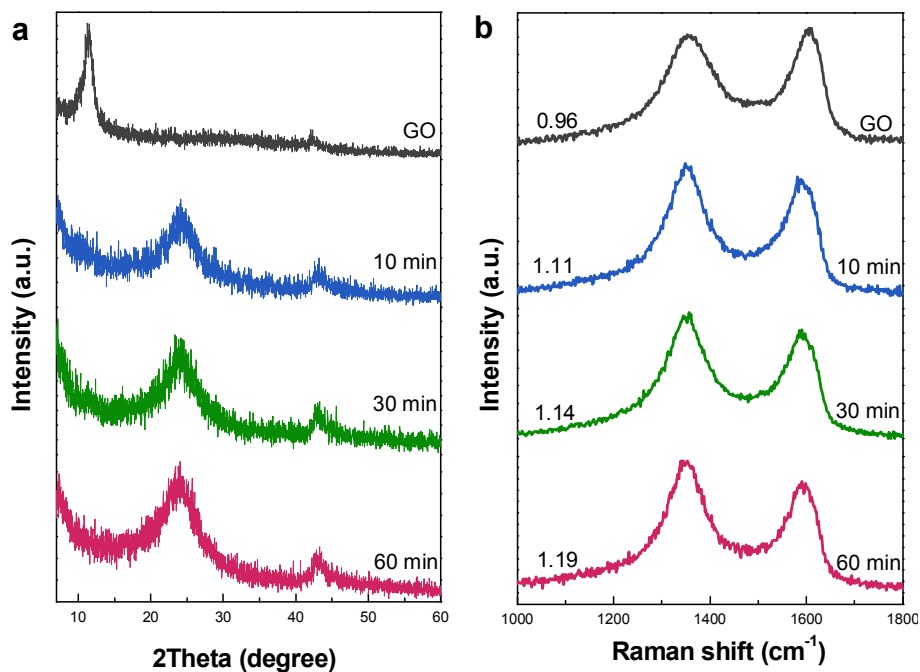


Figure 2. 5. (a) XRD patterns of GO, rGO(LN_10min_M), rGO(LN_30min_M), and rGO(LN_60min_M). (b) Raman spectra of GO, rGO(LN_10min_M), rGO(LN_30min_M), and rGO(LN_60min_M) with I_D/I_G .

The crystallographic changes observed upon reduction were confirmed with XRD analysis (Figure. 2.5a). GO produces two very sharp peaks at 11 and 42° due to the (001) and (10) planes respectively. Upon reduction of GO with LN, the peak at 11° disappears and a new broad band near 24° appears. The peak at 42° remains intact during the process. These results indicate that LN removes the oxygen-containing groups and recovers the graphitic structure, in good agreement with the reported structures [8, 10, 12]. No significant changes in the diffraction patterns are observed as

we move between the reduction time frames, which suggests that no further reduction reactions occur after 10 min.

Raman spectroscopy was used to characterize the reduction of GO by providing information about the defects, chemical functionalization, and in-plane crystalline sizes of the graphene sheet surfaces. The Raman spectrum (Figure. 2.5b) of rGO(LN_10min_M) contains typical D and G band peaks centered at 1357 and 1605 cm^{-1} respectively, which are similar to those observed for GO. The I_D/I_G ratio for rGO (1.11) is higher than that for GO (0.96) because the reduction of a sonication-assisted GO dispersion with an intensely reactive reagent can induce additional reactions, increase the in-plane defects, and increase the number of dangling edge atoms by reducing the lateral domain size [6, 10, 44, 45]. In addition, alkali metal doping (by the remaining lithium atoms) has been shown to increase the I_D/I_G ratio through a charge transfer process, although the phenomenon has not clearly been elucidated. The change in the I_D/I_G ratio upon reductive treatment is much smaller than the changes obtained upon reduction with other chemicals [9, 46]. The I_D/I_G ratio for rGO increases with longer LN exposure times, which indicates that shorter reduction times are preferable for obtaining less damaged rGO.

Electrical conductivity was also used to determine whether the reduction process is complete. As reported elsewhere, GO has insulating characteristics with a negligible conductivity that is too small to be detected in some cases. Likewise, the sheet resistance of GO is beyond the range of detection of four-point probe measurements. However, chemical reduction by LN restores π -conjugation, and the resistance of rGO becomes sufficiently low to be detected. The free-standing rGO(LN_10min_M) film has an electrical conductivity (424.03 S/m) that is comparable to or higher than those of rGO samples produced in previous studies, even without additional treatments such

as pelletizing or thermal processing [6, 36]. This observation demonstrates that LN reduction is a superior method for preparing graphene because of its better recovery of the π -conjugated structure.

2.3.1.3. Microstructure

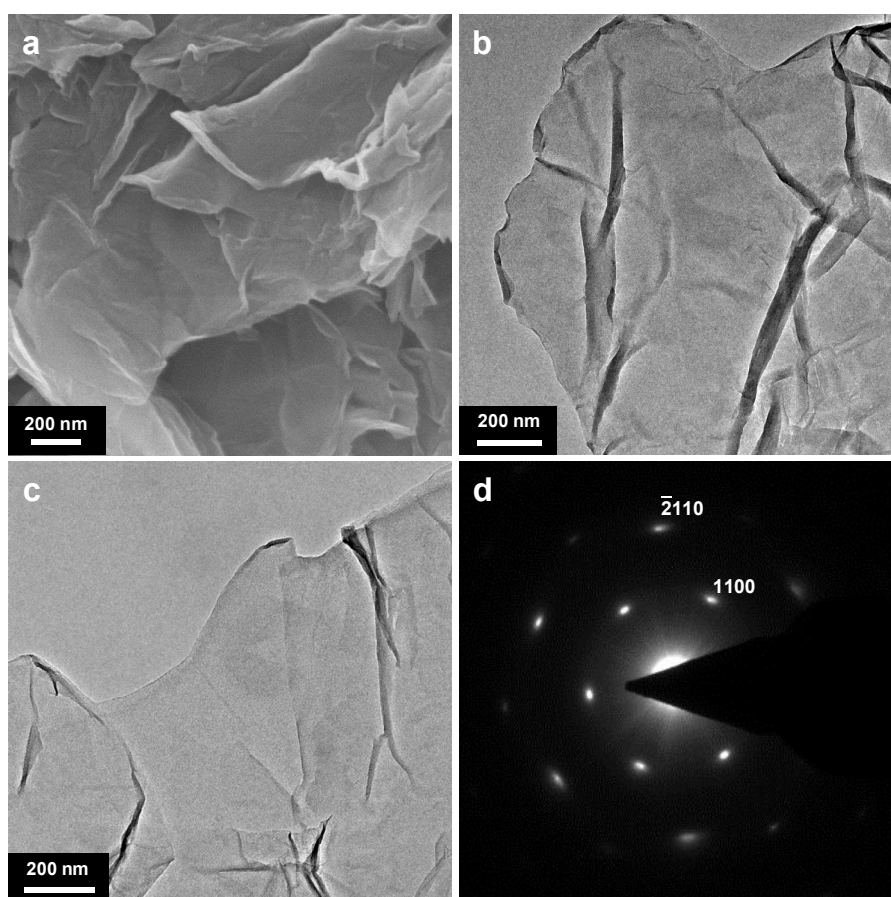


Figure 2. 6. (a) SEM image, (b),(c) TEM images, and (d) SAED pattern of rGO (LN_10min_M).

The morphology of rGO was characterized with SEM and TEM. The rGO in the SEM image in Figure 2.6 is fluffy in appearance, and each sheet edge appears to have rolled up. The folded and crumpled rGO in the TEM image resembles the thermodynamically stable morphology of a 2D membrane [9, 47]. We also found that the flimsy rGO consists of a few layered monolayer-like graphene sheets. The damage to the graphene sheets resulting from reduction was characterized by using selected area electron diffraction (SAED) analysis. rGO(LN_10min_M) produces one set of well-defined six-fold symmetric diffraction spots in the SAED pattern (Figure 2.6d) that is indicative of high crystallinity, whereas rGO without long-range ordering produces weak and ring-type diffraction patterns [7, 9]. The effectiveness of this reduction process is evident in the summary in Table 1 of the reduction temperatures, reduction times, C/O atomic ratios, and I_D/I_G ratios for rGO samples prepared by using a variety of chemical approaches. Interestingly, the reduction of GO with LN at room temperature produces single-layered graphene with a quality comparable to that obtained with other reducing agents, despite the ultrafast reaction time (10 min).

2.3.1.4. Fragility and flexibility

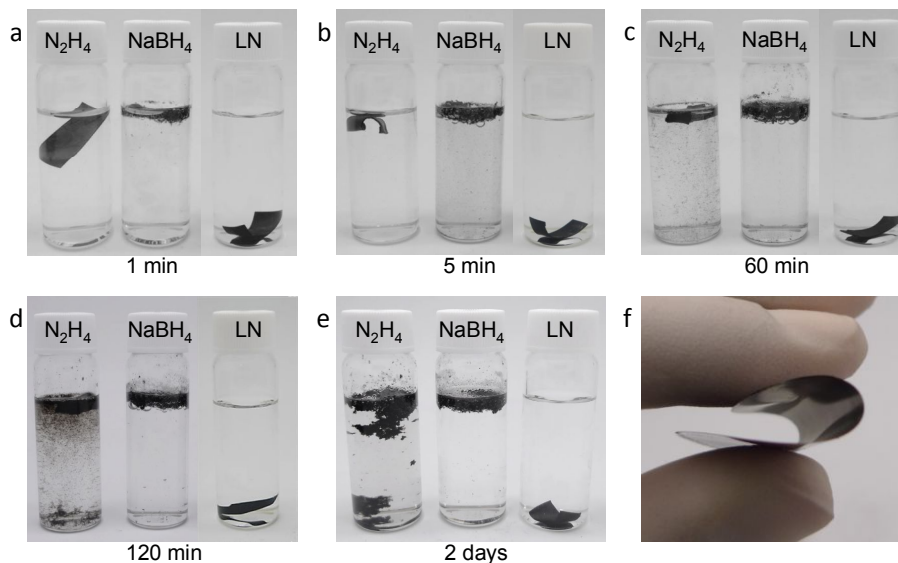


Figure 2. 7. Photographs of GO films immersed in various reducing agents (35 wt% aqueous N_2H_4 solution, 0.2 M $NaBH_4$, and LN) for various reaction times: (a) 1 min, (b) 5 min, (c) 60 min, (d) 120 min, and (e) 2 days. For clarity, the rGO film reduced by LN was re-immersed in MeOH after reduction because the LN solution is dark green. (f) A flexible rGO(LN_10min_M) film.

In the fragility testing, we immersed GO films in well-known reducing agents (hydrazine and sodium borohydride) and LN, and observed the changes in physical appearance with reduction time (Figure. 2.7). Whereas the rGO(S) and rGO(H) films start to break up within 1 and 5 min respectively, the rGO(LN_10min_M) film maintains its pristine shape for at least 2 days. Moreover, the obtained rGO(LN_10min_M) film is flexible and bendable without fracture, as shown in Figure. 2.7f. The improved mechanical stability of rGO films could be attributed to the highly retained microstructure without significant expansion in thickness during reduction with LN, as inferred from the little gas evolution in Figure 2.7.[8, 48] Considering the

difficulty of producing flexible graphene films from poorly dispersed rGO sheets, this reduction method is especially important for preparing graphene-based flexible transparent conductive films.

2.3.2. Application for TCF

2.3.2.1. Effect of oxidation control on TCF performance

For high performance TCF, large sized rGO is favorable due to their lower resistance than small sized GO from the decreased number of inter-sheet junctions. Since GO size generally determines the rGO size, GO synthesis with a large lateral size is a top priority. The lateral size of GO is affected by oxidation during the synthesis process and three different lateral sized GO were prepared by controlling the oxidation time (Figure 2.8). As the lateral size of GO increases, the sheet resistance of derived rGO decreases to 1 order. Therefore, the larger GO size should be used for high performance TCF.

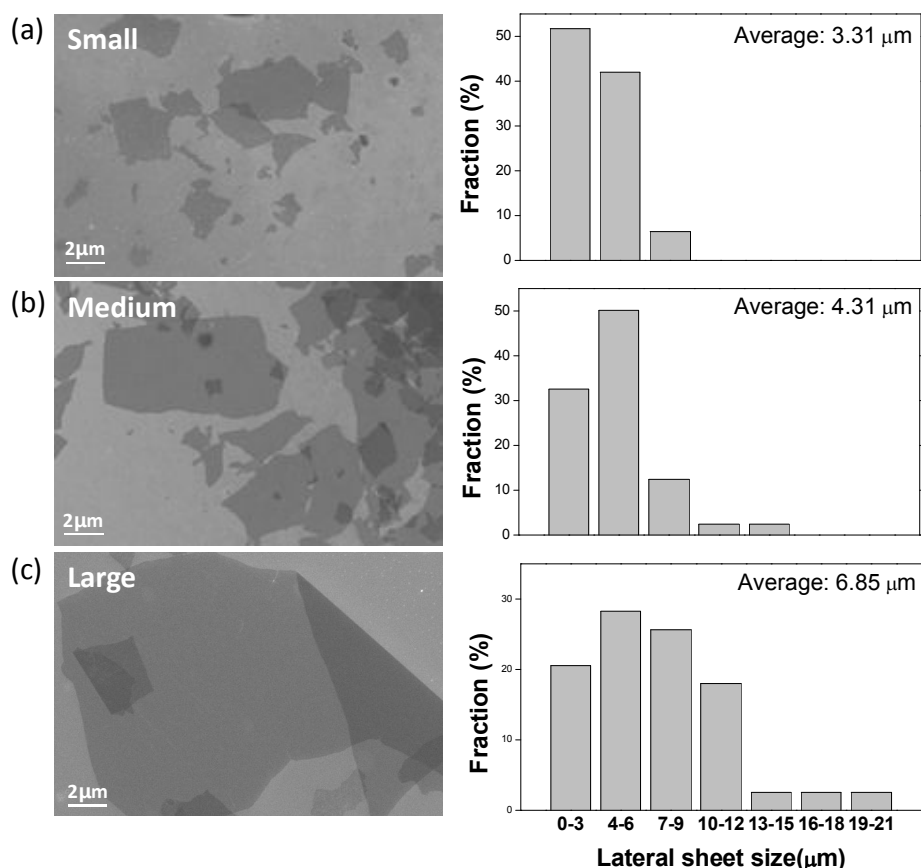


Figure 2. 8. SEM images and size distribution of (a) small sized GO, (b) medium sized GO, and (c) large sized GO.

2.3.2.2. Effect of reduction control on TCF performance

As shown earlier, reduction with LN is effective and nondestructive to film. However, neither of these properties is satisfied by other widely used reducing agents such as thermal (Th), hydrazine (N_2H_4), sodium borohydride ($NaBH_4$), and hydroiodic acid (HI). Hydrazine and sodium borohydride cannot fully reduce GO in 10 minutes at room temperature according to their color and XPS C1s spectra in Figure 2.9. In

contrast, HI shows high reducing efficiency when compared to LN, but the film is easily detached from the substrate even though the film integrity is not significantly damaged. Although thermally reducing GO at 200 °C for 10 minutes (rGO(TH)) maintains apparent integrity, good adhesion to the substrate, and high reduction efficiency, the thermal-evolved porosity inside rGO results in sheet resistance 4-5 orders higher than that of rGO(LN). Therefore, LN is the best reducing agent in preparing rGO for use in TCF applications.

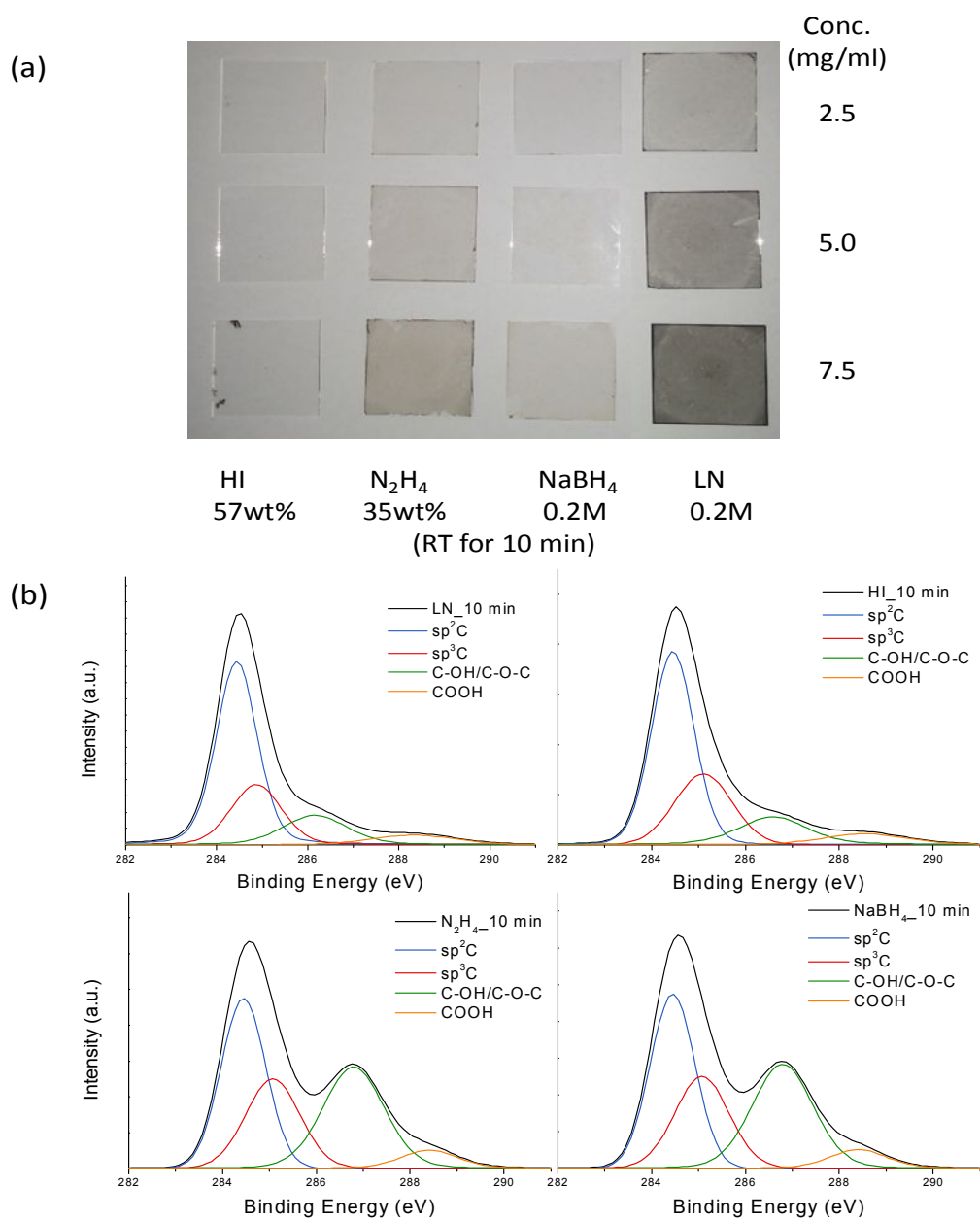


Figure 2. 9. (a) Photos of rGO TCFs prepared using different concentrations of GO and different reducing agents. (b) XPS C1s spectra of rGOs prepared by using different reducing agents.

2.3.2.3. Effect of doping on TCF performance

As shown in Figures 2.4. and 2.10, THF washed rGO, rGO(T), yields rGO that contains a sufficient number of lithium derivatives (e.g., lithium carbon compounds (LiC_x), lithium carbonate (Li_2CO_3), lithium peroxide (Li_2O_2), and lithium oxide (Li_2O)) as confirmed by XPS C1s and O1s spectra (Figure. 2.11.).

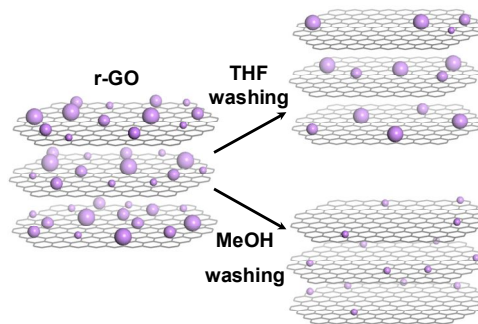


Figure 2. 10. Controlled doping of lithium-containing moieties of rGO by controlling washing step.

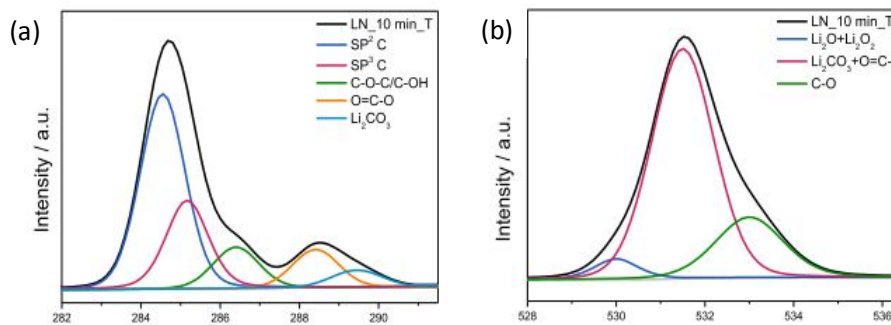


Figure 2. 11. XPS (a) C1s spectra and (b) O1s spectra of rGO(LN_10min_T).

The sheet resistance of rGO(LN_T) is lowered by 50% when compared to that of rGO(LN_M), which is attributed to the doping effect (Figure 2.12). In Raman spectra, the G band of rGO(LN_T) is blue-shifted compared to rGO(LN_M), possibly due to Fermi level shifting away from the Dirac point by a surface charge transfer,[49-52] because rGO(LN_T) has lithium containing compounds such as Li_2O_2 and Li_2CO_3 which can act as n-type dopants.[53-55] In addition, these compounds can also facilitate the charge carriers transport by the surface charge screening effect, which can seemingly increase carrier mobility.[49, 53, 54, 56-58]

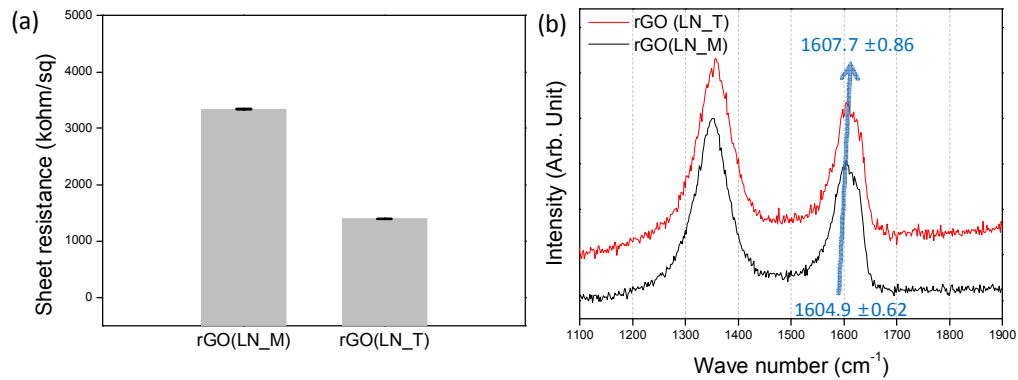


Figure 2. 12. (a) Sheet resistance and (b) Raman spectra of rGO(LN_M) and rGO(LN_T).

In Figure 2.13, the rGO prepared from large sized GO and LN reduction with controlled washing shows 20.3 and 145.8 kohm/sq with optical transparency of 66 and 91% at 550 nm wavelength, respectively, which is comparable to the TCF performance reported by others even without further treatment.[59]

The TCF performance of rGO(LN_T) is better than that of rGO(LN_M) with nitric acid doping, which is a widely used doping method. This indicates that lithium-

containing compounds have better doping effects than nitric acid. In addition, LN reduction-induced doping shows better stability than nitric acid doping, providing a solution for the poor stability of existing dopants.

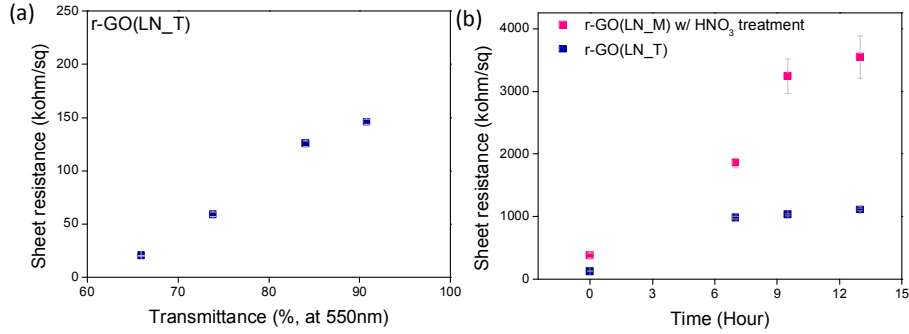


Figure 2. 13. (a) TCF performance of rGO(LN_T). (b) TCF stability of rGO(LN_M) with nitric acid doping and rGO(LN_T).

In order to evaluate the performance of different TCFs, a figure of merit (FoM), which is a ratio of direct current electrical conductivity (σ_{DC}), and optical conductivity (σ_{OP}), is considered. This FoM is derived from the relationship between optical transparency (T) and sheet resistance (Rs).[59]

$$T = \left(1 + \frac{188.5 \sigma_{OP}}{R_s \sigma_{DC}}\right)^{-2}$$

The representative FoM values of rGO prepared by different procedures are summarized in Table 2.2. rGO reduced by LN showed comparable TCF performance to rGO produced by others, even though rGO(LN_T) was not thermally annealed.

Although further research on the chemical doping effect is necessary, it should be noted that the chemical doping of rGO simultaneously occurs during reduction with

LN and simply modifying the washing step to adjust the remaining amount of lithium-containing species. Therefore, rGO TCF with better performance and stability can be obtained by LN-induced doping.

Table 2. 2. Values of σ_{DC}/σ_{OP} .

Material	σ_{DC}/σ_{OP}	References
rGO reduced by LN	0.04	Present work
rGO reduced by Hydrazine vapor with thermal annealing	0.01	[60]
rGO reduced by Hydrazine vapor with thermal annealing	0.05	[61]
rGO reduced by Hydrazine with thermal annealing	0.02	[62]
rGO thermally reduced and annealed	0.18	[63]
rGO thermally reduced and annealed	0.10	[3]

2.4. Conclusions

To design graphene for TCF applications, we used large sized GO as a precursor to synthesize large sized rGO by the shortening oxidation step. For the practical application of graphene, we have developed an ultrafast, one-step chemical reduction under ambient conditions of GO using LN as the reducing agent. Furthermore, by simply modifying the washing step, lithium-containing doping can be induced to show better TCF performance and stability than those of widely used nitric acid doping.

2.5. References

- [1] J. Zhao, S. Pei, W. Ren, L. Gao, H.-M. Cheng, *ACS Nano* **2010**, *4*, 5245.
- [2] Q. Zheng, W. H. Ip, X. Lin, N. Yousefi, K. K. Yeung, Z. Li, J.-K. Kim, *ACS Nano* **2011**, *5*, 6039.
- [3] C.-Y. Su, Y. Xu, W. Zhang, J. Zhao, X. Tang, C.-H. Tsai, L.-J. Li, *Chem. Mater.* **2009**, *21*, 5674.
- [4] A. Kasry, M. A. Kuroda, G. J. Martyna, G. S. Tulevski, A. A. Bol, *ACS Nano* **2010**, *4*, 3839.
- [5] N. Jung, N. Kim, S. Jockusch, N. J. Turro, P. Kim, L. Brus, *Nano Lett.* **2009**, *9*, 4133.
- [6] S. Stankovich, D. A. Dikin, R. D. Piner, K. A. Kohlhaas, A. Kleinhammes, Y. Jia, Y. Wu, S. T. Nguyen, R. S. Ruoff, *Carbon* **2007**, *45*, 1558.
- [7] W. Gao, L. B. Alemany, L. J. Ci, P. M. Ajayan, *Nat. Chem.* **2009**, *1*, 403.
- [8] S. Pei, J. Zhao, J. Du, W. Ren, H.-M. Cheng, *Carbon* **2010**, *48*, 4466.
- [9] G. Wang, J. Yang, J. Park, X. Gou, B. Wang, H. Liu, J. Yao, *J. Phys. Chem. C* **2008**, *112*, 8192.
- [10] Z.-J. Fan, W. Kai, J. Yan, T. Wei, L.-J. Zhi, J. Feng, Y.-m. Ren, L.-P. Song, F. Wei, *ACS Nano* **2010**, *5*, 191.
- [11] V. Dua, S. P. Surwade, S. Ammu, S. R. Agnihotra, S. Jain, K. E. Roberts, S. Park, R. S. Ruoff, S. K. Manohar, *Angew. Chem. Int. Ed.* **2010**, *49*, 2154.
- [12] A. Kumar, A. L. M. Reddy, A. Mukherjee, M. Dubey, X. Zhan, N. Singh, L. Ci, W. E. Billups, J. Nagurny, G. Mital, P. M. Ajayan, *ACS Nano* **2011**, *5*, 4345.
- [13] D. Kim, S. J. Yang, Y. S. Kim, H. Jung, C. R. Park, *Carbon* **2012**, *50*, 3229.
- [14] V. C. Tung, M. J. Allen, Y. Yang, R. B. Kaner, *Nat. Nanotechnol.* **2009**, *4*, 25.
- [15] H. A. Becerril, J. Mao, Z. Liu, R. M. Stoltenberg, Z. Bao, Y. Chen, *ACS Nano*

- 2008**, 2, 463.
- [16] D. Li, M. B. Muller, S. Gilje, R. B. Kaner, G. G. Wallace, *Nat. Nanotechnol.* **2008**, 3, 101.
- [17] S. Gilje, S. Han, M. Wang, K. L. Wang, R. B. Kaner, *Nano Lett.* **2007**, 7, 3394.
- [18] H.-J. Shin, K. K. Kim, A. Benayad, S.-M. Yoon, H. K. Park, I.-S. Jung, M. H. Jin, H.-K. Jeong, J. M. Kim, J.-Y. Choi, Y. H. Lee, *Adv. Funct. Mater.* **2009**, 19, 1987.
- [19] Y. Xu, H. Bai, G. Lu, C. Li, G. Shi, *J. Am. Chem. Soc.* **2008**, 130, 5856.
- [20] Z. Xiang, Z. Hu, D. Cao, W. Yang, J. Lu, B. Han, W. Wang, *Angew. Chem. Int. Ed.* **2011**, 50, 491.
- [21] Z. Xiang, Z. Hu, W. Yang, D. Cao, *Int. J. Hydrogen Energy* **2012**, 37, 946.
- [22] H.-J. Liu, J. Yip, K.-S. Shia, *Tetrahedron Lett.* **1997**, 38, 2253.
- [23] Y.-K. Wu, H.-J. Liu, J.-L. Zhu, *Synlett* **2008**, 621.
- [24] R. Jankowska, H.-J. Liu, G. L. Mhehe, *Chem. Commun.* **1999**, 1581.
- [25] A. Mordini, E. Ben Rayana, C. Margot, M. Schlosser, *Tetrahedron* **1990**, 46, 2401.
- [26] H.-J. Liu, X. Shang, *Tetrahedron Lett.* **1998**, 39, 367.
- [27] S. Y. Jeong, S. H. Kim, J. T. Han, H. J. Jeong, S. Yang, G.-W. Lee, *ACS Nano* **2011**, 5, 870.
- [28] X. B. Fan, W. C. Peng, Y. Li, X. Y. Li, S. L. Wang, G. L. Zhang, F. B. Zhang, *Adv. Mater.* **2008**, 20, 4490.
- [29] N. L. Holy, *Chem. Rev.* **1974**, 74, 243.
- [30] C. L. Timmons, in *Chem. Eng.*, Georgia Institute of Technology, 2004.
- [31] S. Hayano, M. Fujihira, *Bull. Chem. Soc. Jpn.* **1971**, 44, 1496.
- [32] R. J. Gritter, R. S. Woosley, P. Walker, A. J. Birch, J. Winter, K. O. Christe, A. E. Pavlath, W. Carruthers, G. Harris, I. C. MacWilliam, G. Valkanas, N. K. Roberts, H. Ulrich, A. A. R. Sayigh, A. G. Evans, B. J. Tabner, J. V. Urenovitch, R. Pejic, A.

- G. MacDiarmid, B. R. Brown, A. H. Todd, J. G. Pritchard, R. L. Vollmer, P. J. Scheuer, F. Werny, R. K. Smalley, H. Suschitzky, C. D. Foxall, J. W. W. Morgan, D. F. Evans, G. O. P. Doherty, N. B. Haynes, W. B. Whalley, H. J. Rylance, *Journal of the Chemical Society (Resumed)* **1963**, 5544.
- [33] W. H. Brown, T. Poon, *Introduction to Organic Chemistry*, John Wiley & Sons, Hoboken NJ **2005**.
- [34] M. J. Fernández-Merino, L. Guardia, J. I. Paredes, S. Villar-Rodil, P. Solís-Fernández, A. Martínez-Alonso, J. M. D. Tascón, *J. Phys. Chem. C* **2010**, *114*, 6426.
- [35] A. Ambrosi, C. K. Chua, A. Bonanni, M. Pumera, *Chem. Mater.* **2012**, *24*, 2292.
- [36] Q. Su, S. Pang, V. Alijani, C. Li, X. Feng, K. Müllen, *Adv. Mater.* **2009**, *21*, 3191.
- [37] N. Kim, S. H. Lee, *Bull. Korean Chem. Soc.* **2013**, *34*, 1141.
- [38] J. K. Song, S. Y. Han, I. Chu, J. H. Kim, S. K. Kim, S. A. Lyapustina, S. Xu, J. M. Nilles, K. H. Bowen, *The Journal of Chemical Physics* **2002**, *116*, 4477.
- [39] J. F. Garst, J. T. Barbas, F. E. Barton, *J. Am. Chem. Soc.* **1968**, *90*, 7159.
- [40] A. Esfandiari, O. Akhavan, A. Irajizad, *J. Mater. Chem.* **2011**, *21*, 10907.
- [41] C. Chen, W. Kong, H. Duan, J. Zhang, *PCCP* **2015**.
- [42] R. S. Dey, S. Hajra, R. K. Sahu, C. R. Raj, M. K. Panigrahi, *Chem. Commun.* **2012**, *48*, 1787.
- [43] L. J. Goossen, G. Deng, L. M. Levy, *Science* **2006**, *313*, 662.
- [44] I. Jung, D. A. Dikin, R. D. Piner, R. S. Ruoff, *Nano Lett.* **2008**, *8*, 4283.
- [45] M. A. Pimenta, G. Dresselhaus, M. S. Dresselhaus, L. G. Cancado, A. Jorio, R. Saito, *PCCP* **2007**, *9*, 1276.
- [46] J. O. Hwang, J. S. Park, D. S. Choi, J. Y. Kim, S. H. Lee, K. E. Lee, Y.-H. Kim, M. H. Song, S. Yoo, S. O. Kim, *ACS Nano* **2011**, *6*, 159.

- [47] J. C. Meyer, A. K. Geim, M. I. Katsnelson, K. S. Novoselov, T. J. Booth, S. Roth, *Nature* **2007**, *446*, 60.
- [48] D. Wan, C. Yang, T. Lin, Y. Tang, M. Zhou, Y. Zhong, F. Huang, J. Lin, *ACS Nano* **2012**, *6*, 9068.
- [49] J. T. Han, B. J. Kim, B. G. Kim, J. S. Kim, B. H. Jeong, S. Y. Jeong, H. J. Jeong, J. H. Cho, G.-W. Lee, *ACS Nano* **2011**, *5*, 8884.
- [50] A. C. Ferrari, J. C. Meyer, V. Scardaci, C. Casiraghi, M. Lazzeri, F. Mauri, S. Piscanec, D. Jiang, K. S. Novoselov, S. Roth, A. K. Geim, *Phys. Rev. Lett.* **2006**, *97*, 187401.
- [51] S. Pisana, M. Lazzeri, C. Casiraghi, K. S. Novoselov, A. K. Geim, A. C. Ferrari, F. Mauri, *Nat. Mater.* **2007**, *6*, 198.
- [52] J. Park, W. H. Lee, S. Huh, S. H. Sim, S. B. Kim, K. Cho, B. H. Hong, K. S. Kim, *The Journal of Physical Chemistry Letters* **2011**, *2*, 841.
- [53] J.-H. Huang, J.-H. Fang, C.-C. Liu, C.-W. Chu, *ACS Nano* **2011**, *5*, 6262.
- [54] K. C. Kwon, K. S. Choi, B. J. Kim, J.-L. Lee, S. Y. Kim, *J. Phys. Chem. C* **2012**, *116*, 26586.
- [55] Y. Zhao, C. Ban, J. Kang, S. Santhanagopalan, G.-H. Kim, S.-H. Wei, A. C. Dillon, *Appl. Phys. Lett.* **2012**, *101*, 023903.
- [56] P.-S. Wang, I.-W. Wu, C.-I. Wu, *J. Appl. Phys.* **2010**, *108*, 103714.
- [57] T. Wakimoto, Y. Fukuda, K. Nagayama, A. Yokoi, H. Nakada, M. Tsuchida, *Electron Devices, IEEE Transactions on* **1997**, *44*, 1245.
- [58] P.-C. Kao, J.-H. Lin, J.-Y. Wang, C.-H. Yang, S.-H. Chen, *J. Appl. Phys.* **2011**, *109*, 094505.
- [59] J. Du, S. Pei, L. Ma, H.-M. Cheng, *Adv. Mater.* **2014**, *26*, 1958.
- [60] G. Eda, Y.-Y. Lin, S. Miller, C.-W. Chen, W.-F. Su, M. Chhowalla, *Appl. Phys. Lett.*

2008, 92, 233305.

[61] Y. Xu, G. Long, L. Huang, Y. Huang, X. Wan, Y. Ma, Y. Chen, *Carbon* **2010**, 48, 3308.

[62] G. Eda, G. Fanchini, M. Chhowalla, *Nat Nano* **2008**, 3, 270.

[63] Z. Yin, S. Sun, T. Salim, S. Wu, X. Huang, Q. He, Y. M. Lam, H. Zhang, *ACS Nano* **2010**, 4, 5263.

Chapter 3. Edge-to-edge bridged graphene/PVDF-HFP composite through functionalization using diol and reduction

3.1. Introduction

Gas barrier film is used to prolong the lifespan of organic electronics by blocking reactive gases, moisture, and harmful agents. Although various materials such as inorganic and polymer-based composites have been proposed for the use in gas barrier films, they are prone to defects due to their poor flexibility or have intrinsically high gas permeability levels.[1, 2] In this respect, single-atomically thin graphene has been highlighted as a promising alternative due to its intrinsic flexibility, transparency, and impermeability. However, most studies of graphene-based gas barrier film have utilized graphene oxide (GO) or reduced graphene oxide (rGO) owing to its easy processability,[3-7] without in-depth investigation of its properties. Comprehensive study of GO or rGO is needed to understand how it affects the barrier film properties.

Recently, Chen *et al.* synthesized transparent layer-by-layer-assembled GO/branched poly(ethyleneimine) (BPEI) film and investigated the effect of the pH of the GO dispersion on the surface nanostructure and barrier properties. An ultra-high oxygen barrier value ($< 0.05 \text{ cm}^3\text{m}^{-2}\text{day}^{-1}$) was achieved when the pH of the GO dispersion was 3.5.[8] In addition, our group investigated the effect of the dispersibility, surface roughness, and reduction condition of GO on the degree of moisture permeation, and reported significantly increased lifetimes of organic photovoltaic devices when optimized rGO was applied as an encapsulating film.[9] Despite these efforts to design a material with optimized GO or rGO by controlling its properties, methods to prevent gas permeation through the structural design of GO based on the diffusion path have yet to be reported to the best of our knowledge. One of the most

important factors determining the diffusion path of gas is the lateral size of the GO. For this reason, use of GO with increased lateral size through bridging is necessary to increase the diffusion path and thus solve the gas permeation issue. Apart from this physical perspective on gas diffusion, the chemical effect of bridging should be taken into account because bridging is useless if the simple attack by incoming gases can break the bond. Thus, a linker, which induces bridging in a lateral direction between GO sheets and contains linkages with low reactivity to gas, is preferred.

Herein, we report the facile edge-to-edge bridging of GO sheets through an esterification reaction and a hybrid composite with a poly(vinylidene fluoride-co-hexafluoropropylene) (PVDF-HFP) matrix for use in moisture barrier film, as shown in Figure 3.1. We also investigated common linkers based on an amine (polyethyleneimine; PEI) and a metal ion (CaCl_2) for comparison. With the proposed method, bridged rGO with greatly increased lateral size was easily synthesized and readily processed for the preparation of a hybrid composite with a polymer. This hybrid composite exhibited enhanced moisture barrier performance levels, with improved impermeability by 49.6% and 36.3% compared to PVDF-HFP film and a non-bridged rGO/PVDF-HFP composite, respectively.

3.2. Materials and Methods

3.2.1. Materials and reagents

Reagent-grade chemicals were purchased from Sigma-Aldrich and were used as received.

3.2.2. Synthesis of materials

3.2.2.1. Synthesis of GO

GO was synthesized from graphite by a modified Hummer's method.⁴ In a typical experiment, graphite was initially pre-treated and added to concentrated sulfuric acid, in which $K_2S_2O_8$ and P_2O_5 had been completely dissolved. The mixture was kept at 80 °C for 72 h in an oil bath while stirring. Next, it was washed thoroughly with deionized (DI) water with vacuum filtration until the pH reached 7. The obtained pre-treated graphite was put into concentrated sulfuric acid at 0 °C, which was followed by the slow addition of $KMnO_4$ while stirring. The mixture was then stirred at 35 °C, diluted with DI water, and then stirred for 8 h at 45 °C. After H_2O_2 was added to the mixture, the mixture was washed with HCl and DI water while being centrifuged.

3.2.2.2. Synthesis of edge-to-edge bridged GO

GO (0.05 g) was dispersed in 10 mL of anhydrous dimethylformamide (DMF), followed by an addition of 4-dimethylaminopyridine (0.12 g) while stirring. After 2 h, dissolved N,N'-dicyclohexylcarbodiimide (2.06 g) in 10 mL of anhydrous DMF was added to the mixture, and this was stirred for another 2 h. Next, a diol (10 mmol) was added to the mixture and maintained for 24 h while stirring. (Note that the synthesis procedures were conducted in an argon-filled glove box to avoid exposure to moisture and air.) After washing with anhydrous DMF several times through a sequence of centrifugation and re-dispersion, edge-to-edge bridged GO was obtained. The products were designated as GO(ED), GO(HD), GO(HQ), and GO(DN) according to the abbreviated name of the diols used, i.e., 1,2-ethylenediol (ED), 1,6-hexanediol (HD), hydroquinone (HQ), and 2,6-dihydroxynaphthalene (DN), respectively.

3.2.2.3. Synthesis of bridged GO and a hybrid composite using other linkers

GO(CaCl₂) and GO(PEI) were synthesized by a reaction of CaCl₂ or polyethyleneimine (PEI), respectively, with a GO dispersion according to a method in the literature[10] with a slight modification. A GO(PEI)/PVDF-HFP composite was prepared by mixing GO(PEI) with a 15 wt% of PVDF-HFP solution.

3.2.3. Fabrication of gas barrier layer

0.15 wt% of the bridged GO dispersion in anhydrous DMF was mixed with 15 wt% of PVDF-HFP in an anhydrous DMF solution at a weight ratio of 1:2, and this was stirred for 12 h. Edge-to-edge bridged GO/PVDF-HFP film was fabricated by the doctor blade technique and was chemically reduced by hydroiodic acid at 80°C for 30 min to produce edge-to-edge bridged rGO/PVDF-HFP film.

3.2.4. Characterization.

Raman spectrometry (RAMANplus, Nanophoton) equipped with an optical microscope was used to investigate the distribution of bridged GO in the polymer matrix. The bonding characteristics of the bridged GO were studied by Fourier transform infrared spectroscopy (FTIR; Nicolet iS10, Thermo Scientific), and crystallographic analysis was conducted by powder X-ray diffraction (XRD; D8 Advance, Bruker) using Ni-filtered Cu K α radiation (λ = 0.154184 nm). The thermal properties of the products were investigated through a thermogravimetric analysis (TGA; SDT Q600, TA Instruments). Scanning electron microscopy (SEM; JSM-6700F, JEOL) and

transmission electron microscopy (TEM; JEM-2100F, JEOL) were used to verify the bridging of the GO sheets, and measurements of the water vapor transmission rate (WVTR) were taken with an WVTR analyzer (Permatran-W[®] 3/33, Mocon) at 38 °C and 100% RH.

3.3. Characteristics and application

3.3.1. Characteristics

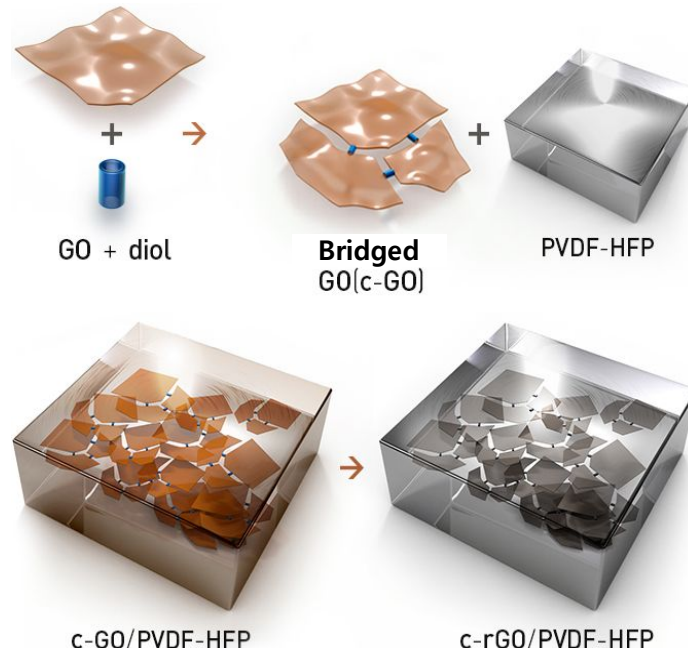


Figure 3. 1. Schematic illustration of the edge-to-edge bridged rGO (c-rGO)/PVDF-HFP synthesis process.

The process used to synthesize the edge-to-edge bridged rGO/PVDF-HFP composite is schematically illustrated in Figure 3.1. To synthesize the bridged GO, Steglich esterification in which GO sheets were bridged via a reaction between the carboxylic acid groups in GO and the alcohol groups in the diol, was utilized. The products, GO(ED), GO(HD), GO(HQ), and GO(DN) were named according to the abbreviated name of used diols, 1,2-ethylenediol, 1,6-hexanediol, hydroquinone, and 2,6-dihydroxynaphthalene, respectively. The bridged GO was then mixed with PVDF-HFP and chemically reduced to produce the edge-to-edge bridged rGO/PVDF-HFP composite.

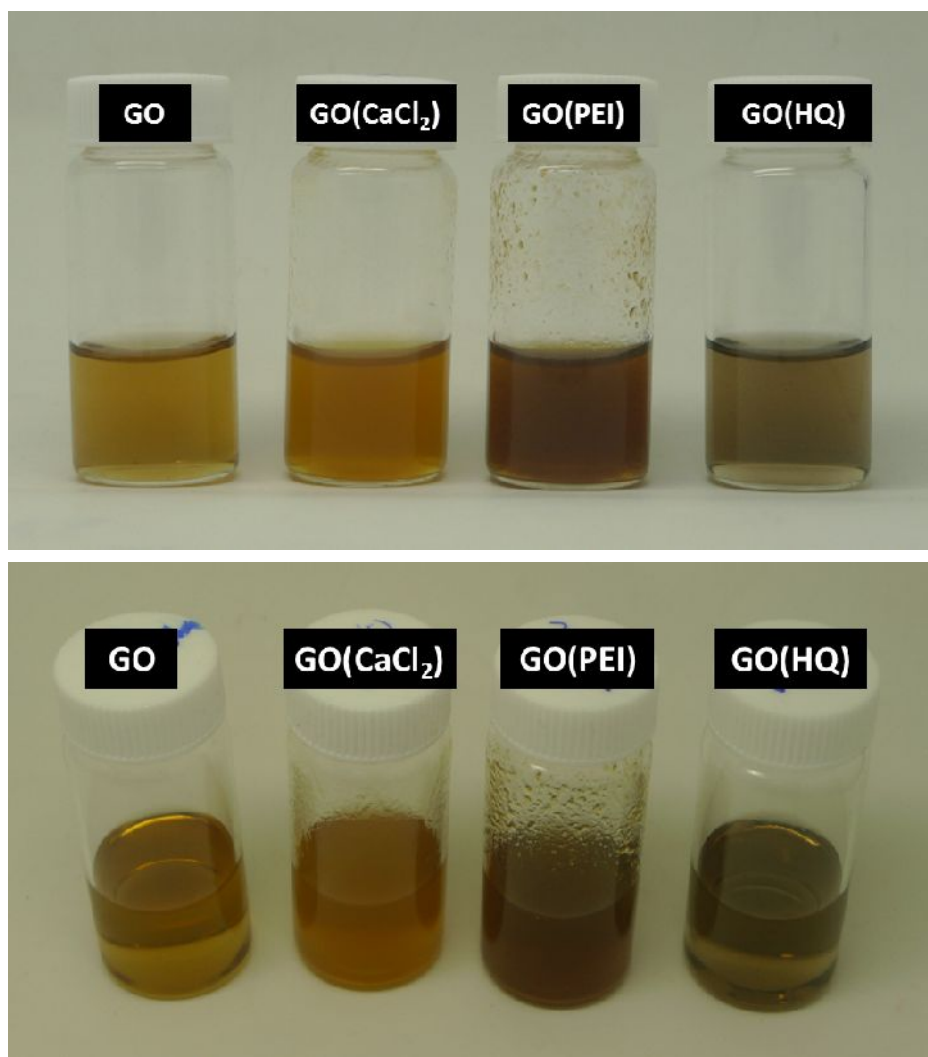


Figure 3. 2. (a) Side view and (b) Top view of GO, GO(CaCl₂), GO(PEI), and GO(HQ).

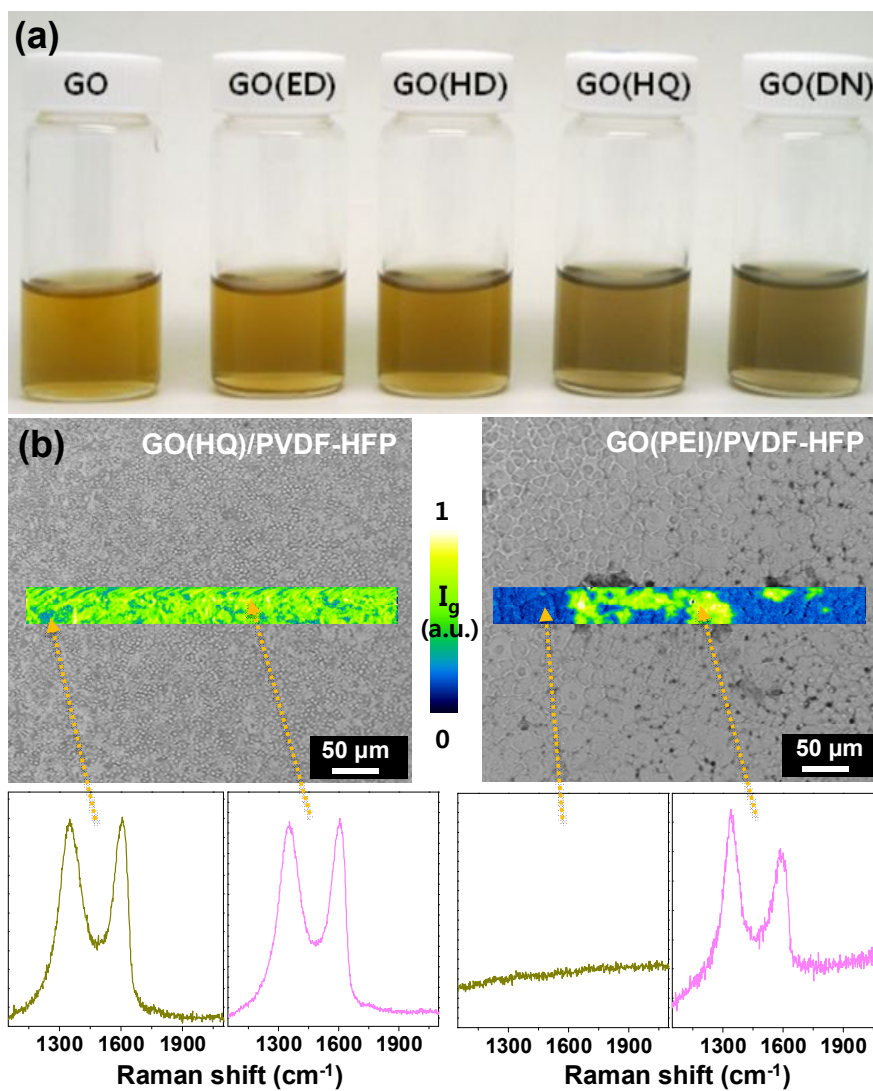


Figure 3. 3. (a) Images of the GO, GO(ED), GO(HD), GO(HQ), and GO(DN) dispersions in DMF. (b) Optical images and G-band Raman maps of the rectangular region and corresponding Raman spectra of GO(HQ)/PVDF-HFP and GO(PEI)/PVDF-HFP as indicated by the arrows.

To bridge the GO sheets, the linkages derived from the reaction between an amine (*e.g.*, polyethyleneimine[11], polyamidoamine[12], diamine[13]) or a metal ion (*e.g.*, La^{3+} , Cu^{2+})[10, 12] and a carboxylic group are generally used due to their simple process and fast reaction rate.[14, 15] However, these reactions are likely to form a gel during the formation of the linkage, which hinders further processing. Moreover, in extreme cases, aggregation occurs, as shown in Figure 3.2. In addition, linkers with acyl chloride functional groups can react with carboxylic acid groups to form an anhydride bond with fast hydrolysis kinetics. Hydrolysis is known to cause the breakage of formed bridges, resulting in the reformation of the carboxylic acid group from the backward bridging reaction. Hence, bridging without any side reactions is required, which an ester linkage can achieve because its dispersion stability is retained during bridging due to its slow reaction rate. In Figure 3.3, homogeneously well-dispersed GO and bridged GO with different diols in anhydrous dimethylformamide (DMF) are shown. It is important to note that the bridged GOs show homogeneous dispersions similar to GO dispersion. This is a great advantage of this fabrication process, as the edge-to-edge bridged GO dispersion via esterification can be directly applied to the coating process without an additional treatment. To investigate the effect of a linker on the degree of uniformity in the distribution of bridged GOs in the polymer matrix, we prepared GO(HQ)- and GO(PEI)-based hybrid films. To analyze the distribution of GO in the polymer matrix, a Raman map showing the relative G-band intensity of each resultant film was studied. A homogeneous distribution of the GO(HQ) in the polymer matrix was found, whereas the aggregation of GO(PEI) hindered the creation of a uniform dispersion in the polymer matrix (Figure 3.3b). Uniform distribution of GO(HQ) in the polymer was further supported by the Raman spectra of GO(HQ)/PVDF-HFP, which showed typical bands in GO, D- and G-bands,

regardless of the point taken. However, GO(PEI)/PVDF-HFP showed several regions in which distinct D- and G-bands were not present, indicating a poor distribution of GO. The completely different morphologies of these hybrids highlight the importance and usefulness of esterification for producing a homogeneous GO-based hybrid composite.

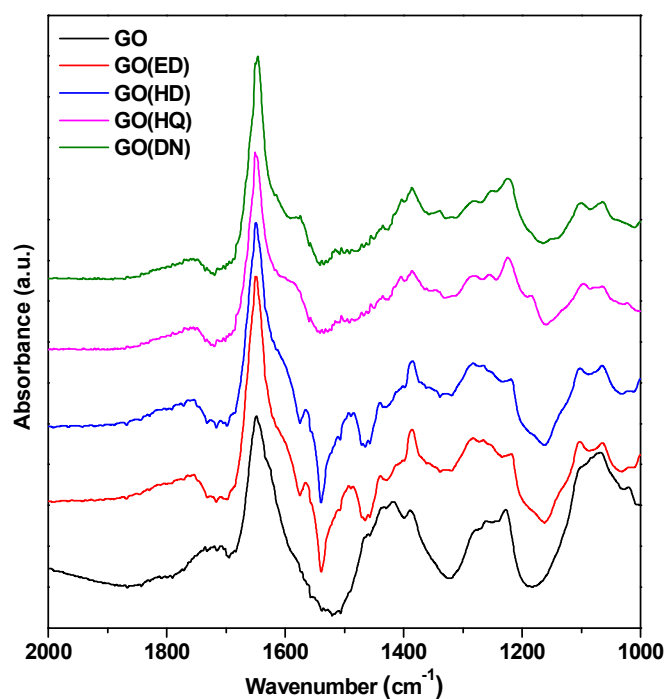


Figure 3. 4. FTIR spectra of GO, GO(ED), GO(HD), GO(HQ), and GO(DN).

The Fourier transform infrared (FTIR) spectra of GO and bridged GO were investigated to identify the bridging reaction (Figure 3.4). The FTIR spectrum of GO displayed C=O stretching vibration at 1725 cm⁻¹, C=C stretching vibration at 1650 cm⁻¹, and two vibration bands at 1420 and 1380 cm⁻¹, stemming from O-H bending and C-O

stretching, respectively. The C-C vibration at 1275 cm^{-1} , the stretching of epoxy (C-O-C) at 1230 cm^{-1} , and the bending of C-O at 1070 and 1100 cm^{-1} were also found. As the bridging reaction proceeded, most of the vibration bands remained unchanged except for C=O, aromatic C=C, and the C-H vibration bands. The C=O stretching vibration was shifted from 1725 cm^{-1} in GO to 1750 cm^{-1} in bridged GOs, indicating the vibration of the carboxylic acid group and the ester group, respectively. In addition, newly formed C-H bending vibration at 1490 cm^{-1} was found in the FTIR spectra of GO bridged with an aliphatic organic linker, and enhanced C=C stretching vibration at 1570 cm^{-1} was found in GO bridged with an aromatic organic linker. Hence, the FTIR results confirmed that the linkers were successfully introduced between the GO sheets and bridged them in an edge-to-edge manner while generating ester groups.

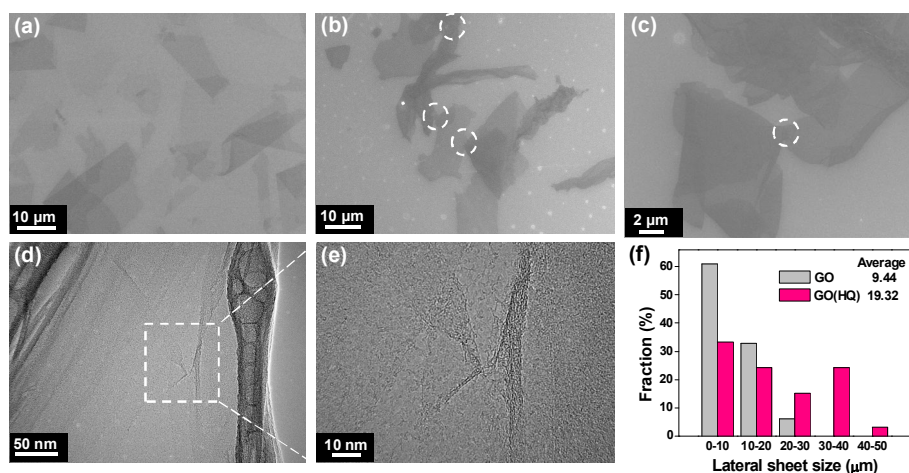


Figure 3. 5. SEM images of (a) GO and (b), (c) GO(HQ). (The white circles indicate the bridge between the GO sheets.) (d), (e) TEM images of GO(HQ). (f) The sheet size distributions of the GO and GO(HQ). The average sheet sizes of the GO and GO(HQ) are 9.44 and 19.32 μm, respectively.

A scanning electron microscopy (SEM) image of GO (Figure 3.5a) showed spatially distributed individual GO sheets with no linkage formation among the individual GO sheets. However, SEM images of GO(HQ) (Figure 3.5b and c) displayed GO sheets in close proximity to each other, clearly showing edge-to-edge bridging between the GO sheets, as indicated by the white-dotted circles. Furthermore, a closer observation with transmission electron microscopy (TEM) (Figure 3.5d and e) revealed the edge-to-edge bridging point between the GO sheets. The lateral size distributions of GO and GO(HQ) show a marked difference; 90% of the GO sheets have a lateral size of less than 20 μm , whereas half of the GO(HQ) sheets have a lateral size that exceeds 20 μm . When calculating the average lateral sheet size based on more than 10 micrographs of the samples, the average size of the GO(HQ) was nearly doubled compared to that of the GO, indicating the occurrence of edge-to-edge bridging (Figure 3.5f). X-ray diffraction (XRD) patterns of the resulting materials also support the presence of edge-to-edge bridging (Figure 3.6). After the bridging reaction, the characteristic (001) peak of GO at around 8° remained unchanged regardless of the chain length or the chemical properties of the linkers, implying that the bridging reaction was generated in an edge-to-edge rather than a face-to-face manner.

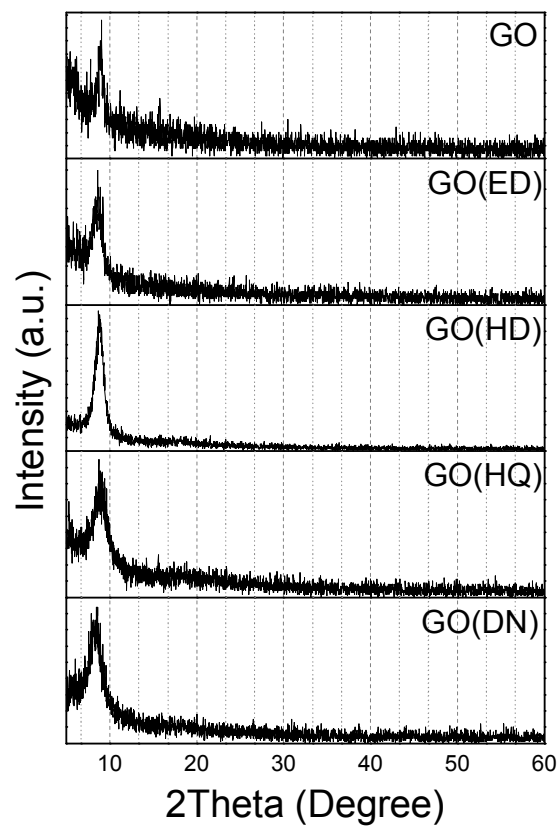


Figure 3. 6. XRD patterns of GO, GO(ED), GO(HD), GO(HQ), and GO(DN).

3.3.2. Application for gas barrier layer

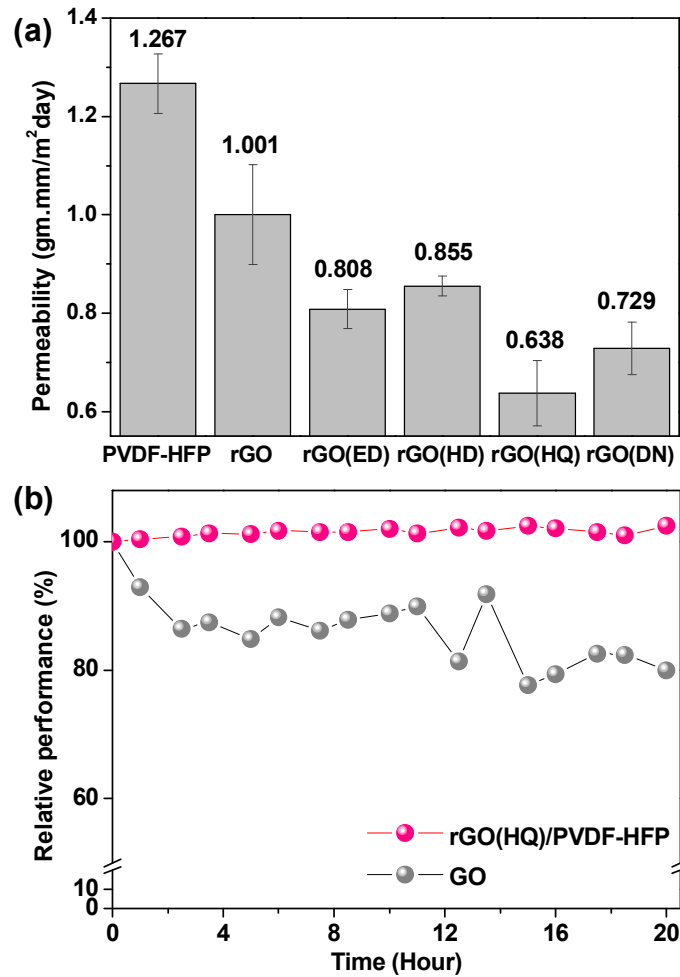


Figure 3. 7. (a) Permeability levels of PVDF-HFP, rGO/PVDF-HFP, rGO(ED)/PVDF-HFP, rGO(HD)/PVDF-HFP, rGO(HQ)/PVDF-HFP, and rGO(DN)/PVDF-HFP. Note that shortened sample names were displayed in the graph. (b) Relative water vapor shielding performances of GO and rGO(HQ)/PVDF-HFP as a function of time.

The impermeability performance of an edge-to-edge bridged graphene filler is superior to that of a graphene filler without bridging (Figure 3.7a), which highlights the effectiveness of the bridging technique to provide shielding against water vapor diffusion by means of the longer gas diffusion path stemming from the increased lateral sheet size. We also investigated the influence of the length and chemical state of the linkers used on the impermeability performance. Longer linkers (HD, DN) exhibited less enhanced performance, most likely due to the shortened water vapor diffusion path caused by the increased inter-planar gap. On the other hand, the chemical state of the linker had a more profound impact on the performance. For example, aromatic organic linkers (HQ and DN) show greatly enhanced impermeability performance compared to an aliphatic organic linker (ED and HD). This can be understood in terms of the hydrolysis of the carboxylic acid ester group. In general, a base-catalyzed reaction involving a direct nucleophilic addition of hydroxide ions to a carbonyl group is a well-known pathway through which this hydrolysis process takes place.[16] Hydrolysis overall depends primarily on the base-catalyzed reaction kinetics, which is sensitive to the electronic state and steric hindrance.[16] Delocalized electron clouds on an aromatic ring produce a less electrophilic carbon in the ester group, resulting in less of a hydrolysis reaction as compared to an aliphatic linker. In addition, the rigidity and steric hindrance of the aromatic parts can slow the hydrolysis reaction, as reported in the literature.[17, 18] When the stability of rGO(HQ)/PVDF-HFP under water vapor was investigated as a function of the exposure time (Figure 3.7b), relative water vapor shielding performance of rGO(HQ)/PVDF-HFP remained stable regardless of a prolonged exposure time, inferring a low hydrolysis rate and high stability against the moisture. In contrast, the relative water vapor shielding performance of GO was decreased by 20% within 20 h, which is possibly attributed to low friction flow of

water vapor through the capillary made by GO sheets resulting in consecutive swelling of GO.[4, 5, 19-21] From these findings, we can conclude that edge-to-edge bridged rGO(HQ) hybrid composite can be a promising moisture barrier film owing to not only increased lateral size but also aromatic chemical nature and short size of HQ linker.

3.4. Conclusions

The bridged graphene-based film was easily fabricated without the gelation phenomenon that arises during a reaction. The diol used as a linker successfully connected the graphene sheets in an edge-to-edge manner to form graphene with a large lateral size. This improved the moisture barrier performance of the rGO(HQ)/PVDF-HFP composite film by 36.3% when compared to non-bridged rGO/PVDF-HFP film.

3.5. References

- [1] A. G. Erlat, B. M. Henry, J. J. Ingram, D. B. Mountain, A. McGuigan, R. P. Howson, C. R. M. Grovenor, G. A. D. Briggs, Y. Tsukahara, *Thin Solid Films* **2001**, 388, 78.
- [2] M. Muramatsu, M. Okura, K. Kuboyama, T. Ougizawa, T. Yamamoto, Y. Nishihara, Y. Saito, K. Ito, K. Hirata, Y. Kobayashi, *Radiat. Phys. Chem.* **2003**, 68, 561.
- [3] B. M. Yoo, H. J. Shin, H. W. Yoon, H. B. Park, *J. Appl. Polym. Sci.* **2014**, 131, 39628.
- [4] Y. Su, V. G. Kravets, S. L. Wong, J. Waters, A. K. Geim, R. R. Nair, *Nat. Commun.* **2014**, 5, 4843.
- [5] R. R. Nair, H. A. Wu, P. N. Jayaram, I. V. Grigorieva, A. K. Geim, *Science* **2012**, 335, 442.
- [6] C. Xiang, P. J. Cox, A. Kukovecz, B. Genorio, D. P. Hashim, Z. Yan, Z. Peng, C.-C. Hwang, G. Ruan, E. L. G. Samuel, P. M. Sudeep, Z. Konya, R. Vajtai, P. M. Ajayan, J. M. Tour, *ACS Nano* **2013**, 7, 10380.
- [7] H. Jung, S. J. Yang, T. Kim, J. H. Kang, C. R. Park, *Carbon* **2013**, 63, 165.
- [8] J.-T. Chen, Y.-J. Fu, Q.-F. An, S.-C. Lo, S.-H. Huang, W.-S. Hung, C.-C. Hu, K.-R. Lee, J.-Y. Lai, *Nanoscale* **2013**, 5, 9081.
- [9] T. Kim, J. H. Kang, S. J. Yang, S. J. Sung, Y. S. Kim, C. R. Park, *Energy Environ. Sci.* **2014**, 7, 3403.
- [10] H. Bai, C. Li, X. Wang, G. Shi, *J. Phys. Chem. C* **2011**, 115, 5545.
- [11] H. Huang, P. Chen, X. Zhang, Y. Lu, W. Zhan, *Small* **2013**, 9, 1397.
- [12] H. Huang, S. Lu, X. Zhang, Z. Shao, *Soft Matter* **2012**, 8, 4609.
- [13] Y. S. Kim, J. H. Kang, T. Kim, Y. Jung, K. Lee, J. Y. Oh, J. Park, C. R. Park, *Chem.*

- Mater.* **2014**, *26*, 5549.
- [14] H. Hu, Z. Zhao, W. Wan, Y. Gogotsi, J. Qiu, *Adv. Mater.* **2013**, *25*, 2219.
- [15] J. Li, J. Li, H. Meng, S. Xie, B. Zhang, L. Li, H. Ma, J. Zhang, M. Yu, *J. Mater. Chem. A* **2014**, *2*, 2934.
- [16] R. A. Larson, E. J. Weber, *Reaction Mechanisms in Environmental Organic Chemistry*, CRC Press, **1994**.
- [17] Y. Tokiwa, T. Suzuki, *J. Appl. Polym. Sci.* **1981**, *26*, 441.
- [18] E. Marten, R.-J. Müller, W.-D. Deckwer, *Polym. Degrad. Stab.* **2005**, *88*, 371.
- [19] S. C. Ray, *Applications of Graphene and Graphene-Oxide based Nanomaterials*, William Andrew, 2015.
- [20] A. Lerf, A. Buchsteiner, J. Pieper, S. Schöttl, I. Dekany, T. Szabo, H. P. Boehm, *J. Phys. Chem. Solids* **2006**, *67*, 1106.
- [21] A. Buchsteiner, A. Lerf, J. Pieper, *J. Phys. Chem. B* **2006**, *110*, 22328.

Chapter 4. Pt-decorated graphene through reduction, functionalization, doping, and metal decoration

4.1. Introduction

Global concerns stemming from increased energy consumption are the limited availability of natural resources, environmental pollution, and global warming. As a solution, hydrogen has attracted attention due to its high energy density (142 MJ/kg), which is much higher than that of petroleum. It also has clean combustion, producing only water as a byproduct.[1, 2] Since storage of hydrogen is the main issue preventing the establishment of a hydrogen economy, several storage methods such as liquid hydrogen, compressed hydrogen gas, physical adsorption of hydrogen, and chemical storage of hydrogen have been suggested.[3, 4] Physical adsorption is considered a promising way to store hydrogen due to its moderate operating conditions and safety compared to others. For physical adsorption, high surface area materials including zeolite, carbons, metal-organic frameworks, intrinsically microporous polymers, and so on were researched.[2, 5-9] Among them, graphene, one of the carbon family, is considered to be a good adsorbent for hydrogen with theoretical values of up to 8 wt% due to its lightness and high surface area (ideally up to 2630 m²/g).[1, 10] In particular, graphene derived from graphene oxide (GO) followed by the reduction method has mass reducibility, structuration possibility, and ease of modification. This is beneficial for the tailoring and commercialization of graphene in hydrogen storage.

Despite the good properties of graphene as hydrogen storage medium, the experimental hydrogen storage capacity of pristine graphene is still low (generally less than 1 wt.% at room temperature and 120 bar).[1, 11, 12] This is not applicable for on-board hydrogen systems, considering the 2015 targets (5.5 wt% and 40 g/L at 300-320

K) set by the U.S. Department of Energy (DOE).[3, 7, 13] In this regard, an increase in the specific surface area (SSA) of graphene has been attempted by tailoring the interlayer spacing between GO sheets through functionalizing GO using pillaring species such as amine and boronic acid.[14-17] Despite the noticeable improvements, this approach generally works in cryogenic conditions and therefore industrially inapplicable. Another approach uses doping with heteroatoms such as boron or nitrogen to further increase the interaction between hydrogen and graphene in addition to the van der Waals interaction.[18-21] The heteroatom doping is expected to change the electronic structure of the doped graphene. Accordingly, an induced electric field can facilitate the strong hydrogen binding. Although this strategy was theoretically proved to increase hydrogen uptake, the experimental results of hydrogen storage using heteroatoms doping in graphene have not been widely reported due to the difficulty in controlling the heteroatom loading in a reliable manner.[22] Decorating with transition metals was proposed as the most promising alternative to increase the hydrogen storage capacity at ambient conditions with the spillover mechanism. Spillover refers to the migration of hydrogen atoms onto the adsorbent after hydrogen molecule dissociation on a metal catalyst such as Pt, Pd, or Ni nanoparticles.[19, 23-25]

In order to achieve a high hydrogen storage uptake based on the spillover concept, a high surface area adsorbent is undoubtedly important to provide abundant hydrogen adsorption sites. Especially for spillover, the synthesis of highly dispersed nanosized metal catalysts on the adsorbent is also considered to be essential in order to maximize the surface area of metal catalysts for the hydrogen dissociation, even though the mechanism taking place is still veiled. For this purpose, the minimization metal catalyst aggregation by heteroatoms doping or functional group introduction was theoretically suggested, and a uniform distribution of transition metal using this

technique was experimentally demonstrated in some literature.[23, 26, 27] In addition, the control of metal loading is also important. While a sufficient amount of incorporated metal can maximize the hydrogen dissociation sites, too much incorporated metal can obstruct the porosity.[28] Although the factors mentioned above should be considered, a simple and reliable way that could concurrently control the size and amount of transition metal loading with a uniform distribution whilst maximizing the porosity has not yet been reported.

In this context, we adopted polydopamine (PD) as a multi-functional substance to prepare a superb bio-inspired hydrogen storage medium. PD is synthesized through the oxidative polymerization of 3,4-dihydroxyphenethylamine (dopamine), which is inspired by 3,4-dihydroxyphenylalanine (Dopa) in marine mussels. Since Dopa has been considered to play a key role in the strong adhesion to various species due to catechol and amine functional groups, PD was used as a strong metal binder to uniformly distribute nanosized catalytic Pt particles.[29, 30] As a result, the size and amount of decorated Pt nanoparticles were systematically controlled by modulating the functionalization degree of PD. In addition, PD utilized as a reducing agent and functionalizer helped to prepare three-dimensional, interconnected porous graphene foams with tailored porosity. By controlling the porosity and decoration of Pt nanoparticles, the resultant Pt-decorated graphene (rGO/PD_Pt) showed highly enhanced hydrogen storage capacity (2.93 wt%) under a practical operating condition of 298 K at 100 bar with an enhancement factor of 551% based on rGO, which highlights the potential of an early hydrogen economy realization.

4.2. Tailor-fitted preparation of Pt-decorated graphene for hydrogen storage

4.2.1. Material and reagents

Graphite was purchased from Bay Carbon while 0.1M NaOH was purchased from Daejung Chemicals and Metals Co., Ltd. All other chemicals were purchased from Sigma-Aldrich. GO was produced by a modified Hummers' method with slight changes.

4.2.2. Synthesis of Materials

4.2.2.1. Synthesis of PD

Dopamine hydrochloride was dissolved in deionized (DI) water while stirring. 100mM of Tris buffer was added to adjust the pH of the solution. The solution was then hydrothermally treated at 250°C in a tightly sealed Teflon liner inside an autoclave. After reacting, PD was washed, collected, and freeze-dried.

4.2.2.2. Synthesis of PD_Pt.

Freeze-dried PD was dispersed in ethylene glycol for 1 hour using a bath sonication. Two fold of chloroplatinic acid hydrate was put in PD dispersion and the pH was then adjusted to 8 using 0.1 M NaOH. The dispersion was sonicated for another hour before being kept at 110 °C for 2 hours while stirring, refluxing, and purging with nitrogen. After cooling down to near room temperature, the product was washed, collected, and dried at 60 °C in a vacuum oven.

4.2.2.3. Synthesis of rGO

GO (125mg) was dispersed in DI water (50ml) for 1 hour using a bath sonication. After adding 100mM of Tris buffer to adjust the pH of the dispersion, it was hydrothermally treated at 250°C then tightly sealed inside a Teflon liner and autoclaved. After a desired time, PD was washed, collected, and freeze-dried.

4.2.2.4. Synthesis of rGO_Pt

Freeze-dried rGO was dispersed in ethylene glycol for 1 hour using a bath sonication. Two fold of chloroplatinic acid hydrate was put in rGO dispersion and the pH was then adjusted to 8 using 0.1 M NaOH. The dispersion was sonicated for another hour before being kept at 110 °C for 2 hours while stirring, refluxing, and purging with nitrogen. After cooling down to near room temperature, the product was washed, collected, and dried at 60 °C in a vacuum oven.

4.2.2.5. Synthesis of rGO/PDxx

GO (125mg) was dispersed in DI water (50ml) for 1 hour using a bath sonication. The GO dispersion was mixed with the dopamine solution. After the pH of the mixture was adjusted using Tris buffer, it was hydrothermally treated at 250°C for some time. The mixture was cooled to room temperature, washed, collected, and freeze-dried. The products were named rGO/PDxx, where xx refers to the hydrothermal treatment time in hours.

4.2.2.6. Synthesis of rGO/PDxx_Pt

Freeze-dried rGO/PDxx was dispersed in ethylene glycol for 1 hour using a bath

sonication. Two fold of chloroplatinic acid hydrate was put in rGO/PDxx dispersion and the pH was then adjusted to 8 using 0.1 M NaOH. The dispersion was sonicated for another hour before being kept at 110 °C for 2 hours while stirring, refluxing, and purging with nitrogen. After cooling down to near room temperature, the product was washed, collected, and dried at 60 °C in a vacuum oven.

4.2.3. Characterization

A microstructure analysis was conducted using scanning electron microscopy (SEM; MERLIN Compact, ZEISS) and analytic transmission electron microscopy (Analytic TEM; Tecnai F20, FEI and JEM-2100F, JEOL Ltd.). A UV-Vis spectrometer (Cary 5000, Varian Inc.) was used to identify the presence of dopamine and intermediate species. The N and Pt content and the surface characteristics were analyzed by elemental analysis (Flash EA 1112, Thermo Electron corporation) and X-ray photoelectron spectroscopy (XPS; AXIS-His, KRATOS). A Fourier transform infrared spectrophotometer (FTIR; Nicolet iS10, Thermo Scientific) was used to investigate bonding characteristics. For crystal structure analysis, powder X-ray diffraction (PXRD; D8 Advance, Bruker) using Cu K α radiation ($\lambda = 0.154184$ nm) was used. Nitrogen and hydrogen sorption measurements were carried out with a static volumetric gas adsorption instrument (ASAP 2020, Micromeritics) at 77 K and magnetic suspension microbalance (Isosorp 2000, Rubotherm) at 298K. Ultrahigh purity grade gases (99.999-99.9999%) of He, N₂, and H₂ were used in all sorption measurements. The instrument was periodically checked using Silica-alumina, multi-walled carbon nanotube, and metal organic framework-derived carbon as common references.

4.3. Characteristics and application

4.3.1. Characteristics

PD is presumed to be formed as a result of dopamine oxidation, since the exact mechanism has not yet been elucidated. A commonly proposed dopamine oxidation and cyclization pathway to make PD goes through the successive production of intermediate species: dopamine-o-quinone (DQ), Aminochrome (AC), 5,6-Dihydroxyindole (DHI), and PD.[31, 32] The PD formation is identified by XPS N 1s spectrum of rGO/PD as shown in Figure 4. 1. While dopamine only has primary amine functional groups, the nitrogen in rGO/PD is mainly in its pyrrolic nitrogen form as a result of an oxidative polymerization of dopamine with cyclization.[31, 32] Further, because intermediate species show distinguished colors, we can find their presence using UV-Vis absorption spectroscopy. In Figure 4. 2a, a rGO/PD filtrate during purification shows no absorption peak at 280 nm corresponding to dopamine, indicating that all dopamine underwent oxidation. Instead, two distinguishable peaks at 344 and 460 nm are found, which are representative peak of DQ and AC, respectively. As the reaction time increases, the absorbance intensity of the peaks decreases, meaning that less intermediate species were found. In turn, more PD was formed onto graphene. This is also supported by the change in microstructure from SEM images and nitrogen content deduced from the elemental analysis (Figure 4. 3). As the reaction time increases, the surface of graphene is covered with more PD and the nitrogen content of rGO/PD increases. XPS C 1s spectra of samples show a similar trend (Figure 4. 4 and Table 4. 1). The relative ratio of C-O/C-N increases as the reaction time increases in rGO/PDs while the relative ratio of C-O decreases from 38.42% in GO to 17.05% in rGO, meaning that more PD is introduced onto graphene when increasing the reaction time.

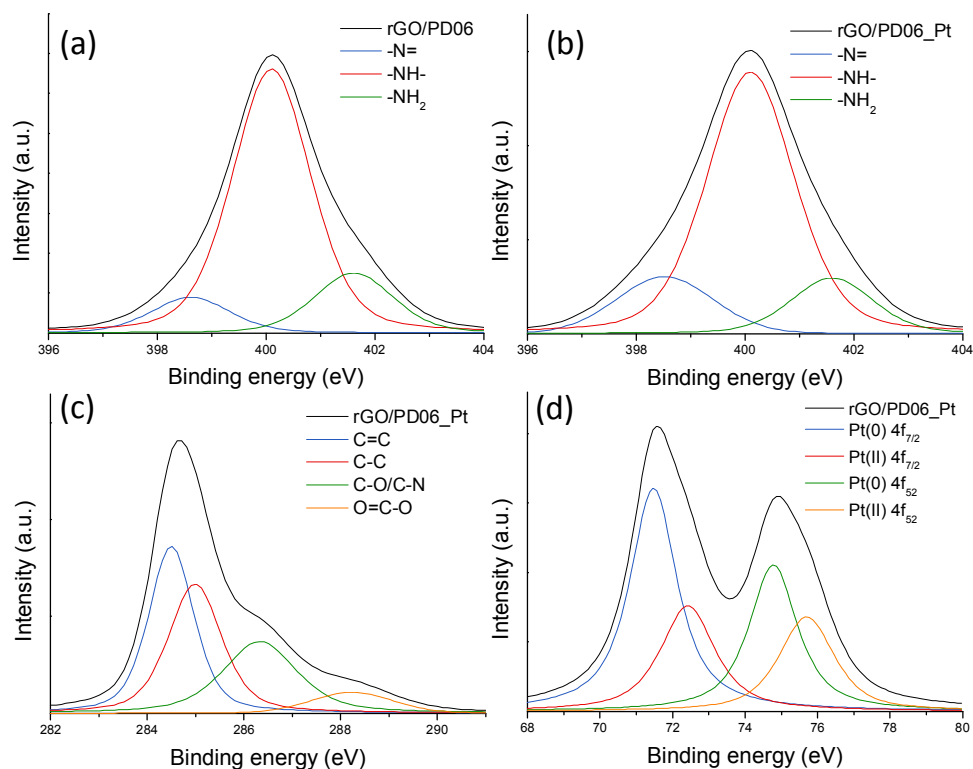


Figure 4. 1. XPS N 1s spectra of (a) rGO/PD06 and (b) rGO/PD06_Pt. XPS (c) C 1s and (d) Pt 4f spectrum of rGO/PD06_Pt.

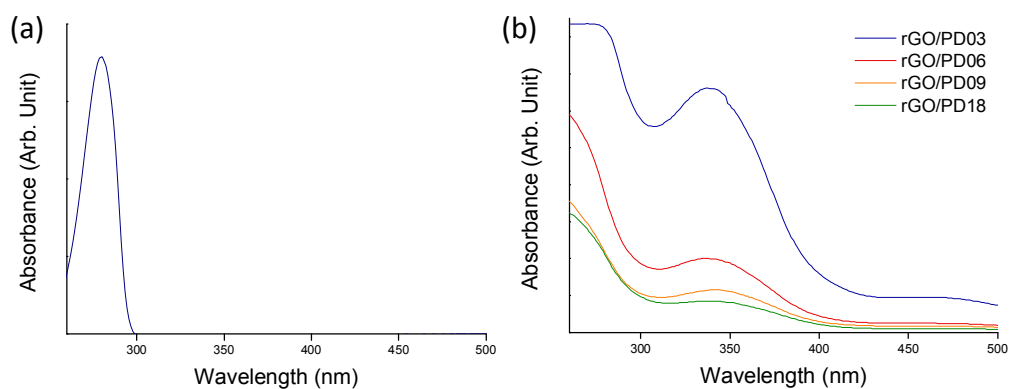


Figure 4. 2. UV-Vis absorption spectra of (a) dopamine and (b) rGO/PDs with different reaction times.

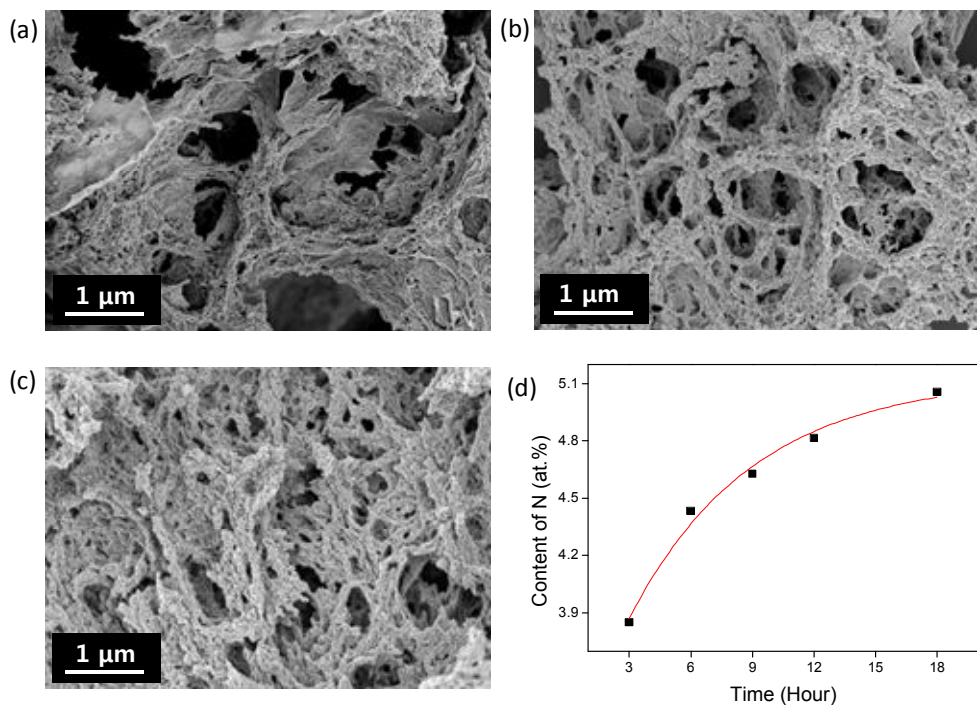


Figure 4. 3. SEM images of (a) rGO/PD03, (b) rGO/PD06, and (c) rGO/PD12. (d) Nitrogen content as a function of reaction time.

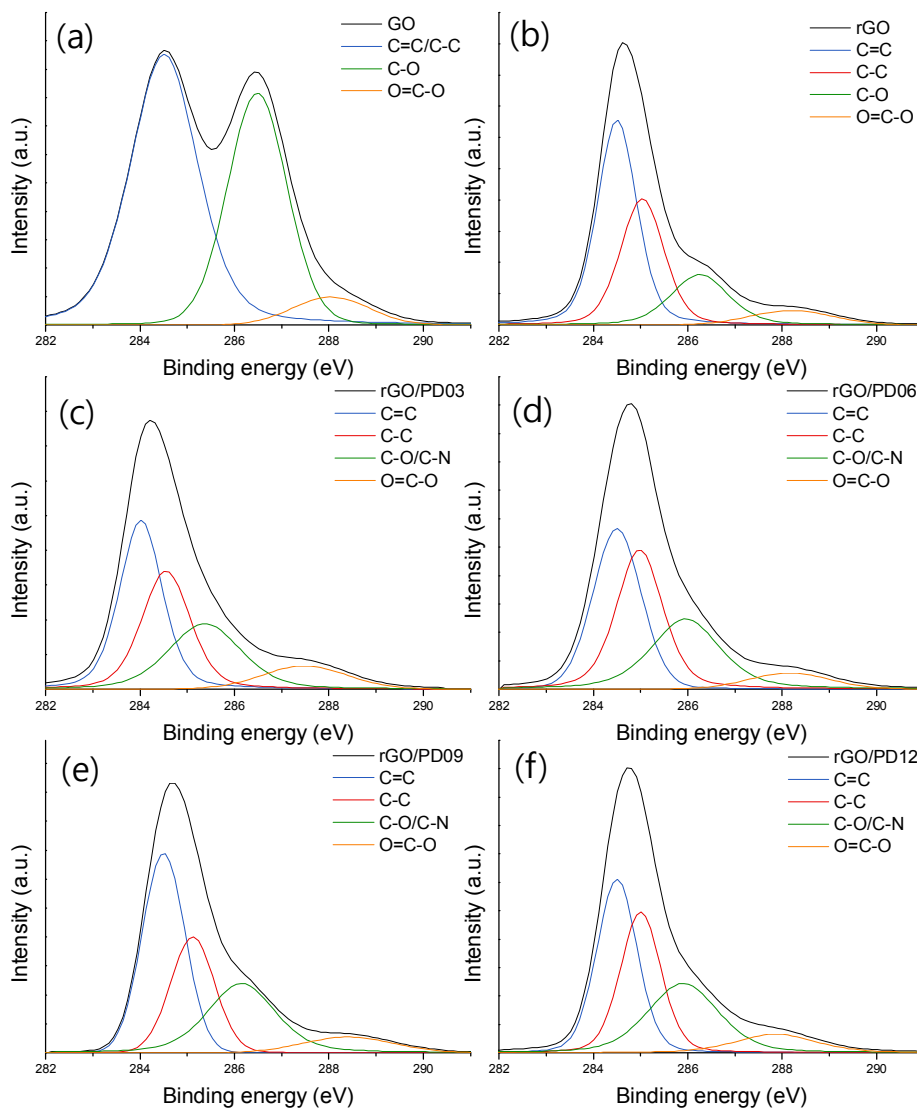


Figure 4. 4. XPS C 1s spectra of (a) GO, (b) rGO, (c)-(f) rGO/PDs.

Table 4. 1. Quantitative analysis of XPS C 1s data.

Sample	C=C (%)	C-C (%)	C-O/C-N (%)	O=C-O (%)
GO	55.88		38.42	5.71
rGO	46.11	30.80	17.05	6.04
rGO/PD03	37.04	29.32	24.40	9.24
rGO/PD06	35.52	32.91	25.55	6.02
rGO/PD09	41.30	25.36	26.37	6.97
rGO/PD12	35.51	29.51	26.64	8.33
rGO/PD18	36.32	30.90	27.49	5.29

Dopamine reduces GO through oxidative polymerization to become PD. In addition, PD has a number of benzene rings as well as amine and hydroxyl functional groups that possibly interact with GO via noncovalent interactions such as π - π interaction and hydrogen bonding. In Figure 4. 5, the FTIR spectra of rGO and rGO/PD are shown. Peaks at 3371, 1726, 1630, and 1063 cm^{-1} were found in the FTIR spectrum of GO, indicating the presence of O-H, carboxyl C=O, C=C, and C-O, respectively. After reacting GO with dopamine, the carboxyl C=O peak was almost entirely eliminated by GO reduction. However, a broad peak at 3371 cm^{-1} remains, which is attributed to the stretching vibration of hydrogen bonded O-H. Furthermore, new peaks at 1568 and 1170 cm^{-1} are apparent, stemming from the aromatic C=C and C-N stretching vibrations, respectively. These support a successful introduction of

catechol and amine functional groups through PD functionalization onto graphene. The formation of amide functional groups is not observed, meaning that a covalent functionalization between PD and GO does not happen.

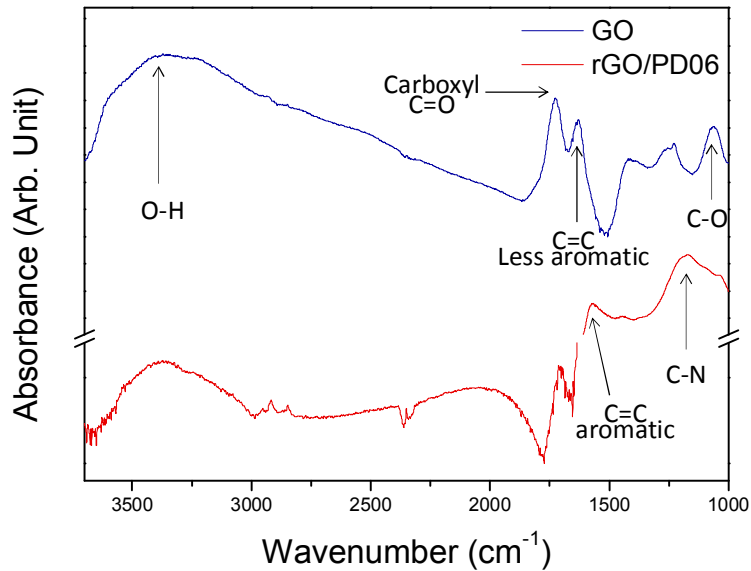


Figure 4. 5. FTIR spectra of GO and rGO/PD06

As a result of functionalization, rGO/PD with three-dimensionally connected porous structures was synthesized as shown in Figure 4. 6 and Figure 4. 7. Graphene sheets become highly interconnected with small sized pores through PD functionalization as the reaction time increases. Nitrogen adsorption isotherms of rGO/PDs also support the continuing pore development by increasing the reaction time, resulting in an increased Brunauer–Emmett–Teller (BET) SSA. rGO/PDs commonly exhibits type-IV isotherm; as defined by IUPAC (International Union of Pure and

Applied Chemistry), a slight increase in the low relative pressure region means an existence of negligible amount of micropores and a hysteresis loop indicates the presence of mesopores in rGO/PD. From the morphology and pore characteristics analyses, rGO/PD foams with meso-/macro-pores which are enough size for introducing Pt nanoparticles were found. It is noteworthy that BET SSA, which is a critical factor for hydrogen storage, is tunable simply by controlling the amount of functionalized PD.



Figure 4. 6. Photograph of rGO/PD foam.

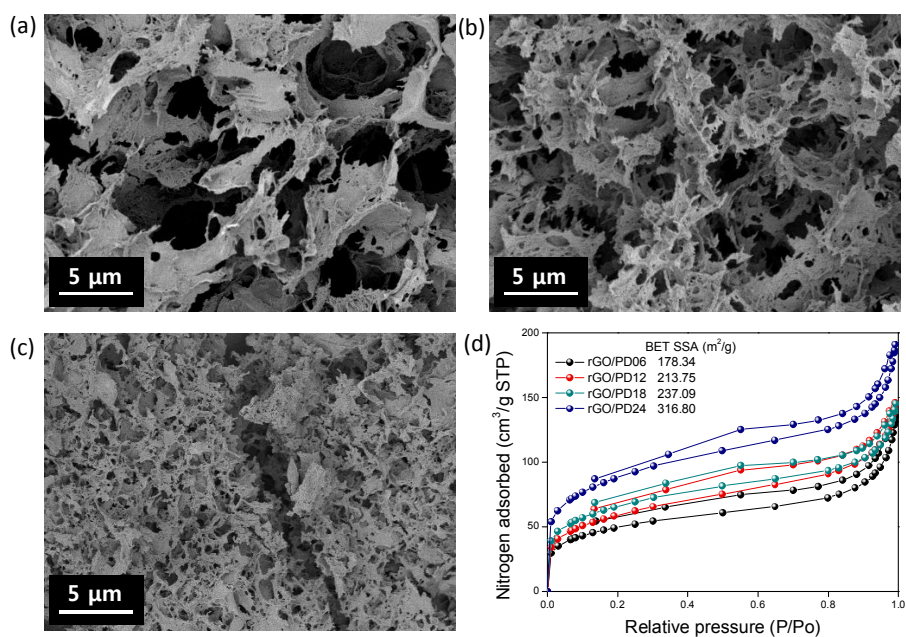


Figure 4. 7. SEM images of (a) rGO/PD03, (b) rGO/PD06, and (c) rGO/PD12. (d) Nitrogen adsorption isotherms and BET SSA of rGO/PDs with different reaction times.

A uniform metal distribution without aggregation is important for a good hydrogen storage medium using the spillover mechanism. Based on the previous literature, introducing functional groups and doping heteroatom is effective approaches.[26, 27] PD is a good candidate, because it has both hydroxyl and amine functional groups as mentioned previously. In Figure 4. 8, PD_Pt shows a uniform distribution of Pt on PD without aggregation, whereas rGO_Pt shows a heterogeneous distribution of Pt nanoparticles at various sizes and aggregated parts, proving the effectiveness of PD in binding Pt nanoparticles. More evidence of PD effectively binding Pt nanoparticles can be provided from the oxidation state of Pt in the XPS Pt 4f spectrum (Figure 4. 1). When Pt (+4 oxidation number in the starting precursor H_2PtCl_6) is introduced into PD-functionalized rGO through ethylene glycol reduction, Pt with 0 and +2 oxidation

states are found in rGO/PD_Pt. The presence of Pt(II) indicates the interaction of Pt(0) with nitrogen or oxygen in PD as similarly suggested by others.[18, 19, 33]

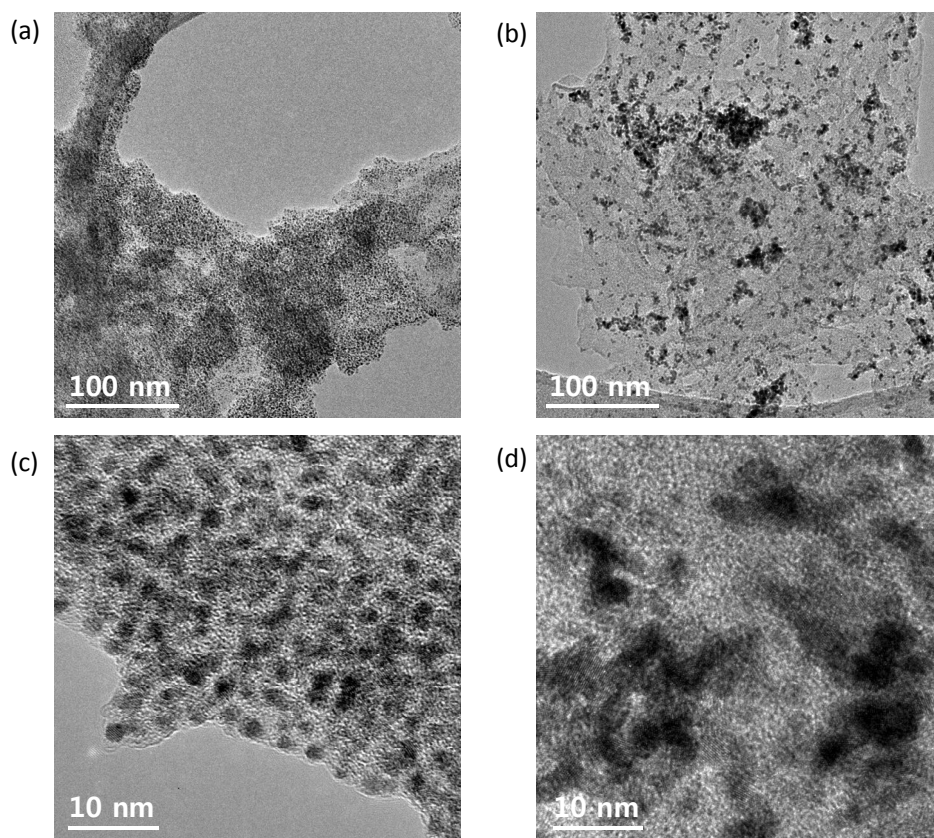


Figure 4. 8. TEM images of (a), (c) PD_Pt and (b), (d) rGO_Pt.

In addition to a uniform distribution of Pt nanoparticles, tailoring the size and amount of decorated Pt nanoparticles are also necessary. These are tuned by controlling the degree of functionalized PD on graphene. In Figure 4. 9, the distribution of Pt nanoparticles in rGO_Pt and rGO/PD_Pt with different PD functionalization is displayed. Regardless of the reaction, face-centered cubic crystal structures of Pt nanoparticles were decorated as inferred from the d-spacing in Figure 4. 9f.[34-36]

When no PD was used, rGO_Pt exhibits two distinct regions: one covered with almost no Pt nanoparticles and the other decorated with big, irregularly shaped Pt clusters as shown in Figure 4. 8b and Figure 4. 9a. Although rGO/PD03_Pt reflects a better distribution than rGO_Pt due to a slightly functionalized PD, usually large and uneven Pt nanoparticles were found, indicating an insufficient PD coverage. A uniform distribution of small sized Pt particles (2.21 ± 0.08 nm) was found in rGO/PD06_Pt, meaning that the functionalization of PD in this sample is considered to be sufficiently strong to bind Pt nanoparticles without aggregation. The rGO/PD_Pts with reaction times longer than 6 hours still show regular Pt nanoparticle shapes with a narrow size distribution, but Pt nanoparticles are densely positioned. This indicates that more Pt nanoparticles were decorated on rGO/PD, which is attributed to a higher degree of PD functionalization. This further means that there is over-coverage of Pt nanoparticles on the rGO/PD surface, leading to the cohesion of closely located Pt nanoparticles and resulting in slight aggregation. We conclude that the degree of PD functionalization affects the size, distribution, and content of Pt as shown in Figure 4. 10. In other words, a uniform distribution of Pt with optimized size and loading can be achieved by controlling the degree of PD functionalization.

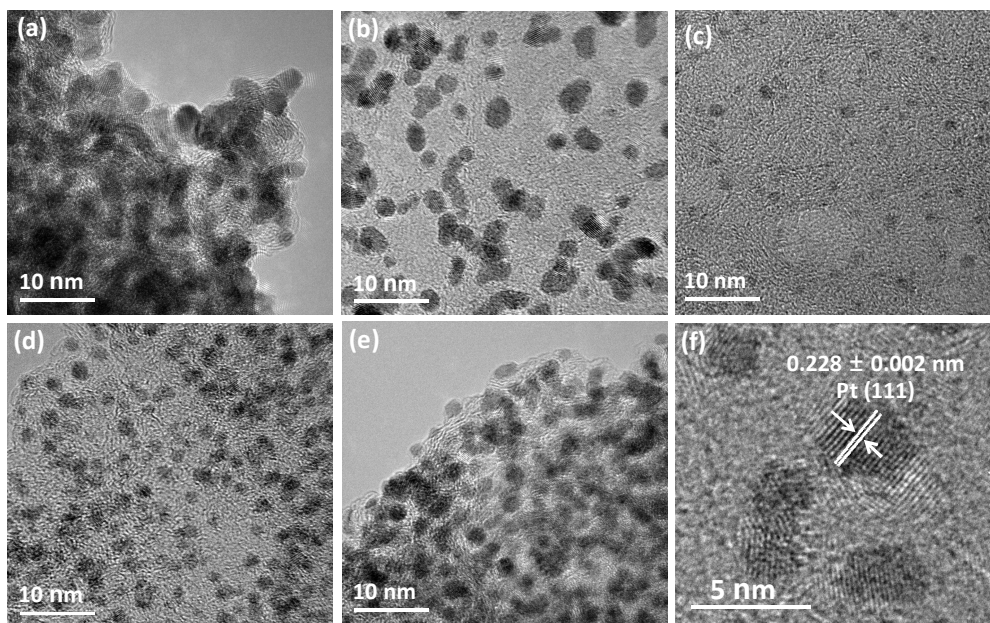


Figure 4. 9. TEM images of (a) rGO_Pt, (b) rGO/PD03_Pt, (c) rGO/PD06_Pt, (d) rGO/PD09_Pt, (e) rGO/PD12_Pt. (f) Magnified image of rGO/PD_Pt.

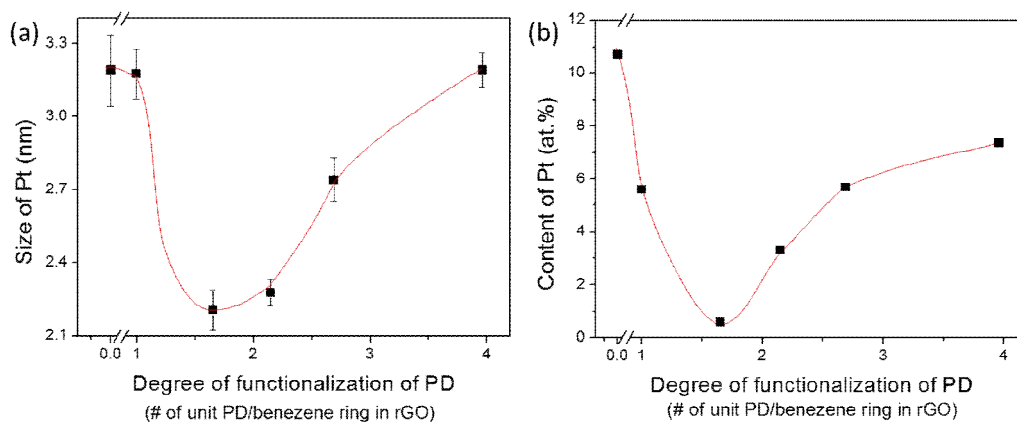


Figure 4. 10. Correlation between (a) size of Pt and (b) content of Pt and degree of functionalization of PD.

In Figure 4. 11, XRD patterns of rGO/PD and rGO/PD_Pts are displayed. rGO/PD shows a small and broad peak at $2\theta = 24.7^\circ$, which corresponds to the (002) plane diffraction of graphene. After Pt nanoparticle decoration, three peaks appear at 39.9° , 44.3° , and 67.5° , which correspond to (111), (200), and (220) diffraction planes of Pt, respectively, in rGO/PD03_Pt and rGO/PD09_Pt. This indicates the incorporation of a relatively large amount of Pt into rGO/PD (Table 4. 2). In contrast, rGO/PD06_Pt shows a weak Pt diffraction peak, indicating the presence of uniformly distributed Pt (0.57 at.%) in small amounts with small size, which is more favorable for metal-assisted hydrogen storage.[37]

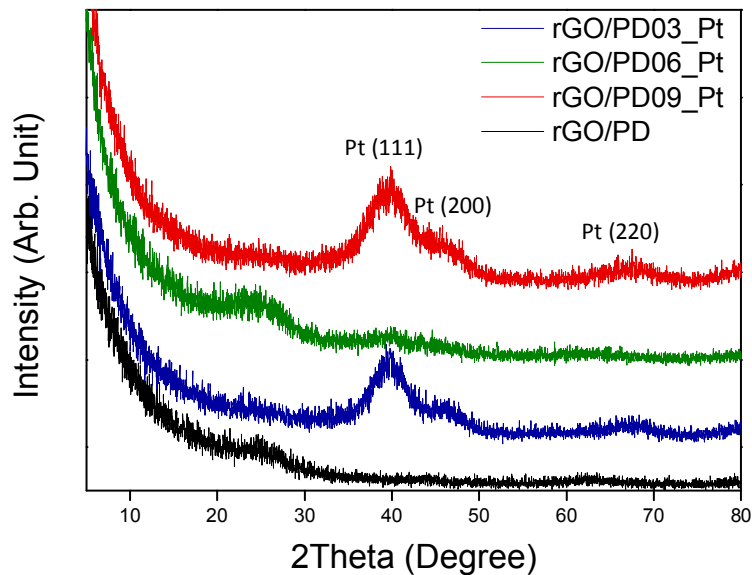


Figure 4. 11. XRD patterns of rGO/PD, rGO/PD03_Pt, rGO/PD06_Pt, and rGO/PD09_Pt.

Table 4. 2. Summary of BET SSA, Pt size and content, and hydrogen uptake of samples

Sample	BET SSA (m ² /g)	Size of Pt (nm)	Pt content		Hydrogen uptake at 298 K, 10 bar (wt.%)
			(at.%)	(wt.%)	
rGO	419.66	3.19	0	0	0.13
rGO/PD06	178.34	-	0	0	0.30
rGO/PD03_Pt	228.97	3.17	5.58	47.44	0.40
rGO/PD06_Pt	303.00	2.21	0.57	8.11	0.64
rGO/PD09_Pt	350.56	2.28	3.29	34.29	0.57
rGO/PD12_Pt	161.35	2.74	5.67	47.76	0.35
rGO/PD18_Pt	177.18	3.19	7.36	54.39	0.22

The size and amount of decorated Pt nanoparticles also influence the pore characteristics of rGO/PD_Pt. The nitrogen adsorption isotherms of all samples exhibit Type IV, indicating a mesopores-dominated pore structure (Figure 4. 12a). A high loading of Pt nanoparticles results in the significant decrease of BET SSA, as shown in nitrogen adsorption isotherms of rGO/PD03_Pt, rGO/PD12_Pt, and rGO/PD18_Pt. This is due to an obstruction in the pores by a large amount of big sized Pt particles. In contrast, a small amount of small sized Pt particles could partially block the meso-/macropores that make smaller pores, resulting in an increased BET SSA as with rGO/PD06_Pt (303.00 m²/g). This is further supported by the pore size distribution change shown in Figure 4. 13.

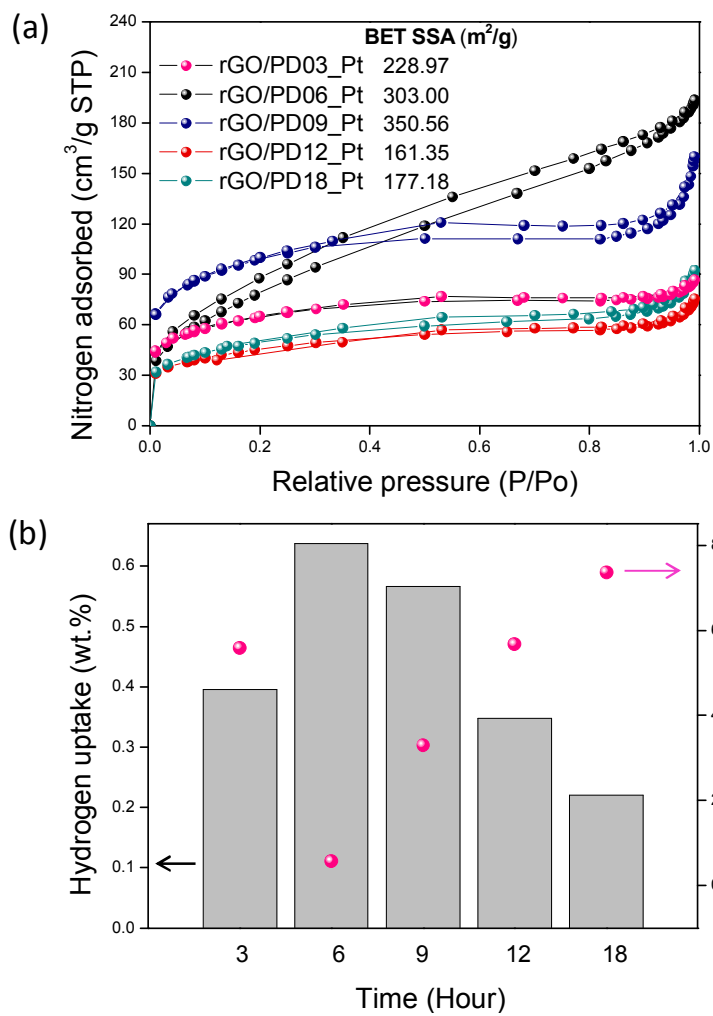


Figure 4. 12. (a) Nitrogen adsorption isotherms of rGO/PD_Pt and (b) hydrogen uptake at 298 K and 10 bar with Pt content of rGO/PD_Pts.

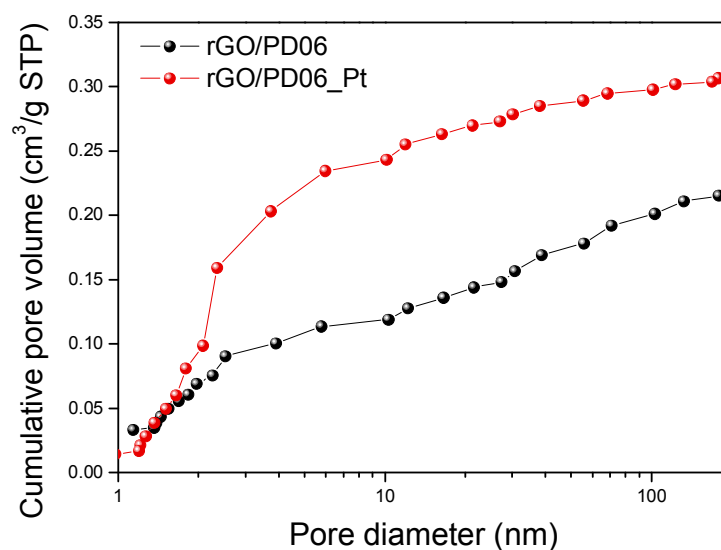


Figure 4. 13. Pore size distribution of rGO/PD_06 and rGO/PD06_Pt by cumulative pore volume using Barrett-Joyner-Halenda (BJH) model.

The hydrogen storage capacity results of rGO/PD_Pts at different reaction time are provided in Figure 4. 12b. Since the hydrogen uptake decreases as the content of Pt increases, the hydrogen storage capacity of rGO/PD_Pt is predominantly dependent on the Pt content, indicating that a proper amount of Pt nanoparticles decoration is important. The rGO/PD06_Pt which has a uniformly decorated Pt nanoparticles at small loading, results in a highest hydrogen uptake of 0.64 wt.% at 298 K and 10 bar. In rGO/PD09_Pt, a slightly lower hydrogen storage capacity (0.57 wt.%) was found even though it has a higher BET SSA than rGO/PD06_Pt, which is attributed to a higher Pt content of 3.29 at.%. This trend also applies to rGO/PD_Pt with a higher Pt content because of the heaviness of Pt as inferred by the content of Pt in wt.% in Table 4. 2.

4.3.2. Application for hydrogen storage

As the best hydrogen storage material among rGO/PD_Pts, the hydrogen sorption of rGO/PD06_Pt is compared with those of rGO and rGO/PD06 to investigate the effect of functionalization of PD and decoration with Pt nanoparticles on hydrogen storage (Figure 4. 14). rGO/PD06 shows a higher hydrogen storage capacity of 0.85 wt.% at 298 K and 100 bar than rGO (0.45 wt.%) with an 189% increase due to the nitrogen doping effect. Pyrrolic nitrogen (-N-) and pyridinic nitrogen (-N=) can donate π -electrons to graphene, which changes the local electronic density near the nitrogen, and results in a stronger affinity to hydrogen than pristine graphene.[19] The enhancement in hydrogen uptake by Pt nanoparticles decoration, however, surpasses the nitrogen doping effect because rGO/PD06_Pt showed a much higher hydrogen uptake of 2.93 wt.% which shows a significant enhancement factor of 551 and 245 % compared to rGO and rGO/PD06, respectively. The outstanding hydrogen storage capacity of rGO/PD06_Pt is mainly attributed to spillover, even though the mechanism is still under investigation. To the best of our knowledge, this is the best hydrogen storage capacity per unit BET SSA using graphene.

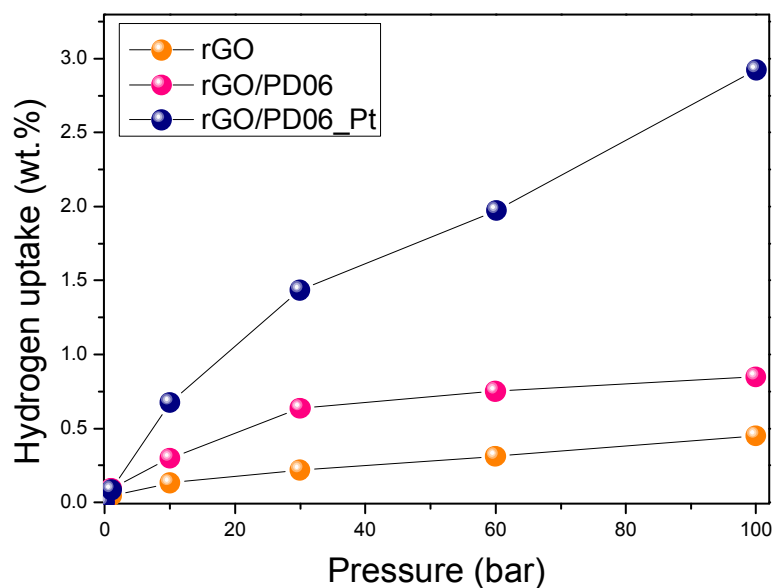


Figure 4. 14. Hydrogen uptakes of rGO, rGO/PD06, and rGO/PD06_Pt at 298 K and 100 bar.

4.4. Conclusion

Pt-decorated graphene foam using bio-inspired PD was suggested for use a promising hydrogen storage material. In order to maximize the hydrogen storage with Pt-decorated graphene, the size, distribution, and decorated amount of Pt nanoparticles along with the BET SSA were controlled by the degree of PD functionalization. As a result, the hydrogen uptake of rGO/PD_Pt showed the highest hydrogen storage capacity per SSA among graphene-based materials with $0.97 \text{ wt.}\% \cdot 10^{-2} \text{ g/m}^2$ at 298 K and 100 bar.

4.5. References

- [1] V. Tozzini, V. Pellegrini, *PCCP* **2013**, *15*, 80.
- [2] J. Sculley, D. Yuan, H.-C. Zhou, *Energy Environ. Sci.* **2011**, *4*, 2721.
- [3] V. V. Struzhkin, B. Militzer, W. L. Mao, H.-k. Mao, R. J. Hemley, *Chem. Rev.* **2007**, *107*, 4133.
- [4] U. Eberle, M. Felderhoff, F. Schüth, *Angew. Chem. Int. Ed.* **2009**, *48*, 6608.
- [5] L. Wang, R. T. Yang, *Ind. Eng. Chem. Res.* **2010**, *49*, 3634.
- [6] J. Dong, X. Wang, H. Xu, Q. Zhao, J. Li, *Int. J. Hydrogen Energy* **2007**, *32*, 4998.
- [7] S. H. Aboutaleb, S. Aminorroaya-Yamini, I. Nevirkovets, K. Konstantinov, H. K. Liu, *Advanced Energy Materials* **2012**, *2*, 1439.
- [8] M. Hirscher, B. Panella, B. Schmitz, *Micropor. Mesopor. Mat.* **2010**, *129*, 335.
- [9] P. M. Budd, A. Butler, J. Selbie, K. Mahmood, N. B. McKeown, B. Ghanem, K. Msayib, D. Book, A. Walton, *PCCP* **2007**, *9*, 1802.
- [10] M. Pumera, *Energy Environ. Sci.* **2011**, *4*, 668.
- [11] G. Srinivas, Y. Zhu, R. Piner, N. Skipper, M. Ellerby, R. Ruoff, *Carbon* **2010**, *48*, 630.
- [12] L.-P. Ma, Z.-S. Wu, J. Li, E.-D. Wu, W.-C. Ren, H.-M. Cheng, *Int. J. Hydrogen Energy* **2009**, *34*, 2329.
- [13]
- [14] G. Srinivas, J. W. Burrell, J. Ford, T. Yildirim, *J. Mater. Chem.* **2011**, *21*, 11323.
- [15] B. H. Kim, W. G. Hong, H. R. Moon, S. M. Lee, J. M. Kim, S. Kang, Y. Jun, H. J. Kim, *Int. J. Hydrogen Energy* **2012**, *37*, 14217.
- [16] Z. Jin, W. Lu, K. J. O'Neill, P. A. Parilla, L. J. Simpson, C. Kittrell, J. M. Tour, *Chem. Mater.* **2011**, *23*, 923.
- [17] J. W. Burrell, S. Gadipelli, J. Ford, J. M. Simmons, W. Zhou, T. Yildirim, *Angew.*

- Chem. Int. Ed.* **2010**, *49*, 8902.
- [18] V. B. Parambath, R. Nagar, S. Ramaprabhu, *Langmuir* **2012**, *28*, 7826.
- [19] B. P. Vinayan, R. Nagar, S. Ramaprabhu, *J. Mater. Chem. A* **2013**, *1*, 11192.
- [20] Y. G. Zhou, X. T. Zu, F. Gao, J. L. Nie, H. Y. Xiao, *J. Appl. Phys.* **2009**, *105*, 014309.
- [21] L. Firlej, B. Kuchta, C. Wexler, P. Pfeifer, *Adsorption* **2009**, *15*, 312.
- [22] S. J. Yang, J. H. Cho, G. H. Oh, K. S. Nahm, C. R. Park, *Carbon* **2009**, *47*, 1585.
- [23] B. P. Vinayan, K. Sethupathi, S. Ramaprabhu, *Journal of Nanoscience and Nanotechnology* **2012**, *12*, 6608.
- [24] V. B. Parambath, R. Nagar, K. Sethupathi, S. Ramaprabhu, *J. Phys. Chem. C* **2011**, *115*, 15679.
- [25] D. P. S. Ramaprabhu, *PCCP* **2014**, *16*, 26725.
- [26] G. Kim, S.-H. Jhi, N. Park, S. G. Louie, M. L. Cohen, *Physical Review B* **2008**, *78*, 085408.
- [27] H. Lee, M. C. Nguyen, J. Ihm, *Solid State Commun.* **2008**, *146*, 431.
- [28] L. Wang, R. T. Yang, *Catalysis Reviews* **2010**, *52*, 411.
- [29] H. Lee, S. M. Dellatore, W. M. Miller, P. B. Messersmith, *Science* **2007**, *318*, 426.
- [30] B. Yang, N. Ayyadurai, H. Yun, Y. S. Choi, B. H. Hwang, J. Huang, Q. Lu, H. Zeng, H. J. Cha, *Angew. Chem. Int. Ed.* **2014**, *53*, 13360.
- [31] M. Bisaglia, S. Mammi, L. Bubacco, *J. Biol. Chem.* **2007**, *282*, 15597.
- [32] S. Hong, Y. S. Na, S. Choi, I. T. Song, W. Y. Kim, H. Lee, *Adv. Funct. Mater.* **2012**, *22*, 4711.
- [33] C. Nethravathi, E. A. Anumol, M. Rajamathi, N. Ravishankar, *Nanoscale* **2011**, *3*, 569.
- [34] N. Mejias, A. Serra-Muns, R. Pleixats, A. Shafir, M. Tristany, *Dalton Transactions*

2009, 7748.

- [35] X. Xiang, W. He, L. Xie, F. Li, *Catalysis Science & Technology* **2013**, 3, 2819.
- [36] B. Zhang, D. Wang, Y. Hou, S. Yang, X. H. Yang, J. H. Zhong, J. Liu, H. F. Wang, P. Hu, H. J. Zhao, H. G. Yang, *Sci. Rep.* **2013**, 3.
- [37] L. Wang, J. A. J. Lachawiec, R. T. Yang, *RSC Advances* **2013**, 3, 23935.

Part III
Conclusions

Chapter 5. Conclusive remarks

Even though CDG is widely studied due to the possibility of mass production and ease of processing, performance of CDG-based applications is still below than that of the expected level due to the lack of appropriate application-targeting CDG design. In order to show an optimized performance in application, the CDG-based material should meet the required properties in a specific application. In this context, this thesis presents a tailor-fitted CDG designs for specific applications using proper modifications.

To design a CDG for TCF application, LN reduction and doping were used. Reduction with LN generated CDG within 10 minutes at room temperature without any damage to the CDG film. In addition, a simultaneous doping effect by residual lithium-containing compounds was obtained by modifying the purification step. The resultant CDG showed TCF performance comparable to that of others even without further treatments. The LN doping effect is more effective and longer lasting than the representative chemical doping with nitric acid.

The CDG for GBL applications utilized functionalization using diol and reduction. The edge-to-edge cross-linking of GO followed by reduction resulted in large CDG, which can improve moisture shielding by increasing the diffusion path of moisture. As a result, the moisture barrier performance was improved by 36.3% when compared to non-cross-linked CDG based composites.

Finally, for hydrogen storage using CDG, reduction, functionalization, doping, and decoration were used. By controlling PD functionalization degree, the surface area as well as Pt size, distribution, and amount were systematically controlled. As a result, Pt-decorated CDG with BET SSA of 303 m²/g and optimal Pt size and amount had the

best hydrogen uptake of 2.93 wt.% at 298K and 100 bar, which is the highest performance among graphene-based hydrogen storage medium, to the best of our knowledge.

All results in this thesis show that production of CDG-based materials with desired properties to maximize performance in specific applications is successfully achieved by tailor-fitted modification of GO.

초 록

그래핀은 투명성, 경량성, 고비표면적, 고강도, 높은 전기 전도도를 지녀, 기존 물질을 능가하는 꿈의 신소재로 각광받아왔다. 특히 화학적 유도 그래핀은 대량 생산이 가능할 뿐 아니라 용액 공정과 비교적 용이한 구조 및 특성 부여 가능성으로 인하여 특히 널리 연구되었다. 그래핀 옥사이드라는 전구체를 이용, 환원, 기능화, 도핑, 장식 등을 비롯한 개질을 통해 원하는 특성을 지닌 화학적 유도 그래핀 기반 물질을 생산해 다양한 응용처에 적용한 연구들이 많이 보고 되었으나, 개질을 통한 화학적 유도 그래핀의 응용처는 기존 범위를 크게 벗어나지 못했을 뿐 아니라 괄목할 만한 특성을 보이지 못했다. 따라서 성능 발현을 최대화하고자, 특정 용도가 요구하는 특성을 충족시킬 수 있는 용도 맞춤형 화학적 유도 그래핀의 설계 및 제조가 필요한 실정이다. 이에, 본 연구에서는 각 응용처의 요구 특성 분석에 기반하여, 관련 물질 파라미터 조절을 위해, 적합 개질을 이용하여 화학적 유도 그래핀 기반 물질을 제조하고 이를 응용하고자 한다.

1부에서는 화학적 유도 그래핀 기반 재료에 대한 전반적 소개와 함께, 특성 조절된 화학적 유도 그래핀 기반 물질 제조를 위한 그래핀 옥사이드의 대표적인 개질 방법들을 소개하였다. 특히

투명전극, 기체 차단막, 수소 저장이라는 세가지 대표적 응용처에 초점을 맞춰, 각 응용처가 요구하는 주요 이슈들을 분석하여 이에 맞춘 할 수 있는 화학적 유도 그래핀 기반 물질 설계 전략과 더불어 이의 필요성을 기술하였다.

2부에서는 1부에서 언급된 전략을 기반으로 화학적 유도 그래핀 기반 물질의 맞춤형 설계 및 응용을 구체적으로 제시한다. 먼저, 투명전극으로의 응용을 위해 부도체인 그래핀 옥사이드를 도체로 만들기 위해 새로운 환원제를 합성하고 이를 이용하여 전기전도도가 높은 투명전극을 제조할 수 있는 방법을 연구하였다. 새로운 환원제로 리튬나프탈레나이드를 새롭게 개발하여 상온에서 단시간에 필름 손상 없이 환원하면서도 동시에 조절된 도핑 효과를 가지는 화학적 유도 그래핀을 제조하여 투명전극으로서의 성능 향상이 가능함을 보고하였다. 다음으로, 기체 차단막에서 기체 투과도를 최소화하기 위해 기체의 확산 속도를 낮출 수 있는 방법을 연구하였다. 이를 위해 edge-to-edge 연결과 환원을 통해 화학적 유도 그래핀의 크기를 증가시킴으로써 기체 확산 경로를 확대하였고 그 결과로 수분 차단 성능이 향상됨을 확인하였다. 수소 저장재료의 활용을 위해, 그래핀 옥사이드를 매개물질을 통해 기능화하고 촉매와 하이브리드함으로써 상온에서의 수소저장능을 향상시킬 수 있음을 확인하였다. 매개물질로 폴리도파민을 발굴하고 환원 및 기능화도

조절을 통해 다공성 그래핀의 비표면적 조절, 그 위에 올리는 촉매인 백금의 크기, 분포, 함량 등의 조절을 통해 상온에서 높은 수소 저장능을 보이는 화학적 유도 그래핀 기반 수소저장재를 보고하였다.

3부에서는 2부에서 제시된 화학적 유도 그래핀의 제조 및 응용에 대해 요약했다. 결론적으로 본 연구는, 용도특성 파라미터를 그래핀 옥사이드의 개질에 반영하는 방법을 모색함으로써, 용도 맞춤형 개질을 통한 화학적 유도 그래핀 기반 물질 설계 방향을 제시하고, 이를 응용처에 적용함을 통해 보다 향상된 성능을 얻을 수 있었다.

주요어: 그래핀, 화학적 유도 그래핀, 그래핀옥사이드, 개질, 응용

학 번: 2011-20670